High Temperature Oxidation Behavior of (Ti,Cr,Al)N Coatings Studied by *in-situ* Synchrotron Radiation X-ray Powder Diffraction

Dissertation with the aim of achieving a doctoral degree at the Faculty of
Mathematics, Informatics and Natural Sciences
Department of Physics
of University Hamburg

submitted by
Daniel Michael Ostach

Hamburg
2017

Gutachter/innen der Dissertation:	Prof. Dr. Andreas Schreyer Prof. Dr. Jens Birch
Zusammensetzung der Prüfungskommission:	Prof. Dr. Robin Santra Prof. Dr. Jens Birch Prof. Dr. Andreas Schreyer Prof. Dr. Andreas Stierle Dr. Norbert Schell
Vorsitzender der Prüfungskommission:	Prof. Dr. Robin Santra
Datum der Disputation:	26.01.2018
Vorsitzender Fach-Promotionsausschusses PHYSIK:	Prof. Dr. Wolfgang Hansen
Leiter des Fachbereichs PHYSIK:	Prof. Dr. Michael Potthoff
Dekan der Fakultät MIN:	Prof. Dr. Heinrich Graener

Abstract

TiCrAlN coatings are superior compared to TiAlN coatings with regard to protect the cutting tool from oxidation. The promotion of α-$(Cr,Al)_2O_3$ has been suggested to be the reason for the improved oxidation resistance with increasing Al content in *ex-situ* oxidation experiments in the literature, whereas the promotion of TiO_2, as known from the literature, has a negative impact on the oxidation resistance. Furthermore, the formed oxide scale is assumed to suppress or at least to hinder a complete decomposition of TiCrAlN at elevated temperatures. At elevated temperatures, TiCrAlN exhibits a spinodal decomposition into coherent enriched TiN TiCr(Al)N and enriched AlN (Ti)CrAlN domains, followed by a transformation from cubic to hexagonal AlN. By *in-situ* time resolved synchrotron radiation x-ray powder diffraction (SR-XRPD) real-time oxidation studies, it is possible to gain detailed information about transformation, oxidation and growth kinetics of oxides. For this purpose, a self-designed thermal annealing setup was constructed to perform real-time oxidation studies on TiCrAlN powder samples with a heating rate of 3000 K min^{-1} up to 1250 °C. The results provide information regarding the oxidation mechanisms of the coating, which shows that the spinodal decomposition of TiCrAlN shows a negative effect on the oxidation resistance, whereas it shows a positive effect on the thermal stability in vacuum. Depending on the Ti-content in TiCrAlN, TiCrAlN can maintain the cubic structure at elevated temperatures, which are typical at the edge of a cutting tool during metal machining. Using a detailed peak fitting procedure it is revealed that the spinodal decomposition also appears under annealed oxidation conditions. Furthermore, by the *in-situ* SR-XRPD technique two assumptions are confirmed: the high oxidation resistance in TiCrAlN is related to a convoluted oxide scale α-$(Cr,Al)_2O_3$ and this oxide scale can nearly suppress a complete decomposition of TiCrAlN. These results provide new findings of the oxidation behavior of TiCrAlN and confirm previous *ex-situ* oxidation investigations of binary, ternary and quaternary material systems.

Zusammenfassung

TiCrAlN Beschichtungen zeigen, im Vergleich zu TiAlN Beschichtungen, überzeugende Eigenschaften im Bezug zur Oxidationsbeständigkeit. Aus den in der Literatur bekannten *ex-situ* Oxidationsexperimenten wird vermutet, dass α-$(Cr,Al)_2O_3$ Beschichtungen mit steigendem Al Gehalt der Grund sind für eine verbesserte Oxidationsbeständigkeit. Dem gegenüber zeigt TiO_2 einen negativen Einfluss auf die Oxidationsbeständigkeit. Die hier entstehenden Oxidschichten unterdrücken oder verhindern zumindest eine komplette Entmischung von TiCrAlN Schichten bei erhöhten Temperaturen. Bei erhöhten Temperaturen zeigt TiCrAlN eine spinodale Entmischung in kohärent angereicherten TiN TiCr(Al)N und angereicherten AlN (Ti)CrAlN Domainen, gefolgt von der Transformation der kubischen zu hexagonalen AlN Phase. Durch *in-situ* zeitaufgelöste Synchrotron Röntgen Diffraktion von Echtzeit Oxidation an Puder (synchrotron radiation x-ray powder diffraction: SR-XRPD) ist es möglich detaillierte Informationen über Transformation, Oxidation und Wachstumskinetik zu erhalten. Zu diesem Zweck wurde ein selbst erstelltes Heizexperiment konstruiert, um Echtzeit-Oxidationsuntersuchungen an TiCrAlN Puder Proben mit eine Heizrate von 3000 K min^{-1} und dabei erreichten Temperaturen von bis zu 1250 °C durchzuführen. Die Resultate liefern Informationen bezüglich der Oxidationsmechanismen, welche zeigen, dass die spinodale Entmischung in TiCrAlN einen negativen Effekt auf die Oxidationsbeständigkeit in Luft zeigt, jedoch einen positiven Effekt auf thermische Stabilität im Vakuum. Abhängig von dem Ti-Gehalt in TiCrAlN bleibt die kubische Struktur bei erhöhten Temperaturen erhalten, welche bei einem Schneidprozess erreicht werden. Durch Verwendung einer Peak-Fit Prozedur konnte gezeigt werden, dass die spinodale Entmischung auch unter aufgeheizter Oxidation entsteht. Zusätzlich konnten mit *In-situ* SR-XRPD zwei Annahmen bestätigt werden: die hohe Oxidationsbeständigkeit von TiCrAlN steht im Bezug zum verschachtelten Oxid α-$(Cr,Al)_2O_3$ und dieses Oxid könnte annähernd eine komplette Entmischung von TiCrAlN unterdrücken. Die Resultate liefern neue Erkenntnisse zu dem Oxidationsverhalten von TiCrAlN und bestätigen vorherige *ex-situ* Untersuchungen an binären, ternären und quaternären Materialsystemen.

Hiermit erkläre ich an Eides statt, dass ich die vorliegende Dissertationsschrift selbst verfasst und keine anderen als die angegebenen Quellen und Hilfsmittel benutzt habe.

Die eingereichte schriftliche Fassung entspricht der auf dem elektronischen Speichermedium.

Die Dissertation wurde in der vorgelegten oder einer ähnlichen Form nicht schon einmal in einem früheren Promotionsverfahren angenommen oder als ungenügend beurteilt.

Hamburg, den 15.06.2017

Unterschrift

Das diesem Bericht zugrundeliegende Vorhaben wurde mit Mitteln des Bundesministeriums für Bildung und Forschung unter dem Förderungskennzeichen 05K12CG1 gefördert. Die Verantwortung für den Inhalt dieser Veröffentlichung liegt beim Autor, Daniel Michael Ostach.

Contents

Chapter 1

1. Introduction and motivation

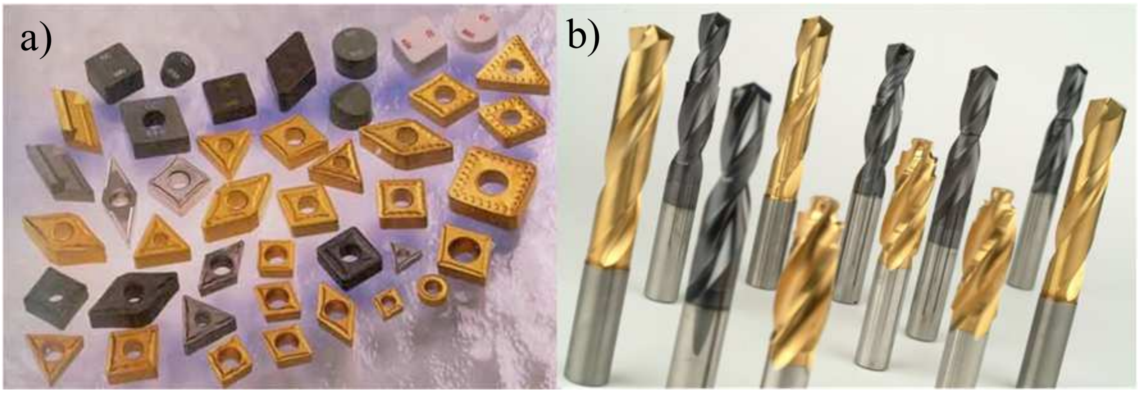

Figure 1: a) Cutting inserts and b) mills and drills are typical cutting tools for application and metal machining in the cutting tool industry. The gold colour is typical for a high TiN content [1] [2] [3].

TiCrAlN films show high hardness, good thermal stability and high oxidation resistance. They are currently replacing more and more the, so far, mostly used coating surface of TiAlN. These films are applied to dry machines and high performance cutting applications. In a real cutting or drilling situation the tools need special requirements depending on their application. High hardness, wear resistance and the ambient impact are only some points which are mentioned. While running a cutting application, the tool heats up very fast, and the point of contact between the cutting tool and the work piece is under high pressure [4]. In the literature there is still a lack of knowledge, whether this point of contact is protected from an oxidation process due to the high pressure or not. Generally, it is important to investigate the reaction between oxygen and an annealed cutting tool. In this thesis, the applied condition on a high performance cutting tool, i.e. high heating rates, is used to study the oxidation behavior of TiCrAlN by *in-situ* time resolved synchrotron radiation x-ray powder diffraction.

One important point in a cutting application is the oxidation process, which the tool is exposed to. The focus of this thesis, therefore, is to simulate an industrial cutting application by a self-designed thermal annealing setup to perform fast heating rates in order to investigate the oxidation process of TiCrAlN under reproducibly controlled conditions.

Protective coatings in the cutting tool industry have been used since 1960s [5], and more than 80 % of the tungsten carbide/cemented carbide inserts (Figure 1) are coated for their specific applications. Coatings on cutting tools show up to 8 times higher lifetime compared to normal bulk material without any protective coating. In the early stage of the industrial use TiN was one of the coatings for the purpose of protecting a cutting tool. But higher requirements on the tools, *e.g.* higher cutting speed, higher hardness, protection of corrosion and oxidation, etc. led to an extension of material classes into ternary systems.

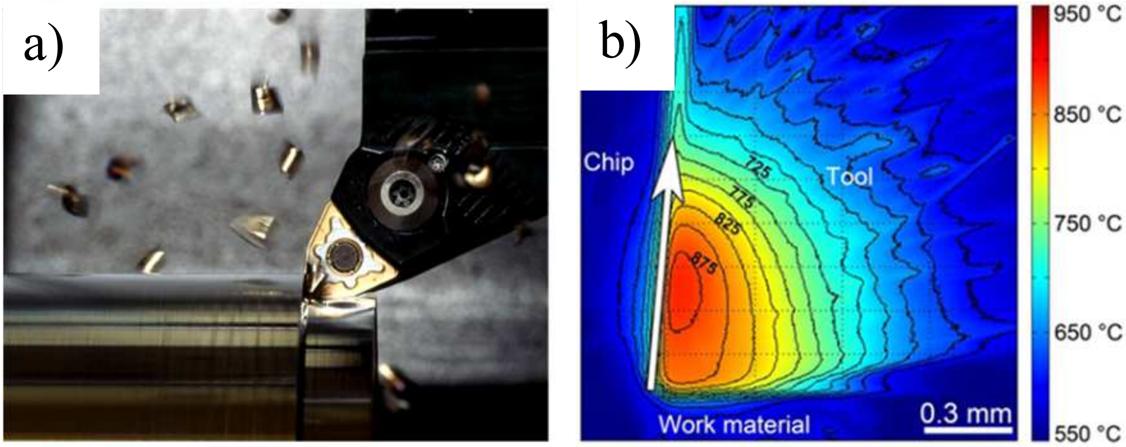

Figure 2: Cutting tools have to fulfil high requirements on the corrosion, wear resistance, hardness, high thermal stability and oxidation. a) Chip formation on a TiAlN cutting insert, b) temperature distribution inside the cutting insert (from [4] [6]).

TiAlN is one of the most used coatings in the cutting tool industry since the 1980s [7] [8], and one can find a lot of specific knowledge in the literature [9] [10] [11] [12] [13] [14] about this ternary coating system. The mechanical properties and oxidation resistance of TiAlN are superior compared to TiN at elevated temperatures [7] [8] [10] [12]. The oxidation process can lead to a deteriorated cutting performance and substrate protection. This is aggravated if the coating is exposed to an oxygen rich atmosphere, *e.g.* normal air instead of protective gases, and if it exposed to elevated temperatures (which is a consequence of the cutting operation).

To minimize the oxidation process, the ternary system CrAlN coating can be used, which shows superior oxidation resistance compared to TiAlN [15]. However, CrAlN coatings have lower hardness compared to TiAlN and, therefore, are not suited for high performance cutting applications. There are many investigations to improve the thermal stability and the cutting performance of adding a third metal, like Nb, Hf, B or Zr to TiAlN to form a quaternary system. Multilayer growth of coatings is also typical concept to improve required properties for a corresponding application. The phase transformations and decomposition processes in the crystal structure of the coating can lead to a decrease in the thermal stability or mechanical stability of the coating which can be suppressed or delayed by the two described concepts above. Therefore, time resolved *in-situ* investigation of these described processes is an outstanding method to study them.

1.1 Aim

The focus of this thesis is to investigate the **real-time oxidation behavior of TiCrAlN coatings** by ***in-situ* time resolved synchrotron radiation x-ray powder diffraction** (SR-XRPD) technique. For this purpose, I designed and build **a thermal annealing setup**, in order to perform real-time oxidation which is closely related to a real-time cutting situation. Especially, fast realistic heating rates of 3000 K min^{-1} were employed to anneal c-TiCrAlN in air.

It has been pointed out, that TiCrAlN with low Ti-content outperforms TiAlN in hardness and oxidation resistance [5]. There is still a lack of knowledge, how the oxidation process arises. By high energy *in-situ* SR-XRPD the **time resolved phase evolution and phase transformation during oxidation** could be followed under real-time industrially relevant conditions for a high performance cutting application.

1.2 Outline

In Chapter 2, a short introduction to the background of the material science relevant for this thesis is presented. Chapter 3 gives a short overview about the unique high energy synchrotron source PETRA III used for the *in-situ* SR-XRPD experiment in the thesis. Chapter 4 describes the high-end industrial scale cathodic arc evaporation technique which was used for the deposition of the TiCrAlN coatings followed with chapter 5, the sample preparation for the experiments. The characterization methods used are described in Chapter 6. In Chapter 7, the self-designed thermal annealing experimental setup is presented. Chapter 8 presents the relevant results of the oxidation experiment. And the last chapters summarize the thesis and give a short conclusion with an outlook into future work.

Chapter 2

2. Material science background

In this chapter, a short overview into the material science around the TiCrAlN ternary system is given.

2.1 TiAlN

TiAlN is widely used as a protective coating for cutting applications, as is has excellent mechanical properties at elevated temperatures [7] [8]. The intention, here, was to add Al to the previously used TiN systems in order to improve the oxidation resistance and the mechanical properties [16] [17]. Both properties can be enhanced by higher Al-content while maintaining the metastable cubic c-AlN structure, i.e. without the possible transformation into the hexagonal h-AlN phase. Furthermore, with higher Al-content the protective aluminium oxide Al_2O_3 layer forms at the surface of the coating [7] [8], thus further enhancing oxidation resistance, as the oxide layer acts as an oxide barrier to avoid the diffusion of oxygen atoms deeper into the coating. As a consequence, the improved mechanical properties can be attributed to the protective Al_2O_3 layer. However, for higher Al-content the metastable c-AlN phase transforms into the stable h-AlN phase with the consequence that the mechanical properties deteriorate. In general, the ternary TiAlN and the later mentioned CrAlN coatings have better oxidation resistance than their binary counterparts, TiN and CrN coatings [18].

2.2 CrAlN

Face centered cubic (fcc) CrN coatings (NaCl or B1 structure) are widely used in industrial applications like metal forming or plastic molding to protect the tools from oxidation and corrosion [19]. In terms of wear resistance and hardness, however, CrN coatings are *not suited* for protection of tools used for metal machining in comparison to other transition metal nitrides [20]. CrN is known to be superior to TiN in corrosion resistance, friction behaviour, and toughness [21] [22] [23] [24].

Like for TiN, by adding Al the mechanical properties of CrN can be improved, thus forming a metastable ternary system, CrAlN. Similar to TiAlN, the incorporation of Al into cubic c-CrN structure, the hardness of CrAlN is enhanced [25]. Likewise, the Al addition leads to the formation of a protective layer of chromium and aluminium (Cr, Al)$_2$O$_3$ oxide layers at the surface of the coating, preventing diffusion of oxygen deeper into the coating [15]. The addition of Al also leads to thermally stable dense c-AlN bonds [26], which improve further the oxidation resistance. The nitrogen concentration can also play a critical factor in determining the CrN film oxidation behaviour [27]. In general, CrAlN coatings have many good properties, such as high toughness, high compressive residual stress, good oxidation resistance and high wear resistance. With an Al-content up to 60 – 70 at. %, it is achievable to deposit metastable cubic c-CrAlN coatings (fcc- structure, B1 cubic structure) [28] [29]. For higher amount of Al, the more stable hexagonal h-AlN phase will form during deposition and thus finally decreases the hardness [29]. Figure 3 sketches the structures involved.

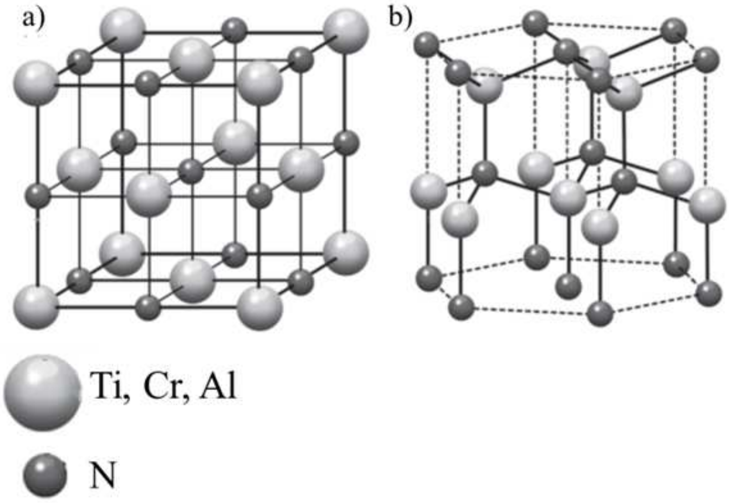

Figure 3: a) B1, NaCl, cubic structure and b) B4, wurtzite, hexagonal structure. The large atoms correspond to Ti,Cr or Al and the smaller one to N. Taken from **[4]**.

In Chapter 4 a short overview about the deposition technique used is given, and in this context the above described transformation from the c-AlN into h-AlN is illustrated in

Figure 10 of Chapter 4.3. The result is a change in crystal structure of c-CrAlN from B1 cubic to B4 hexagonal. Hence, there is a driving force to transform the cubic c-AlN into the h-AlN phase, and with sufficient energy for diffusion processes at elevated temperature, the mechanical properties deteriorate. At 900 °C the cubic phase and the high hardness can be retained up to 2 hours [29]. But during typical metal machining the temperature at the edge of a cutting tool can reach 1000 °C and above [30]. As a consequence, the protective coating used must be able to withstand those extreme conditions. For comparison, the “normal”, i.e. usual, service life time of cutting inserts or drilling cutting tools mentioned and shown above is about only 5 minutes [31].

CrAlN coatings are in these temperature regions usually inadequate for high performance cutting applications. This is explained in literature both, by the smaller curvature of the mixing free energy and the magnitude itself compared to TiAlN [32] [33]. A coherent decomposition doesn't take place, if CrAlN is annealed at high temperature compared to TiAlN [34] [35]. The crystal orientation of c-CrAlN is also related to the Al concentration and shows preferred textures [36]. Similar results are also observed for TiCrAlN in chapter 4.4. CrN shows an abnormal hardness variation – i.e. increase of the coating hardness – in an oxidation atmosphere after annealing at temperature of $\geq$ 800 °C. This might be attributed to the formation of the dense structure Cr_2O_3 [18], but the underlying mechanism of this behaviour is still not clear. The compressive residual stress in CrAlN coatings increases with increasing Al-content [36]. This behavior can be surmised (in Figure 10 of Chapter 4.3) also for TiCrAlN. CrN and CrAlN coatings usually grow in a randomly oriented non-columnar dense structure. CrAlN also shows good oxidation resistance in air. It forms dense oxide mixture layers (Cr_2O_3 + Al_2O_3) at the surface, which is dominated by Cr_2O_3 at high temperature (900°C). Further diffusion of oxygen into the bulk material is prevented, thus also preventing the decomposition of c-CrAlN, which, thus, raises the oxidation resistance temperature [37]. The oxidation kinetics and phase structure evolution are strongly depended on the nitrogen and Al-contents [26]. With a similar Al-content of c-TiAlN coating, c-CrAlN coatings generally feature higher oxidation resistance than c-TiAlN due to the dense mixture structure of Al_2O_3 and Cr_2O_3 on the surface of the coatings [29] [26] .

2.3 TiCrAlN

TiCrAlN is a part of a group of used commercially available quadruple material systems commonly used in industry. It is mainly applied as a protective coating for high performance cutting applications. It contains two important properties, which originate from two different coatings, CrAlN and TiAlN.

Figure 4: The motivation of a functional coating having both, good mechanical properties and high oxidation resistance [20]. TiCrAlN could be one solution.

CrAlN coatings are superior compared to TiAlN with regard to protect the cutting tool from oxidation and corrosion [15], but at elevated temperatures the mechanical properties deteriorate [12] [13]. TiAlN coatings show superior mechanical properties at elevated temperatures (900 °C) [10], but in terms of corrosion and oxidation, it is inadequate at temperature of 1000 °C and above which is typically reached at the edge of cutting tools during metal machining [30]. In short, the motivation of TiCrAlN is having both, oxidation resistance at elevated temperatures and an improved hardness [20], or at least equal high hardness. Figure 4 illustrates this motivation. In comparison with TiAlN, several studies about the TiCrAlN coatings have shown an improved performance [38] [39] [40] [41].

Depending on the Cr- or Ti-content in TiCrAlN coatings, either Ti-rich TiCrAlN or Cr-rich CrTiAlN coatings were studied with regards to the mechanical stability, thermal stability and oxidation resistance [20] [39] [40] [42] [43] [44] [45] [46] [47] [48] [49] [50] [51]. Yamato *et al.* exhibit that the addition of a small amount of Cr in a TiAlN composition increases the onset of the oxidation from 850 °C to 1000°C [51]. In particular, the improved thermal stability and the retained hardness at higher temperature above 1000 °C compared to TiAlN coatings is explained by an intermediate metastable phase in the decomposition route of annealed TiCrAlN coatings. In case of TiAlN, cubic (c)-TiAlN decomposes in two stages under such conditions; first a spinodal decomposition into coherent c-TiN and c-AlN rich domains, followed by a second stage, where c-AlN transforms to hexagonal (h)-AlN. The latter transformation is detrimental for the coating's mechanical properties and, hence, the cutting performance. Alloying of Cr in TiAlN coatings provides an additional decomposition route through the formation of intermediate c-AlCrN and c-TiCrN ternary phases prior to the final stage, where h-AlN and c-TiCrN phases are formed [52]. In effect, Cr in TiAlN delays or suppresses the detrimental effect of h-AlN on the coating's hardness.

Forsén *et al.* studied the effects of Ti-content alloying of CrAlN coatings on thermal stability and oxidation resistance, and reported that the hardness of the CrTiAlN coatings retained after annealing up to 1100 °C due to the spinodal decomposition of the grain interiors into TiCr- and Al-rich c-TiCrAlN [20] [42]. In summary, alloying of Cr in TiAlN increases the thermal stability, while maintaining its hardness [33]. Early oxidation studies of the oxidation resistance of TiCrAlN coatings were focused on coatings with high Al-content due to the protective properties of Al_2O_3. Jianliang Lin *et al.* focused on Al-content less than 30 at. % . They reported a strong correlation between the chemical composition, texture, oxidation resistance and mechanical properties of the CrTiAlN coatings. The cubic phases and the (111) texture of $Cr_{0.61}Ti_{0.10}Al_{0.29}$ coating were reserved after annealing in air up to 1000 °C. By Ti addition in the ternary CrAlN system, the oxidation process is negatively affected caused by the promotion of porous TiO_2 surface layer over a more protective α-Al_2O_3 [52] [53] [54]. The prefix α, θ, etc. describes the crystalline form of the oxides. The α-phase of Al_2O_3 is a corundum/sapphire structure, and the θ-phase of Al_2O_3 is a monoclinic structure.

On the other hand the result of Forsén *et al.* shows that the hardness of CrAlN coatings is improved by the addition of Ti. The striking result is that with TiCrAlN coatings it is possible to generate coatings that outperform TiAlN in terms of oxidation resistance and mechanical properties at high temperatures.

2.4 Phase transformation and phase stability

The stability of a phase in the crystal structure is an important property for the performance of a coating. Essential coating properties, such as hardness, adhesion or oxidation, are depended on different phases. Both, the existing phases and the beneficial phase transformation are important factors to get a qualitative and quantitative relation to the properties described. In crystalline materials, their atoms are arranged in a long range ordered lattice in three dimensions, and for each periodic lattice the unit cells can be obtained for different phases. The most common phases are the body centred cubic (bcc), the face centred cubic (fcc) and the hexagonal close packed (hcp). The latter two examples are shown in Figure 3 for the TiAlN/TiCrAlN structure. Dependent on external parameters like pressure or temperature one material structure can exist in different phases. Some of these phase transitions are described in chapter 2.1 - 2.3.

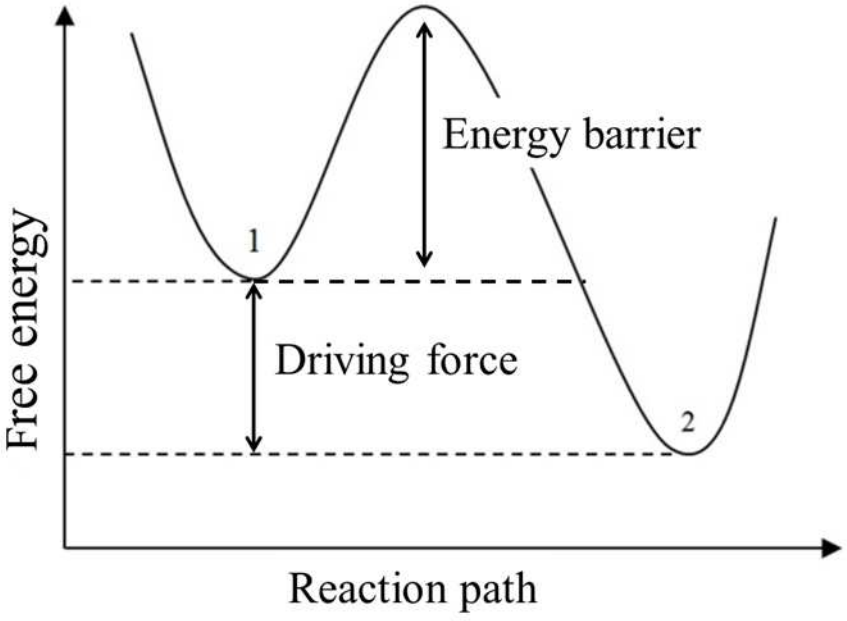

Figure 5: Schematic reaction path of the free energy. Position 1 represents a local minimum, indicating a metastable state. By passing the energy barrier, a more stable state can be reached, the global minimum – or more stable lower energy, further local minimum – at position 2 [4] [55].

In Figure 5 an example is illustrated to explain the thermodynamic state of a stable phase. The minimum of the free energy at position 1 represent a local minimum, *e.g.* the metastable phase. The minimum at position 2 shall represent (for simplification) the global minimum, i.e. stable phase and, therefore, the most favourable state at the minimum energy. There must be a driving force for the described system at position 1 to transform to position 2. In order to get from a metastable phase to a stable phase, the passing of an energy barrier is required.

2.5 Oxidation

In a general view, the oxidation process is a chemical reaction, where oxidized sort donates electrons to a second reactant, which by accepting them reduces itself [56]. All metal oxides are of ionic nature. The standard free energies of oxygen formation of all non-noble metals (show no resistance to oxidation and corrosion whereas noble metals show resistance to oxidation and corrosion) are negative [57]. Therefore, oxidation of non-noble metals always occurs in an oxygen-containing atmosphere. However, the question on which time scale this occurs is, thus, not yet theoretically determined [56]. At low temperatures, the oxidation reactions are slowed down to long time scales, and the activation energies are generally large. For elevated temperatures, the oxidation process deteriorates the metallic properties in much shorter time, and the activation energies are low [56]. Oxides remain at surfaces of metals, and form a continuous oxide layer, if the oxide is not volatile. The ongoing oxidation slows down, if the oxide layer is resistant to transport of oxidized species to the reaction zone, i.e. that if it forms an oxide barrier that separates the reactants and, thereby, delays the transport of the reactants through it. The aim for engineering materials must be to design materials, which withstand high temperature exposures in a specific and aggressive environment. Consequently, materials rely on the formation of continuous and slowly growing scales [56]. Specifically, alloys that form Al_2O_3, Cr_2O_3 or SiO_2 diffusion barriers as a coating protection are often used constituents to reach acceptable lifetime of metallic or ceramic component for high temperatures and high performance applications in an oxidizing atmosphere [58] [59] [60]. The aforementioned oxides have this property as they show the smallest relative growth rates in comparison to FeO or CoO [56] [59].

Chapter 3

3. X-ray synchrotron source

This chapter gives a short overview of the x-ray source used for the *in-situ* annealing measurements. The high brilliance of synchrotron radiation sources enables x-ray characterisation of the used TiCrAlN powders with a quality and time resolution much superior to that with a lab-based-x-ray source.

3.1 Synchrotron radiation

This kind of radiation takes its name from the specific type of particle accelerator where it was first recognized in 1945. The radiation comes from charged particles which move at relativistic speed in a magnetic field, which forces them to change its flight direction, i.e. accelerates them, thereby emitting strongly tangentially directed “white” radiation. Most synchrotron radiation is nowadays produced in storage rings like in the case of PETRA III, DESY, Hamburg. The synchrotron radiation in a storage ring can be produced in bending magnets, which keep the electrons in a closed orbit, or in insertion devices like wigglers or undulators, situated in straight sections of the storage ring. In undulators, the small-amplitude oscillations from the passage of a single electron produce a coherent addition of the radiation from each oscillation, thus leading to an enormous flux in comparison to lab-sources or bending magnets. Synchrotron radiation is not an artificially generated radiation, in fact, it occurs also naturally and has been observed from plasmas around stellar nebula [61]. The features of synchrotron radiation diffraction are especially attractive for quantitative diffraction. The advantages are *e.g.* high resolution, high peak-to-noise ratio, and the possibility to enable thin film studies with low background level due to elimination of samples fluorescence by suitable wavelength selection with narrow spectral band, and low level of instrumental aberrations [62].

3.2 HEMS beamline

The High Energy Materials Science beam line HEMS at PETRA III (Max von Laue Hall) is part of a worldwide unique infrastructure of research with high brilliance synchrotron x- ray photons in an energy range from soft to hard x-rays. This beam line is focused on a tunable energy range of 50-200 keV [63] [64]. At HEMS, one of the material science activities is applied research. The combination of high flux, the availability of fast detector systems together with the small scattering angles (high photon energy) allows time resolved investigations of complex and dynamic processes.

available techniques	XRD, SAXS, 3D-XRD, Tomography
photon source	Undulator
source brilliance	10^{18} ph / s / 0.1% bw / mA
Polarization	linear horizontal
energy range	32 keV – 200 keV
beamline energy resolution	5 – 250 eV at 80 keV
max flux on sample	7 x 10^{11} ph / s at 100 keV
spot size on sample	1 mm x 1 mm down to 2 µm (v) x 30 µm (h) with Al-CRLs 0.9 (v) x 6 (h) mm for 3D-XRD for low-beta mode
angle of incidence	0 to 90^{o}, 3.5 A^{-1}(solid, liquid in EH2) 0 to 15^{o} (EH3), 0 for 3D-XRD and Tomography
sample type	solid or liquid

Table 1: General specifications of the HEMS beamline **[63] [64]**.

This optimized instrumental situation was the important prerequisite for the *in-situ* investigations of annealed TiCrAlN samples in this thesis with high and low heating rates. Table 1**:** presents the general specifications.

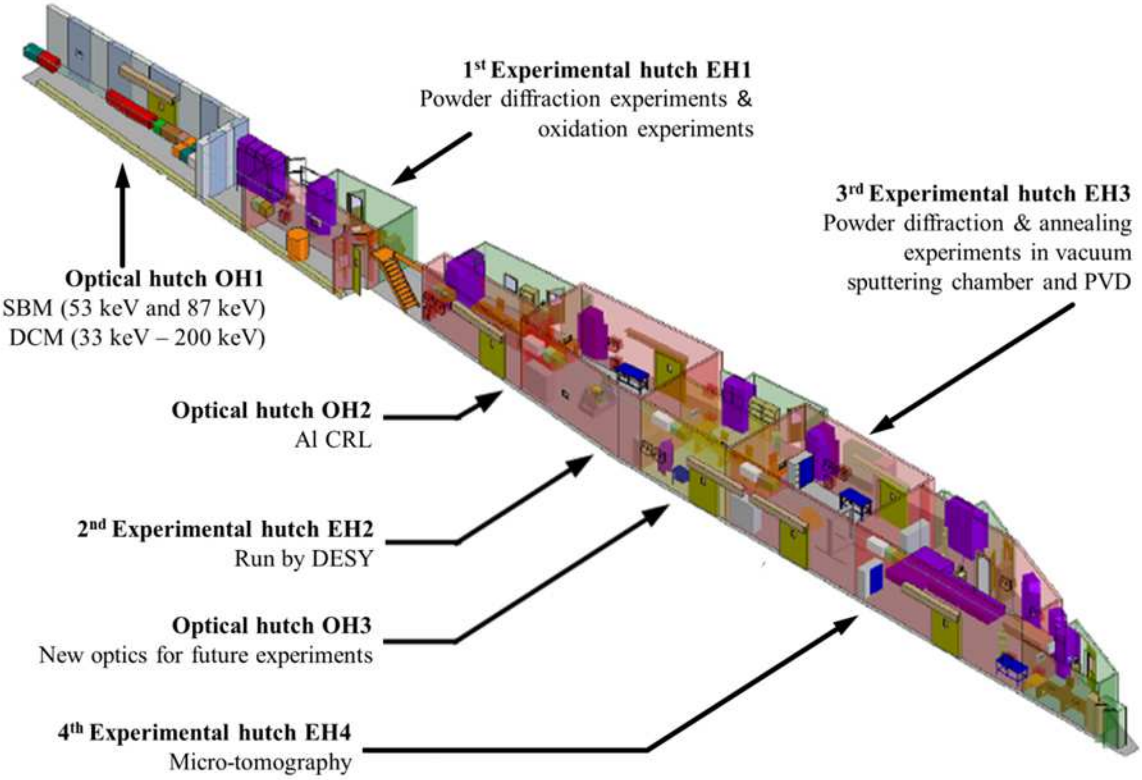

Figure 6: Overview of the HEMS beamline P07. The experiments were conducted at EH1, and EH3 as shortly described under the left listed headlines.

The optics hutch OH1 (Figure 6) harbours two main optical systems: the single bounce monochromator (SBM) for the side station/test facility experimental hutch EH1, and the double crystal monochromator (DCM) for the other parts/experimental hutches of the beamline. The SBM consists of two flat water-cooled Laue crystals Si(111) and Si(220) with an asymmetric angle of 35.56°. The energy can be changed between 53.7 keV and 87.1 keV with a fixed horizontal scattering angle of 4.25°. The maximum beam size in EH1 is approximately $0.9 \times 0.9 \text{ mm}^2$ with an integrated flux of approx. 7×10^9 photons/sec. 0.01 % bw [63]. A challenge for experiments in EH1 is the higher harmonics generated by the SBM (here the 2nd harmonic for 87.1 keV) which poses an issue specially for the measurements and data analysis. But with a direct identification of the 2nd harmonic generated Debye-Scherrer rings the data analysis was succesfull.

Chapter 4

4. Deposition of TiCrAlN thin films

For the cutting tool industry the cathodic arc evaporation is a widely used method to fabricate coatings. The main advantages of this method are the high grade of reproducibility and fast growth.

This cathodic arc evaporation method belongs to the category of physical vapour deposition (PVD) technique [65]. In PVD, the material is vaporized from a solid or liquid source in the form of atoms or molecules. This forms a vapor, which moves through a vacuum to a substrate and condenses on the substrate [66]. This chapter gives a short overview of the deposition process used. In the thesis, an industrial scale cathodic arc evaporation system was used. In this context, industrial scale represents high growth rate of 1 – 10 nm per second or more.

4.1 Physical vapor deposition – PVD

In general, the PVD process starts with a transition from a solid or liquid phase into a vapor phase. The vaporized material moves towards the substrate, and the material condenses on the surface of a substrate, first nucleating in islands or monolayers, followed by further growth of more or less tilted and/or texturized columns. Alternatively, the film grows in epitaxial layers under certain parameter constellations.

4.2 Cathodic arc evaporation

In cathodic arc evaporation, a high current and low voltage discharge between two electrodes leads to characteristic small, melted locations (spots) on the cathode surface. An electric arc is responsible for the evaporation and locally melted areas on the target [67]. From the cathodes, the solid material transforms into a plasma consisting of electrons and positively charged ions. The plasma generated transports the electrical current between the electrodes and, therefore, the arc process is self-sustaining [68]. To avoid impurities from air in the coating while depositing the substrate, the whole evaporation process takes place in a high vacuum environment.

The cathode is made up of the material which is to be used for the vapor deposition. The composition of the film is controlled by using compound cathodes which contain several elements in different quantity – or by simultaneously/sequentially operated several mono-elemental targets. In addition, one can place the cathodes at different positions in the deposition chamber, *e.g.* at different height positions (Figure 7a), thus, thin films with several compositions can be achieved. This configuration results in a gradient change in compositions of the coatings along the height of the drum, as illustrated in Figure 7b. The substrates are mounted on a drum that rotates during deposition. In this thesis, an industrial scale arc evaporation system Sulzer Metaplas MZR323 from SECO® Tools AB[1] was used, which allows this configuration just described. Here, Ti-Al and Cr-Al compound cathodes with different quantity of these elements were used. As the final coatings were to be nitrides, the compound cathodes used, however, were metallic, a flow of N_2 gas into the deposition chamber had to supply the nitrogen and react with the ejected atoms on the way to the substrate. The pressure during the deposition process was 4.5 Pa. Before the onset of the deposition process, the substrates were Ar ion etched and heated for 30 min. The evaporation process is initiated by a high current of 150 A at each cathode. The high current density results in a high local surface temperature on the cathode surface, which is high enough to melt and evaporate the cathode material [69]. The substrate temperature was approximately 550 °C. The temperature is determined by the energy transfer of the ions and the heater in the chamber wall.

The high grade of electron collisions in the ionization zone [70] reaches a high degree of ionization [71] [72]. The high ionization is desirable to affect the kinetic energy and, hence, the surface mobility of the impinging atoms controlled with the substrate bias. These ions are attracted by a negatively biased substrate of -35 V.

---

[1] http://www.secotools.com/de, “Seco Tools has an established reputation as a leading manufacturer and supplier of carbide cutting tools and associated equipment”.

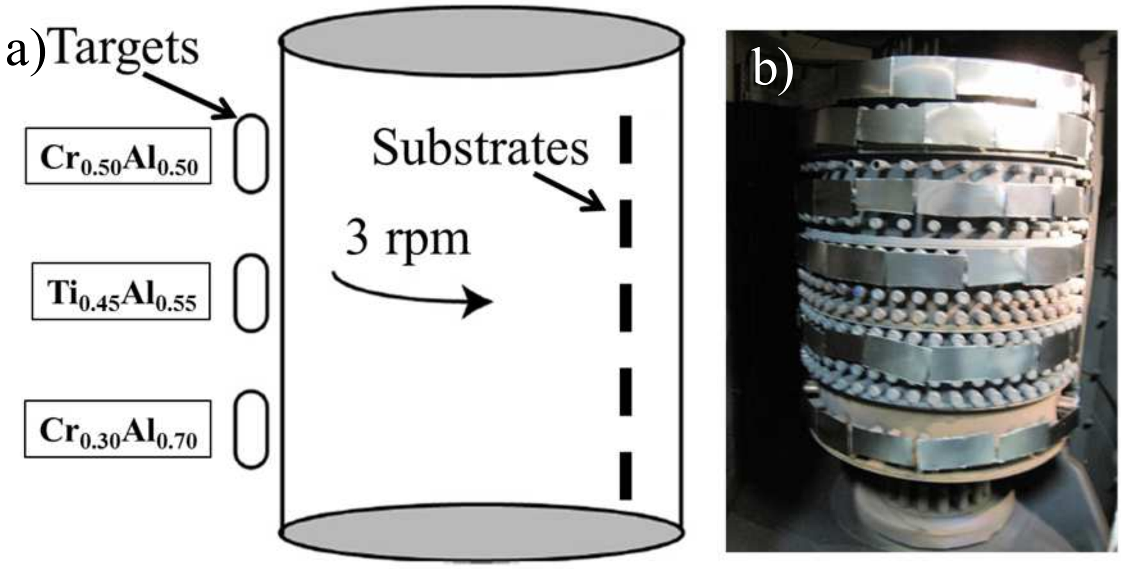

Figure 7: a) Schematic illustration of the deposition system used to synthesize the films. The targets marked with a black arrow represent the height position, top, middle, and bottom. The compound cathodes in this sequence mentioned are used as follows: Configuration 1: $Ti_{33}Al_{67}$, $Cr_{50}Al_{50}$,$Ti_{75}Al_{25}$ & Configuration 2 (here shown): $Cr_{50}Al_{50}$, $Ti_{45}Al_{55}$, $Cr_{30}Al_{70}$. b) Photo of the substrate magnet drum inside the Sulzer Metaplas MZR323 from SECO® Tools AB.

In this thesis two cathode configurations were used for the deposition of the TiCrAlN coatings. In Figure 7 the configuration settings are illustrated with the compound cathodes used. The drum consists of many small cylindrical magnets, which are perpendicular to the drum surface. On the magnets, iron foils (shown) and WC substrates (back side of the drum, not shown) were placed.

4.3 Growth of the coating

The generation of small droplets (macro-particles) on the surface of the substrate are characteristic for cathodic arc evaporation (Figure 8). These particles are incorporated in the coating during film growth. The high current density on the surface of the cathodes, the cathodes material and the located molten spots of the cathodes lead to these droplets. The droplets consist of pure metal from the cathodes and they are positively charged. The particle number and microstructure at the surface can be controlled with the substrate bias [73]. Compared to the coating, the mechanical properties of these metallic droplets are generally lower [4]. The surface shows a high amount of impurities which is typical for coatings fabricated under industrial conditions.

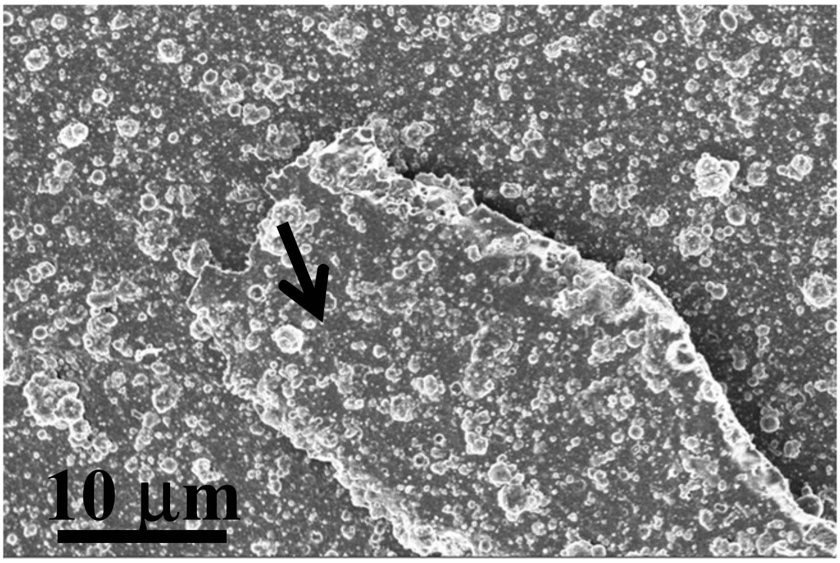

Figure 8: Surface of TiCrAlN on WC manufactured with PVD with the industrial cathodic arc evaporation. The black arrow shows one droplet. These small melted droplets are characteristic for cathodic arc evaporation. SEM with magnification 5000, 5 kV, WD 5.2 mm, the scale bar is 10 µm .

Usually, cathodic arc depositions are implemented between 300 °C - 500 °C. With these low temperatures, it is possible to deposit coatings with unstable phases. The atoms do not get enough energy to diffuse and rearrange to their equilibrium positions during the deposition [52]. However, it is high enough for crystalline growth.

The film growth is controlled by the energy of the atoms at the surface of the film. By increasing the deposition temperature, the diffusion leads to an increasing grain size and lower porosity [74] [75]. Figure 9 shows a cross section of a scanning electron microscope (SEM, described in Chapter 6.4) of TiCrAlN coated WC substrate.

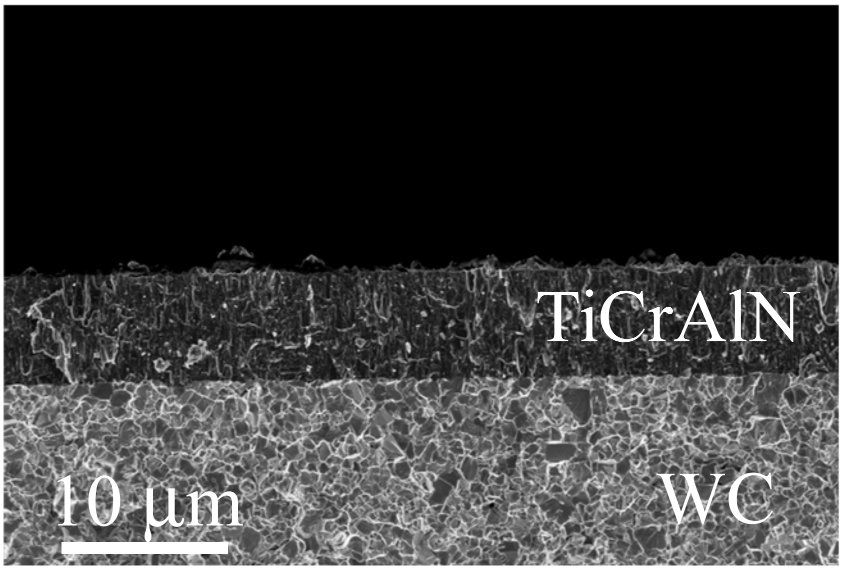

Figure 9: SEM cross section of $Ti_{0.16}Cr_{0.36}Al_{0.48}N$ on WC-Co substrate. The thickness of the coating is up to 8 µm after 30 min deposition time. Magnification 5000, 5 kV and WD (Working Distance) 3.2 mm.

In Figure 10, a θ-2θ diffractogram (Cu-laboratory system) of as-deposited coatings fabricated with configuration 1 A is shown as described in Figure 7. The range is between 30° to 70°. The arrow direction on the right side represents the increasing of the elements Ti, Cr and Al of the compositions. The $Ti_xCr_yAl_zN$ coatings were deposited across an aluminium concentration range of $0.23 \leq z \leq 0.64$, across a chromium concentration range of $0.04 \leq y \leq 0.44$ and a titanium concentration range of $0.09 \leq x \leq 0.73$. The range is determined by the cathode composition as described above.

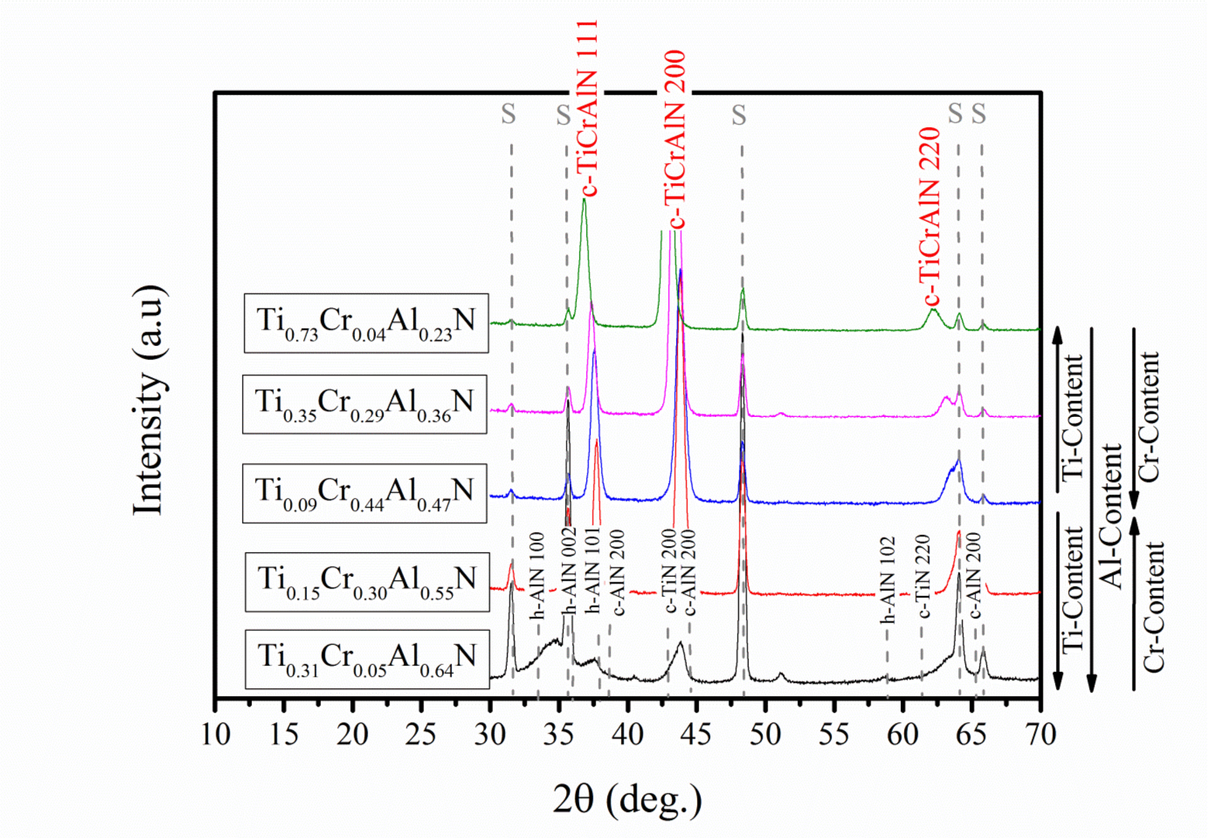

Figure 10: X-ray θ-2θ diffractograms of as-deposited coatings. The compositions are the results from the configuration 1A as described in Figure 7. The c-TiCrAlN (111), (200) and (220) are red labeled. The WC substrate is grey labeled with S. The as-deposited composition $Ti_{0.31}Cr_{0.05}Al_{0.64}N$ illustrates the onset of the h-AlN phase transformation as described in Chapter 2.

All coatings have a cubic structure. The diffractogram contains peaks from the WC substrate indicated by S and the cubic TiCrAlN peaks (111), (200) and (220). The as-deposited composition with $z = 0.64$ (highest Al-content) shows a transformation into the equilibrium hexagonal structure h-AlN. The decrease or suppression of the c-$Ti_{0.31}Cr_{0.05}Al_{0.64}N$ peaks are not the result of an oxidation process but rather a phase transformation and nano-crystalline coating growth. The shown transformed mixture of hexagonal structure and cubic structure of AlN in the as-deposited coating was also reported in [76] with high Al-content (Al > 60 at. %). In this thesis, the *in-situ* measurements were conducted on powder materials to enable quantitative information and *not* on coated WC substrates. The reasons are described in more detail in Chapter 5.

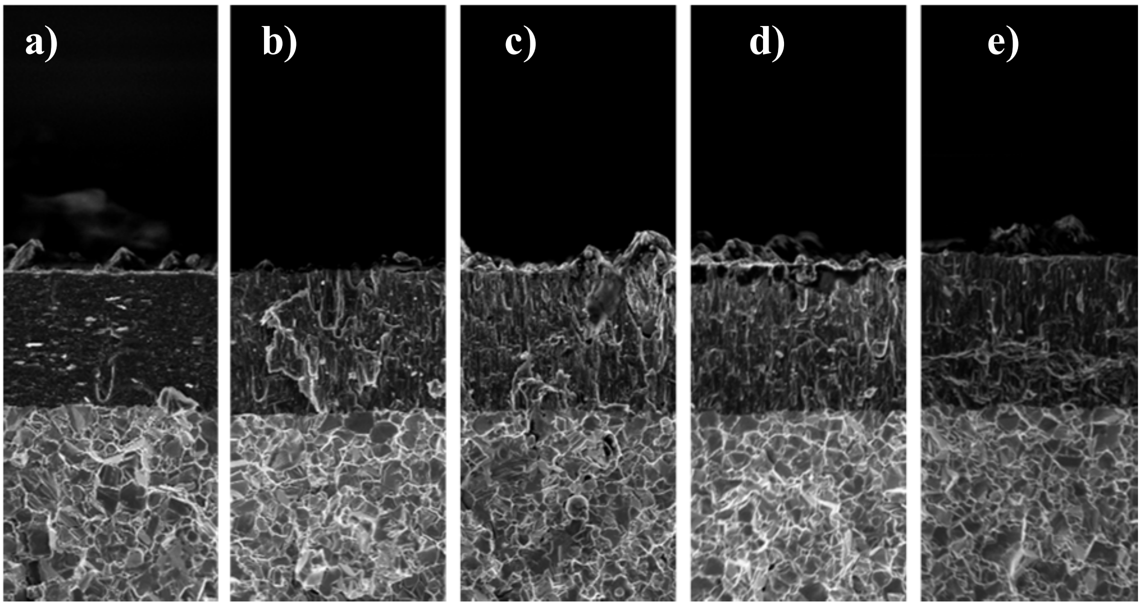

Figure 11: Fraction cross section of TiCrAlN coated WC. a) $Ti_{0.31}Cr_{0.05}Al_{0.64}N$, b) $Ti_{0.15}Cr_{0.30}Al_{0.55}N$, c) $Ti_{0.09}Cr_{0.44}Al_{0.47}N$, d) $Ti_{0.35}Cr_{0.29}Al_{0.36}N$, e) $Ti_{0.73}Cr_{0.04}Al_{0.23}N$. SEM magnification 5000, 5 kV, WD 3.2 mm.

The fractured cross section studied in the SEM (Figure 11) reveals that the coatings show a thickness between 7–8 µm. The coating with high Al-content has a fine-grained, smooth structure with flat surface, whereas with a decrease of the Al concentration the smooth structure transform in a more random, defect rich structure. The structure shows more big grains and a dense columnar structure with a high density of defects. The surface is rougher. With lower Al concentration and higher Ti-content, the structure becomes mixture of porous structure and a columnar structure with a lower density of defects.

4.4 Texture of TiCrAlN coatings

From the θ-2θ data of the as-deposited state of the coating, the preferred orientation can be described by the texture coefficient T_C. It is defined in Eq. (1):

$$\boldsymbol{TC_{i\{hkl\}}} = \frac{\boldsymbol{I_{\{hkl\}}}}{\boldsymbol{I^0_{\{hkl\}}}}\left[\frac{\mathbf{1}}{\boldsymbol{k}}\sum_{\boldsymbol{i=1}}^{\boldsymbol{k}}\frac{\boldsymbol{I_{i\{hkl\}}}}{\boldsymbol{I^0_{i\{hkl\}}}}\right]^{-1} \tag{1}$$

$I^0_{i\{hkl\}}$ is the intensity of every peak extracted from ICDD database (International Centre of Diffraction Data), $I_{i\{hkl\}}$ is the measured spectrum of all peak intensities (only peaks of the coating) from Figure 10, $I_{\{hkl\}}$ is the measured peak intensity of one peak and $I^0_{\{hkl\}}$ is the intensity from the ICDD database.

The TC_i coefficients with their equivalent compositions are presented in Table 2 and Table 3. As seen from the as-deposited data in Figure 10, three coating reflections (111). (220) and (200) are used for the TC_i calculation. Therefore, TC_i can vary between 3 (complete preferred orientation) and 0 (random orientation).

Composition	TC_i (111)	TC_i (200)	TC_i (220)
$Ti_{0.31}Cr_{0.05}Al_{0.64}N$	0.94317	1.04105	1.01578
$Ti_{0.16}Cr_{0.36}Al_{0.48}N$	1.05499	1.67904	0.26597
$Ti_{0.09}Cr_{0.44}Al_{0.47}N$	1.22291	1.43609	0.341
$Ti_{0.35}Cr_{0.29}Al_{0.36}N$	0.61741	2.23531	0.14728
$Ti_{0.73}Cr_{0.04}Al_{0.23}N$	0.76633	1.99412	0.23955

Table 2: Texture coefficients of (111), (200) and (220) calculated with Eq. (1) of the diffraction pattern from Figure 10 of the deposition with deposition configuration 1 (see Figure 7).

Composition	TC_i (111)	TC_i (200)	TC_i (220)
$Ti_{0.02}Cr_{0.53}Al_{0.45}N$	1.15624	1.4893	0.35446
$Ti_{0.05}Cr_{0.49}Al_{0.46}N$	1.19756	1.46649	0.33595
$Ti_{0.16}Cr_{0.36}Al_{0.48}N$	0.94966	1.84975	0.20059
$Ti_{0.32}Cr_{0.16}Al_{0.52}N$	0.56519	2.29516	0.13966
$Ti_{0.20}Cr_{0.18}Al_{0.62}N$	0.93354	1.61326	0.4532
$Ti_{0.03}Cr_{0.38}Al_{0.59}N$	0.72345	1.87412	0.40243

Table 3: Texture coefficients of (111), (200) and (220) calculated with Eq. (1) of the diffraction pattern from Figure 10 of the deposition with deposition configuration 2 (see Figure 7).

Table 2 and Table 3 show only an overview of the fabricated samples and their calculated texture coefficients. Most of the compositions in Table 2 and Table 3 show a (200) preferred orientation after deposition, whereas the composition $Ti_{0.35}Cr_{0.29}Al_{0.36}N$ (Table 2) and $Ti_{0.32}Cr_{0.16}Al_{0.52}N$ (Table 3) show the strongest preferred orientation $TC_i > 2$, and the composition $Ti_{0.31}Cr_{0.05}Al_{0.64}N$ (Table 2) shows the weakest preferred orientation $TC_i \approx 1$. There is no change of the preferred orientation depending on the compositions, nevertheless only a trend can be estimated.

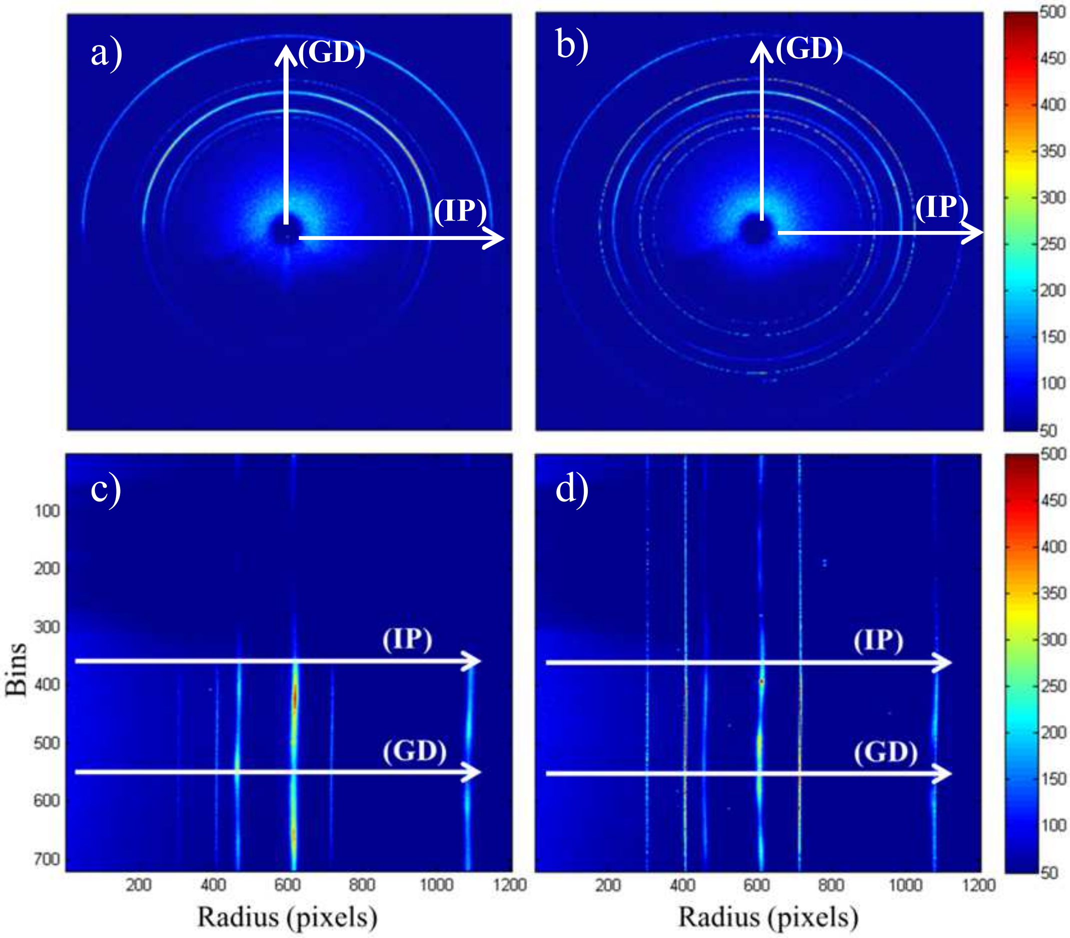

Figure 12: Synchrotron texture measurements of the compositions a) $Ti_{0.03}Cr_{0.38}Al_{0.59}N$ and b) $Ti_{0.16}Cr_{0.36}Al_{0.48}N$ from Table 2 and Table 3 with textures and the transformed images in c) (corresponds to a)) and d) (corresponds to b)). The arrows show the in plane direction (IP) of the coating and the growth direction (GD). Synchrotron energy E = 53.7 keV, measured in side station EH1 (see Chapter 3).

In Figure 12a) and b), the images represent the optimized aligned pattern. There are dark regions without or with less data information due to the absorption of the synchrotron radiation upon transmission through the prepared WC sample. Figure 12c) and d) are the transformed images of Figure 12a) and b). The transformed image corresponds to a radial plot of the diffraction pattern in Figure 12a) and b). This is a ”binning” in radial direction of the diffraction pattern, and additionally, an adding of the radial plot around the azimuth angle, which results in the transformed images in 12c) and d). According to the program analysis used, the bin size is 2. Therefore, the Bins on the left scale is: 360° full rotation (360° azimuth angle) multiply with 2, results in 720 Bins. The x-axis is the radial distance in pixels. The two samples show a strong preferred (200) orientation. The a) $Ti_{0.03}Cr_{0.38}Al_{0.59}N$ sample shows a strong texture between the IP and GD in 45° related to the IP. The $Ti_{0.16}Cr_{0.36}Al_{0.48}N$ sample shows a strong texture in the IP and in the GD. In the next Chapter 5, there are some reasons given why, for the next step, other samples (more precise: powder samples) are used for the oxidation measurements.

Chapter 5

5. Sample preparation (Powder samples)

For the oxidation experiments only powder samples could finally be used: when heating the coatings on their substrate, the different thermal expansions between coating and substrate led to an ablation of the coating, whereby the coating moved out of the beam, hence, it was necessary to remove the coating from its substrate (Figure 13). Furthermore, removing the coating from the substrate was advantageous in order to prevent any interaction with the substrate for annealing temperatures of 1000 °C and above, and in order to avoid peak overlaps from WC-Co-substrate and coating in the XRD diffractograms (alleviating data analysis).

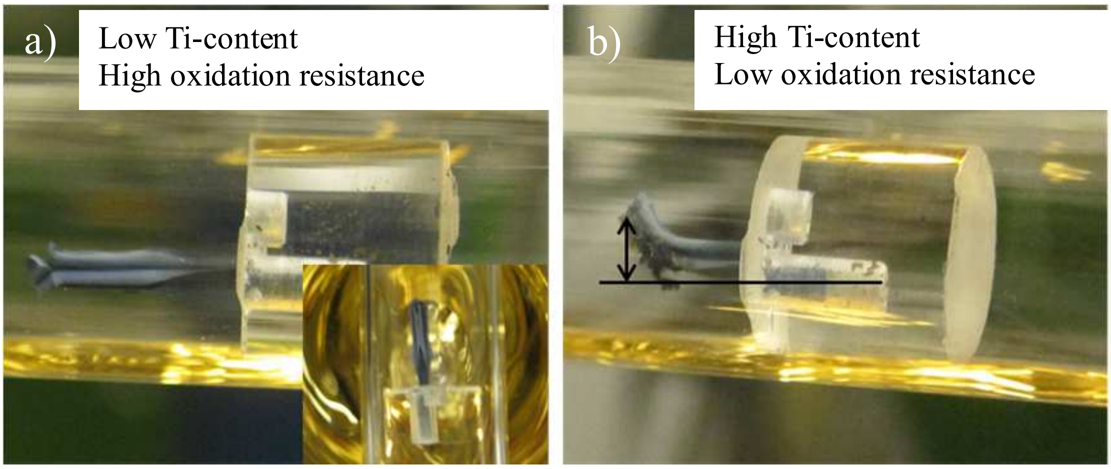

Figure 13: TiCrAlN coatings on WC substrates. The pictures show the TiCrAlN samples after annealing within 6 minutes for a) low Ti-content and b) high Ti-content. Both samples show a deformation and partial ablation after annealing. The two photos show the reason why the coating had to be removed from the substrate for the *in-situ* synchrotron radiation experiments. TiCrAlN with low Ti-content seems to protect the WC substrate much better compared to that with high Ti-content.

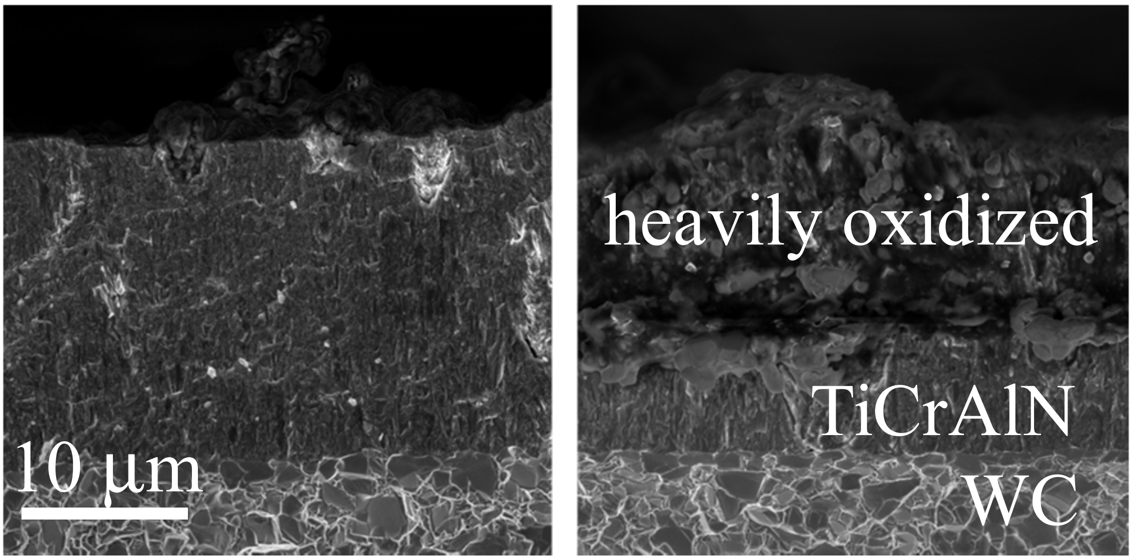

Figure 14: SEM cross section of $Ti_{0.03}Cr_{0.38}Al_{0.59}N$ on WC-Co substrate. The thickness of the coating is up to 8 µm after 30 min deposition time. Magnification 10000, 5 kV, WD 3.2 mm.

In Figure 14 a SEM of a cross section of $Ti_{0.03}Cr_{0.38}Al_{0.59}N$ on WC-Co substrate is illustrated, the as-deposited state and the state after annealing up 3 min at 1250 °C. Here, the fine-grained structure is destroyed by oxidation at the indicated temperature. The result is a heavily oxidized coating, with coarse-grained structure. Nevertheless, the coating withstands and protects the WC substrate within a short time, which corresponds approximately to the normal service life time of cutting inserts (Chapter 2).

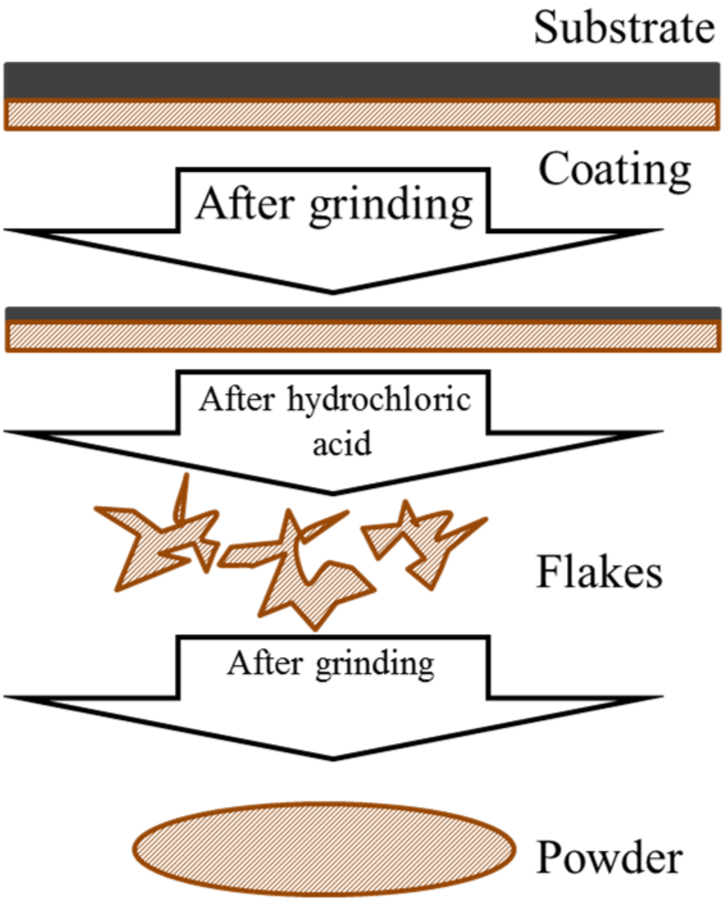

Figure 15: Schematic illustration of the fabrication of the TiCrAlN powder used in this thesis.

Also thin iron sheets were used as substrate during deposition. The iron sheets were placed in the same height of the WC-Co inserts to ensure that the coating compositions were identical (see Chapter 4). After deposition, the backsides of the iron sheets were mechanically ground as thin as possible, such that a following hydrochloric etching removed the residual iron and dissolved the coating into flakes (Figure 15). These flakes were cleaned in acetone and distilled water, and finally ground into a fine powder. With this procedure the structure of the coating is retained [10].

After grinding the iron foils coated with TiCrAlN, the powder samples were measured with SEM again. With energy dispersive x-ray spectroscopy technique the element content of the compositions was measured. After grinding, the contents have been changed only slightly for all compositions. The nitrogen contents were about 50% for every composition. With these results, only compositions were chosen which showed a constant Al and Cr (Figure 16). The powder compositions after grinding are summarized in Table 4.

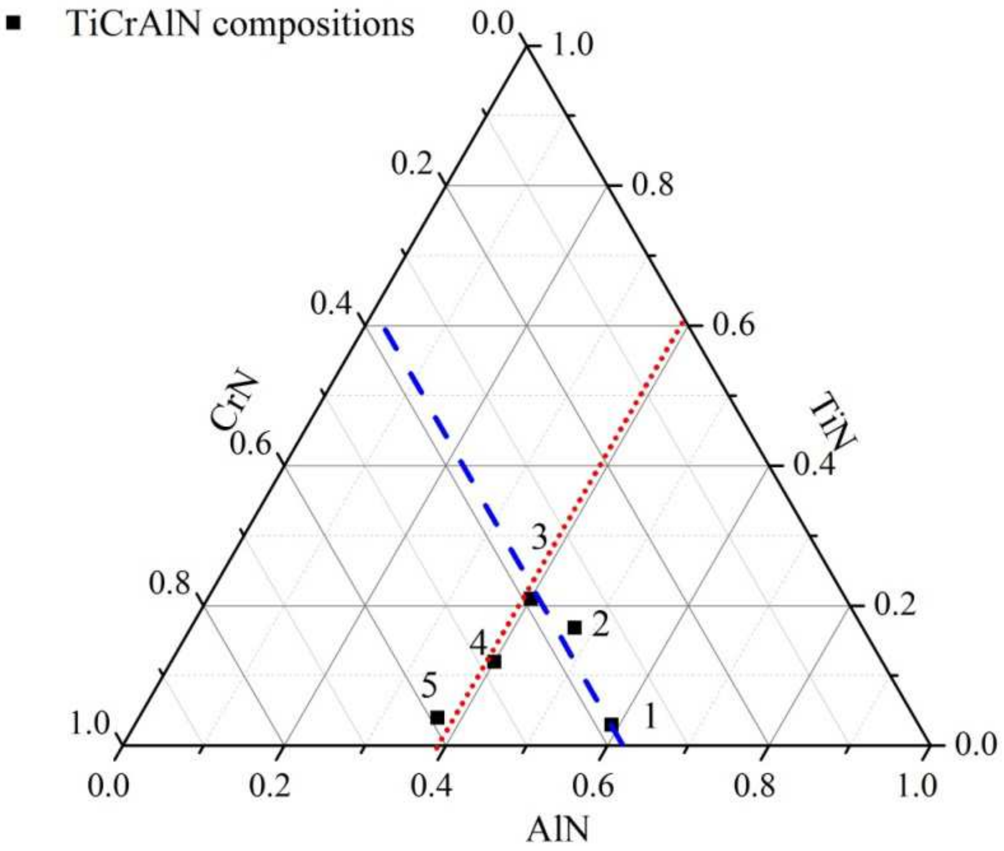

Figure 16: Ternary phase diagram of powder samples fabricated at SECO Tools AB. The diagram shows compositions with constant CrN - - - and AlN ··· content. The numbers indicate the respective compositions in Table 4.

No.	Composition	Internal label
1	$Ti_{0.03}Cr_{\mathbf{0.38}}Al_{0.59}N$	R368-A02-Pos6
2	$Ti_{0.16}Cr_{\mathbf{0.36}}Al_{0.48}N$	R368-A01-Pos2
3	$Ti_{0.21}Cr_{\mathbf{0.39}}Al_{\mathbf{0.40}}N$	R368-A02-Pos3
4	$Ti_{0.12}Cr_{0.48}Al_{\mathbf{0.40}}N$	R368-A01-Pos3
5	$Ti_{0.04}Cr_{0.59}Al_{\mathbf{0.37}}N$	R368-A02-Pos2

Table 4: Overview of fabricated TiCrAlN compositions shown in Figure 16. The coloured sample labels mark the samples with constant CrN (**blue**) content and AlN (**red**) content.

Chapter 6

6. Characterization methods

This chapter introduces the techniques which had been applied for characterizing the TiCrAlN powder samples within this thesis. The techniques are x-ray diffraction (XRD), energy dispersive x-ray spectroscopy (EDX or EDS), scanning electron microscopy (SEM), transmission electron microscopy (TEM), wide-angle x-ray scattering (WAXS) and *in-situ* synchrotron radiation x-ray powder diffraction (SR-XRPD). The SR-XRPD technique was performed at the High Energy Material Science (HEMS) beamline P07.

6.1 X-ray beam

An x-ray is classically a transverse electromagnetic wave, where the electric field **E** and magnetic field **H** are perpendicular to each other and to the direction of propagation **k**. The wavelength is in the region of Ångströms (10^{-10} m). In this thesis, a monochromatic synchrotron x-ray radiation was used. The interaction of x-rays takes place with the electron shells of atoms or the electronic bandstructure of crystals. From the quantum mechanical perspective, this monochromatic electromagnetic wave can be quantized into photons of specific energy:

$$\boldsymbol{E = h\nu = \hbar\omega = \frac{hc}{\lambda}} \qquad (2)$$

with the Planck constant h, the frequency v and the wavelength λ.
The momentum of a monochromatic electromagnetic wave is

$$\boldsymbol{p = \hbar k} \qquad (3)$$

with $\hbar = h/2\pi$ and **k** is the wave vector.

The numerical relation between the wavelength λ in Å and the Energy E in keV is

$$\boldsymbol{\lambda = \frac{hc}{E} = \frac{12.398}{E}} \tag{4}$$

The Intensity of an x-ray beam is given by the number of photons passing thorough a given area per unit time. The used x-ray detector (see Chapter 7 for experimental details) measures the intensity in counts within the used exposure time in one pixel.

6.2 X-ray diffraction

This technique is most important for investigation and determination of crystallographic structures of solid materials. Figure 17 illustrates schematically the diffraction from atomic planes of an x-ray beam in a laboratory θ-2θ geometry.

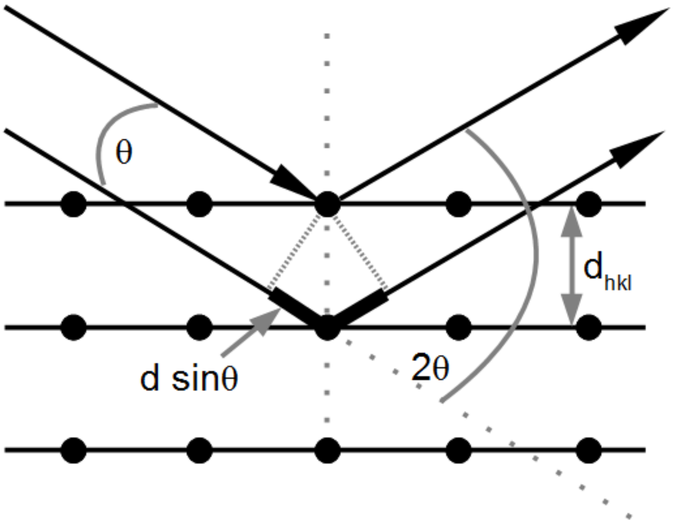

Figure 17: Schematic illustration of Bragg's law for x-ray diffraction of lattice planes in a crystal. θ is the half angle of the diffracted beam, d sin θ is the path length and d_{hkl} is the interplanar spacing. The incoming and outgoing black arrows represent the x-ray beam radiation.

This technique was used for the diffraction pattern in Chapter 4.3. The measured intensity as function of scattering angle makes it possible to determine the lattice plane distance d_{hkl} by Bragg's law:

$$\mathbf{2d_{hkl}sin\theta = n\lambda} \tag{5}$$

where λ is the wavelength of the incoming beam, θ the half angle of the diffracted beam, *n* an integer, and d_{hkl} the interplanar spacing. The recorded intensity *versus* scattering angle 2θ is displayed in a diffractogram. Bragg's law is fulfilled if the scattering of x-ray by the core electrons lead to a constructive interference. Typical diffraction peaks/reflections will be detected corresponding to certain lattice plane spacings d_{hkl}. Peak position and peak shape are a result of strain, lattice parameter, phase, grain size and composition of the crystallites.

In case of x-ray diffraction in transmission geometry (Figure 18), *full* Debye Scherrer rings are recorded with *one shot* at a polycrystalline or powder sample. With the known/measured sample-to-detector distance, and the known wavelength, the d-spacings – thus the unit cell parameters (*e.g.:* a, b, c, α, β, γ) *via* peak position – can be calculated, hence phase, strain and size analysed. Preferred orientation and porosity can be obtained, and with detailed analysis of the peak shape, statements can be made about disorder or defects in the crystal structure.

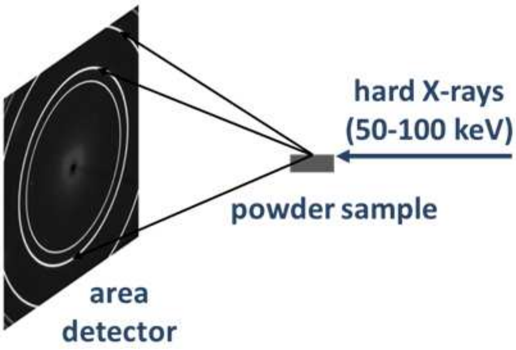

Figure 18: Schematic illustration of x-ray diffraction in transmission geometry. With one x-ray shot it is possible to gain very quickly a full diffraction pattern of a TiCrAlN powder material.

Vice versa also specific information about the radiation (wavelength), instrumental alignment, sample alignment and axial divergence [77] of the beam [78] can be obtained. This transmission configuration is able to get *very quick* detailed information about a material, *i.e.* it allows a *high temporal resolution* making it a powerful tool for following dynamic processes *in-situ*. This was indeed necessary for the annealing of powders in Chapter 8.

Figure 19 shows the 2D diffraction pattern of $Ti_{0.21}Cr_{0.39}Al_{0.40}N$ powder (a) with the corresponding radially integrated one-dimensional lineout (b).

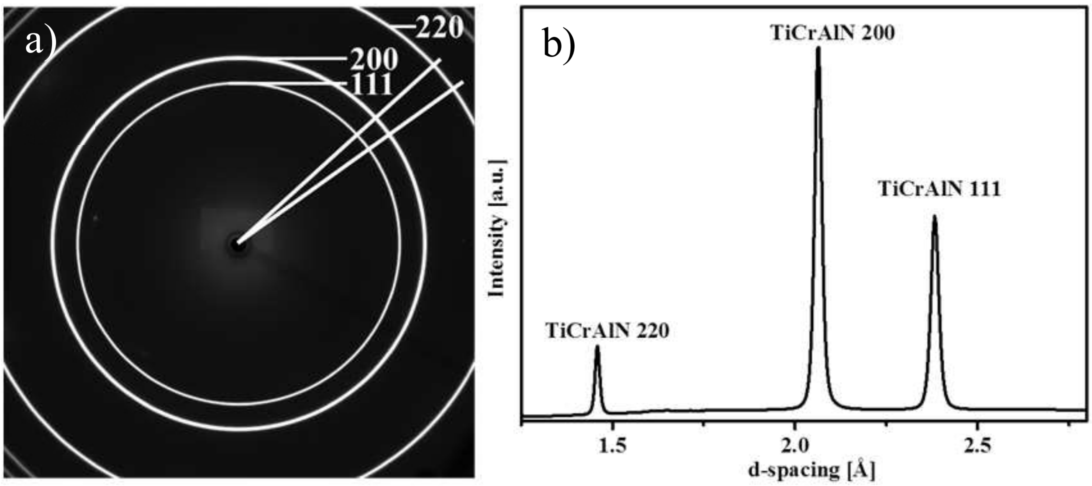

Figure 19: (a) Diffraction pattern of a $Ti_{0.21}Cr_{0.39}Al_{0.40}N$ sample recorded by a Perkin Elmer Detector XRD1622. (b) Integrated one-dimensional lineout of the two dimensional diffraction pattern of the white marked section in (a).

Here, the 1D-lineout is obtained by dividing the circle into about 5° wide sectors, then summing the intensity within those sectors. The transformed pattern is obtained by adding all 5° wide sectors of the whole 360° rings. The radial distance of the resulting transformed pattern is converted to the scattering angle 2θ and used with Eq. (6.4) to finally find the d-spacing. Here the (111), (200), and (220) reflections of as-deposited $Ti_{0.21}Cr_{0.39}Al_{0.40}N$ are shown. The broadness of the peaks is mainly due to small grains, in combination with the pixel size of the detector. A LaB_6 standard was also used to estimate the instrumental peak broadening. The peaks were fitted with a pseudoVoigt function during data analysis to calculate the peak position, peak width and integrated peak intensity (see Chapter 6.9, Analysis of the data).

6.3 *In-situ* synchrotron radiation x-ray powder diffraction (SR-XRPD)

The x-ray powder diffraction technique uses the diffraction of x-rays on crystallites in a powder sample to study the structural and microstructural properties of a material. It allows a quick and non-destructive analysis of multi-component samples [79] [80] [81]. The synchrotron radiation x-ray powder diffraction (SR-XRPD) technique is widely superior to a standard laboratory source in terms of angular resolution, counting statistic, energy tuneability, and fast acquisition time [82] [83]. The structural characterization of materials is improved by the high brilliance of the synchrotron radiation. By combining SR-XRPD with a fast detector the speed of the measurements makes it possible to perform kinetic studies on structural changes during chemical reactions or under high temperatures. In this work the high brilliance synchrotron x-ray source with a wavelength range of λ = 0,14 – 0,23 Å as described in Chapter 3 was used.

6.4 Scanning electron microscopy – SEM

Scanning electron microscopy (SEM) has been used in this thesis to study the surface as well as cross section of thin TiCrAlN films. In SEM (Leo 1550 Gemini), a focused electron beam scans the surface of the samples as a probe beam. The electron energy is usually varied between a few and several tens of keV. Due to interaction with the surface backscattered electrons, secondary electrons (SE) and x-rays are generated. By ionization of the sample, the SE are generated and the origin is close to the surface. Therefore, the detected SE are necessary to gain topographic information about the surface. The contrasts in the SEM images are due to shadowing effects.

6.5 Energy dispersive x-ray spectroscopy – EDS

During the interaction between the electron beam and the sample, the transmitting electrons knock core electrons out of the atoms. The result is an electron hole in the atom. The hole must be filled by an electron in a higher energy level to get back to the ground energy level. This energy transfer from a higher energy level to a lower energy level is accompanied by energy release in the form of an x-ray photon. The described energy transfer is characteristic for all elements and, therefore, the detection of the x-ray spectrum of the atoms yields elemental content information about the observed sample. The EDS detector was equipped in the SEM Leo 1550 Gemini. With EDS and SEM the compositions of the coatings and the cross sections of the coated WC samples were determined.

6.6 Transmission electron microscopy – TEM and STEM

An acceleration voltage of several hundred kV is used for transmission electron microscopy (TEM). In this thesis powder particles of annealed and oxidized TiCrAlN were investigated where the electrons are transmitted through the sample. The TEM requires a special sample preparation, and the probe volume must be very small. Nevertheless, it is wieldy used for coating analysis. With TEM one gains information about crystal structure, chemical compositions, and microstructure. In TEM images, a broad electron beam illuminates a selected part of the sample, which fulfills the requirements (thickness < 100 nm, and preferably *not* contaminated). The underline principle is as follows: the electrons are emitted from an electron gun and are accelerated by a potential difference in the path length. Before the electrons transmit the powder particles and after they transmit the sample, electromagnetic lenses focus the electron beam. During the interaction of the electrons with the sample, there is transmission, absorption, reflection and scattering, which are the contrast mechanisms of the resulting TEM pattern. A CCD or fluorescent screen after the sample is necessary to form an image of the electron beam. In scanning mode, TEM is sometimes called STEM.

6.7 High resolution transmission electron microscopy – HRTEM

At higher magnification, the contrast mechanisms described above are used, which produces high resolution micrographs. With HRTEM it is possible to achieve information about lattice spacing and orientation. Grain boundaries, interfaces between domains or dislocations can directly be imaged.

6.8 Selected area diffraction – SAED

The underline principle is the same for x-ray diffraction. Here, the electrons are mainly scattered by the nuclei, whereas the x-rays are scattered by the core electron of the atoms. Information about crystal structure, lattice spacing and orientation is obtained. The aberration is the limitation in electron diffraction that originates from the electromagnetic lenses. The result is a loss in the resolution for determining *e.g.* lattice spacings. With electron diffraction in TEM, a small area of the sample, *e.g.* a grain, can be selected to obtain information in the nm size range.

6.9 Analysis of the data

The main benefit using the pseudo-Voigt function in peak fitting is the direct separation of the FWHM into Gaussian and Lorentzian contributions to the peak-shape function. Those two represent two different effects: the instrumental broadening (Gaussian) and the grain size broadening from the sample specimen (Lorentzian) [78].

Figure 20 and Figure 21 show a sequel of the phase evolution of the c-TiCrAlN (111) peak (d = 2.38 Å), magnified from a diffractogram, with the pseudo-Voigt peak fitting model [84] at different selected isothermal times: a) as-deposited and before heating, d) the phase evolution after 13 min and h) the phase evolution after 125 min. This example shows only a short sequence of the oxidation process studied at 1100 °C of the c-TiCrAlN coatings. Below, the overlapping of the original c-TiCrAlN (111) peak with emerging oxides and new phases will be explained in more detail.

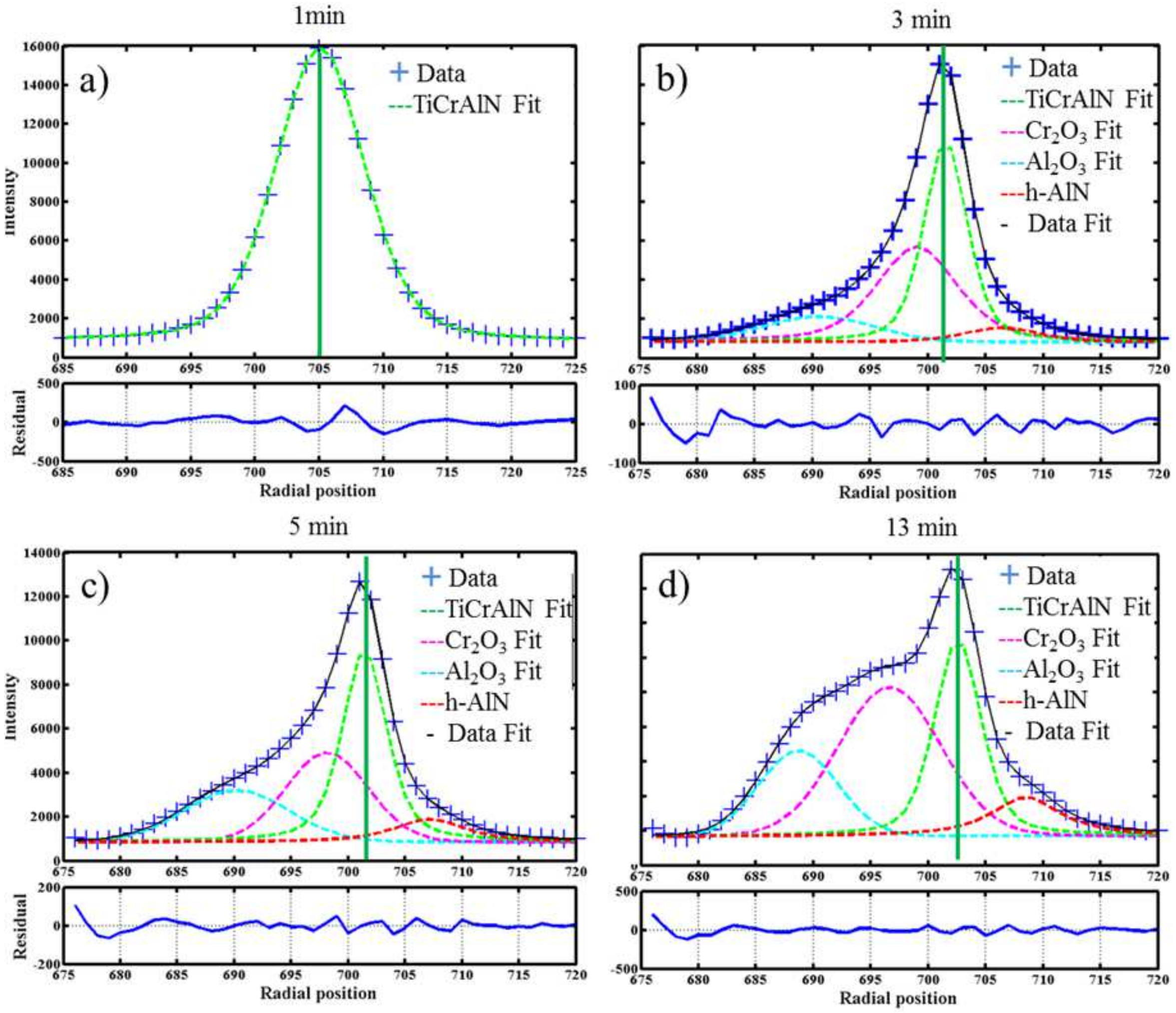

Figure 20: The peak fitting model of pseudo-Voigt functions used for data analysis to extract integrated intensities, full-width-at half-maximum (FWHM) values, and peak positions. Here, the fitting procedure of the TiCrAlN (111) peak at 2.38 Å (marked with a vertical green solid line) and additional convoluted peaks from oxides and emerging phases of $Ti_{0.16}Cr_{0.36}Al_{0.48}N$ are shown. The blue crosses represent the measured data points, the black line through these data points is the resulting fitting curve with the corresponding residuum below in blue line (x-axis is the readout of the radial bin-size position of the data points, and the y-axis gives the intensity in counts, according to the selected exposure time. The sample was annealed in air at a temperature of 1100 °C for 125 min.

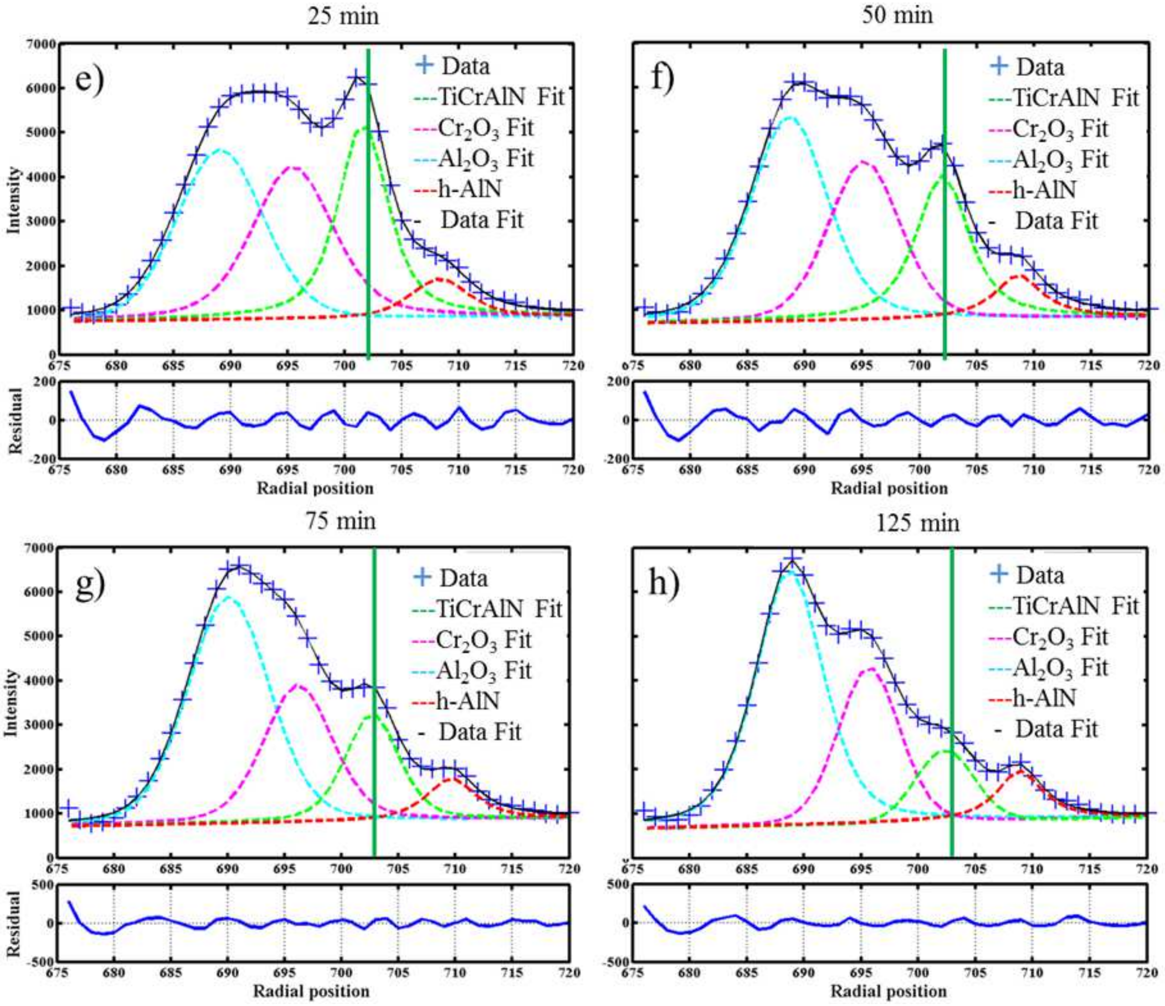

Figure 21: Continued sequel of the phase evolution of the peak fitting model of pseudo-Voigt functions of Figure 20.

In Figure 20 and Figure 21, the x-axis is the readout of the radial bin-size position of the data points (for the analysis adequate to d-spacing), and the y-axis gives the intensity in counts, according to the selected exposure time. In Figure 20 a), the green dashed line, as c-TiCrAlN, represents the peak fit model and final data fit for this isothermal time step, the blue crosses are the measured data points and the green vertical line marks the investigated peak as an example. Below each figure, the residual is depicted as the blue plot for each fitting model. In Figure 20b), new emerging phases and oxide phases show up. With further annealing time, from Figure 20b) to Figure 21h), the c-TiCrAlN peak intensity decreases whereas the intensity of the other peaks increases. Here, the dashed red, dashed blue, dashed magenta and the above mentioned dashed green peak represents the best possible pseudo-Voigt fitting model to find the best data fit (black full fit = data fit) to minimize the residuum. In this example, the dashed red line is the h-AlN phase, the dashed blue the Al_2O_3, the dashed magenta is the Cr_2O_3 and the dashed green line the above mentioned TiCrAlN. At this point it will be clear that only powder samples make the analysis possible. Overlapped peaks with the substrate and with oxide peaks of the substrate itself would make interpretation and modelling more difficult. 4 different fitted pseudo Voigt functions are used, shown in the magnified peaks in Figure 20 and Figure 21. The number of fitted peaks can be explained by the measured and observed oxides and emerging phases at other d-spacing values. For example, the Al_2O_3 and Cr_2O_3, as a convoluted peak, are also observed around 2.60 Å (Figure 22). In other words, the identified emerging phases show up at specific d-spacing values, according to their lattice constants, and are also very close to the d-spacing values of the c-TiCrAlN. Here, this is the case for the convoluted $(Cr,Al)_2O_3$ and the h-AlN. In the literature [52] [85], *ex-situ* oxidation experiments on TiCrAlN with different compositions were performed and a good agreement of the observed phases are found. In addition to that, typical databases JCPDS, crystallography open database, etc. were used to identify the peaks in the diffractograms (see Chapter 8).

At this point the outstanding advantages of *in-situ* SR-XRPD method become clear. With the outperforming angular resolution of the synchrotron radiation, the evolution of oxide phases can be studied separately. Figure 22 presents the raw data of a convoluted $(Cr,Al)_2O_3$ peak magnified from a diffractogram (*e.g.* Chapter 8). The right side presents the time scale of the evolution of the peak. From the magnified lineout it is obvious that the increase in the peak intensity is fast in the onset of the transformation and slows down with time. Compare for example the evolution between ad (as-deposited) and 12.5 min, and 12.5 min and 25 min. This evolution of the oxide peak is shown in Figure 23. Here, the intensity of both peaks is plotted for 1000 °C. A plateau can be seen. This behavior can be compared with the Figure 21. The dashed blue line, the Al_2O_3, grows with the isothermal time whereas the dashed magenta line, the Cr_2O_3, stops to grow. The convoluted oxide peaks show the same behaviour. Because the intensity depends on *e.g.* illuminated volume of the powder sample, the intensity can vary between the different measurements (here not shown) and therefore a direct comparison is not possible. Hence, this circumstance will also affect the cubic phase of as-deposited state of the TiCrAlN.

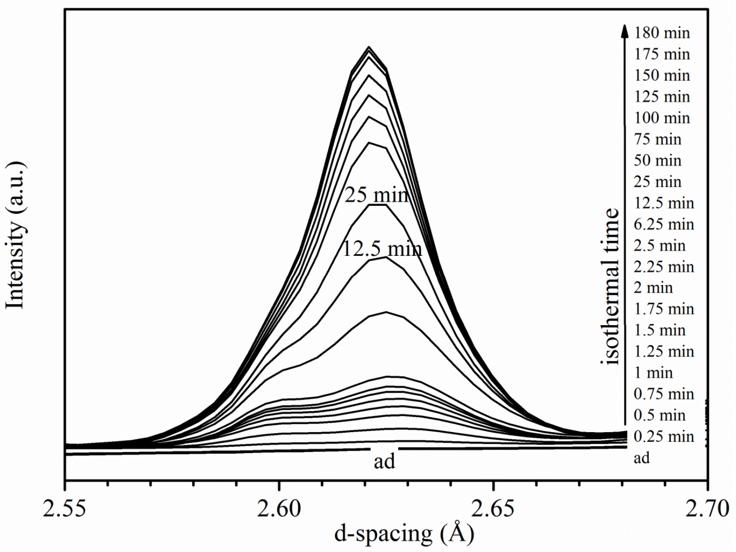

Figure 22: Integrated data lineout of the measured diffraction pattern of a convoluted $(Al,Cr)_2O_3$ peak with selected time steps of $Ti_{0.16}Cr_{0.36}Al_{0.48}N$ at 1000 °C. The peak grows with the isothermal time.

This problem can be overcome by normalizing the intensity data to get the fraction values of the emerging oxide phases and other phases. The measured intensity is divided by the intensity of the cubic (200)-TiCrAlN as-deposited peak of the measured sample [4]. The result of the described calculation is shown in Figure 23: the normalized integrated intensity or Integr. intensity norm. Further, this operation is used to calculate the fraction transformed value in Chapter 8.6 for the h-AlN. In this case, an annealing vacuum setup was used to obtain the fraction transformed value for a possible comparison between annealing in vacuum and oxidation atmosphere. Additionally, the fraction values were used to gain kinetic information.

For the kinetic analysis the raw data have to be prepared for further analysis. In Figure 22 the convoluted $(Al,Cr)_2O_3$ peak is magnified. Both oxide peaks start to grow after 30 seconds, in which the temperature reaches 1100 °C. After reaching 1100 °C the peak rapidly grows with time at the beginning and slows down with time. For a better comparison, the intensity grows fast between ad and 12.5 min compared to 12.5 min till 25 min. Furthermore, the peak intensity at 2.62 Å (Al_2O_3) increases with isothermal time and after 20 min the peak dominates over the Cr_2O_3 peak at 2.60 Å. At that point both peaks are overlapped. In Figure 23 this situation is revealed. The Cr_2O_3 peak reaches its maximum value after 7 min and gets in saturation whereas the Al_2O_3 peak slowly continues to grow.

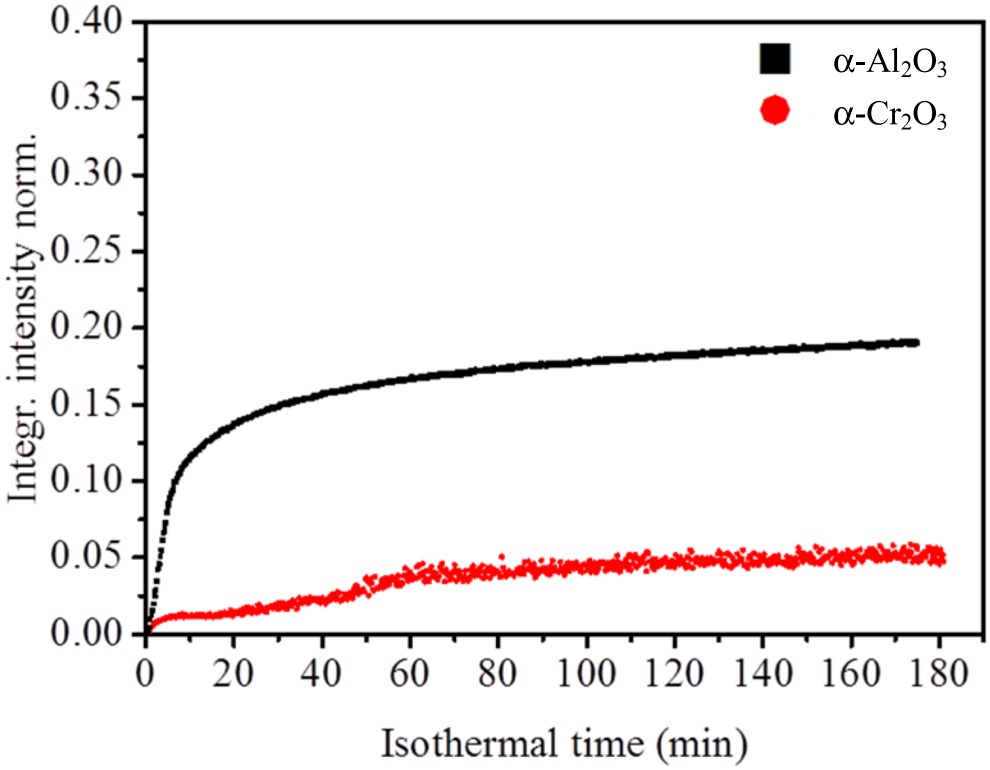

Figure 23: Integrated intensity normalized extracted from the diffraction lineout of Figure 22. The α-Cr_2O_3 peak gets in saturation, whereas α-Al_2O_3 slowly continues to grow.

From Figure 23, the integrated intensity values were used and normalized with fully transformed values of the formed oxides. This fraction values were used to analyze the growth kinetics of oxides in section 8.5.

Chapter 7

7. Experimental setup – *in-situ* measurements

This Chapter gives a short overview about the self-designed oxidation setup, the experimental details and the parameters used to perform the SR-XRPD measurements.

7.1 Custom-designed thermal annealing setup

To simulate the conditions in a high performance cutting tool, fast heating rates are necessary.

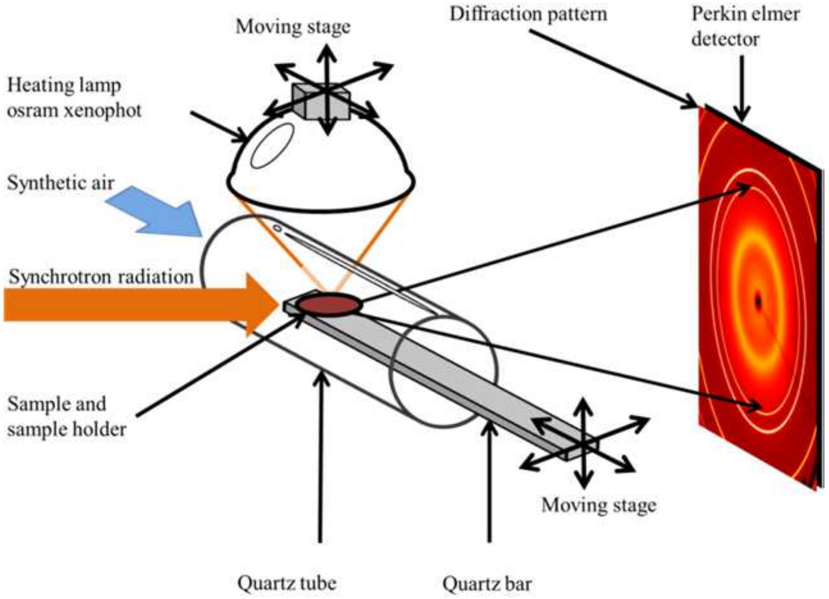

Figure 24: Schematic illustration of the custom-designed annealing setup for fast heating of $(Ti_xCr_yAl_z)N$ powders. The fast heating was performed with an Osram Xenophot® lamp mounted above the powder sample. On the right side is the diffraction pattern from the powder sample. This setup was used for the *in-situ* SR-XRPD measurements.

For this purpose, a self-designed thermal annealing setup was designed and constructed. It consists essentially of an Osram Xenophot® heating lamp (MR16 64635 HLX [86]), a quartz tube, quartz rod, and synthetic air (Figure 24).

With small moving stages the lamp can manually being moved to bring the sample into the focus of the parabolic reflectors. The device was placed into the diffractometer of the Test Facility EH1, in order to bring the sample into the x-ray beam.

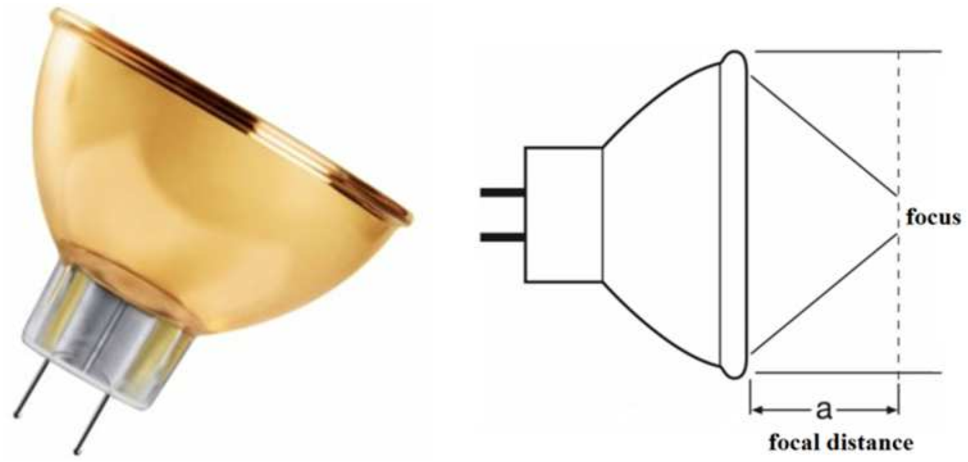

Figure 25: (left) Gold coated Osram Xenophot® lamp MR16 64635 HLX. (right) Scheme of the beaming characteristic with focal distance a = 2 cm.

The Osram Xenophot® lamp is a special low voltage halogen lamp with a gold coated parabolic reflector, which optimizes the focusing of the infrared part of the emitted light spectrum. According to specifications, inside the focus one should reach ~1300 °C with a focal distance of a = 2 cm and maximum power of 150 Watt. The lifetime reaches under full power approximately 50 hours (Figure 25). For the temperature measurement, the lamp was connected to a variable power supply (maximum output: 20 V, 15 A) and the tip of a k-type thermocouple was placed in the focus of the lamp inside the quartz tube as shown in Figure 26. Figure 27 gives a typical calibration curve: the manufacturer´s specification deviates from the measured values. In order to reach the maximum temperature of 1250 ^{o}C, one had to power the lamp to around 200 Watt, which drastically reduced the lamp´s lifetime. One explanation of this variance could be the high resistance of the used electric cable and therefore the high power output. In addition to that, the quartz tube shows a low absorption of ~5% of the transmitted heating radiation of the lamp. Furthermore, the gas flow also reduced the measured temperature. These circumstances require an increase of the power output to more than 150 Watt.

Both, the lamp and the thermocouple were mounted on a 3 axis moving stage system. For the optimization of the focal point, the thermocouple was placed in the quartz tube close to the focal point of the lamp as described above. By using the 3 axis moving stage of the Osram Xenophot®, the focal point could be exactly determined with a temperature readout controller. The optimum focal point is found if the temperature controller shows the maximum value of the measured temperature with a fixed power value.

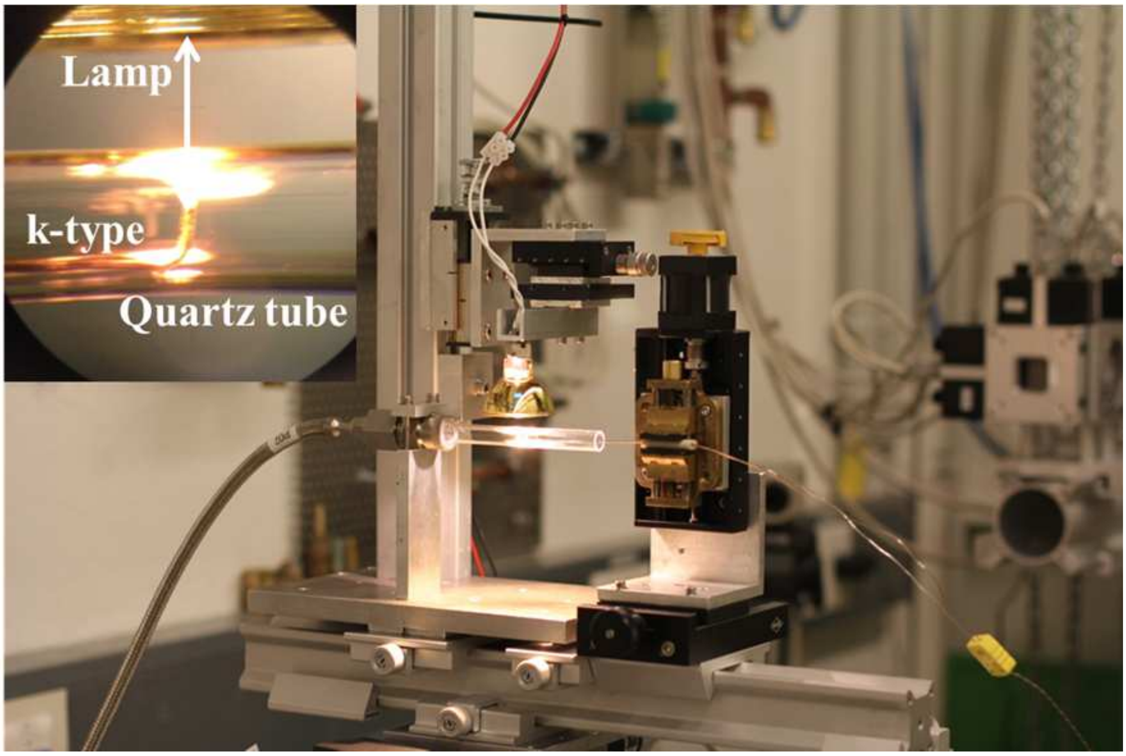

Figure 26: Annealing setup for temperature calibration at beamline P07B with a k-type thermocouple mounted in the lamp focus.

Notabene, this furnace setup was also successfully used for annealing CaO-CoO thin films in another joint collaboration with the University of Linköping, where the mechanisms of the formation of thermoelectric layered cobaltate $Ca_3Co_4O_9$ was thoroughly studied. The maximum temperature used for this later study was up to 1120°C with the heat ramping of 8 K min^{-1} [87][2].

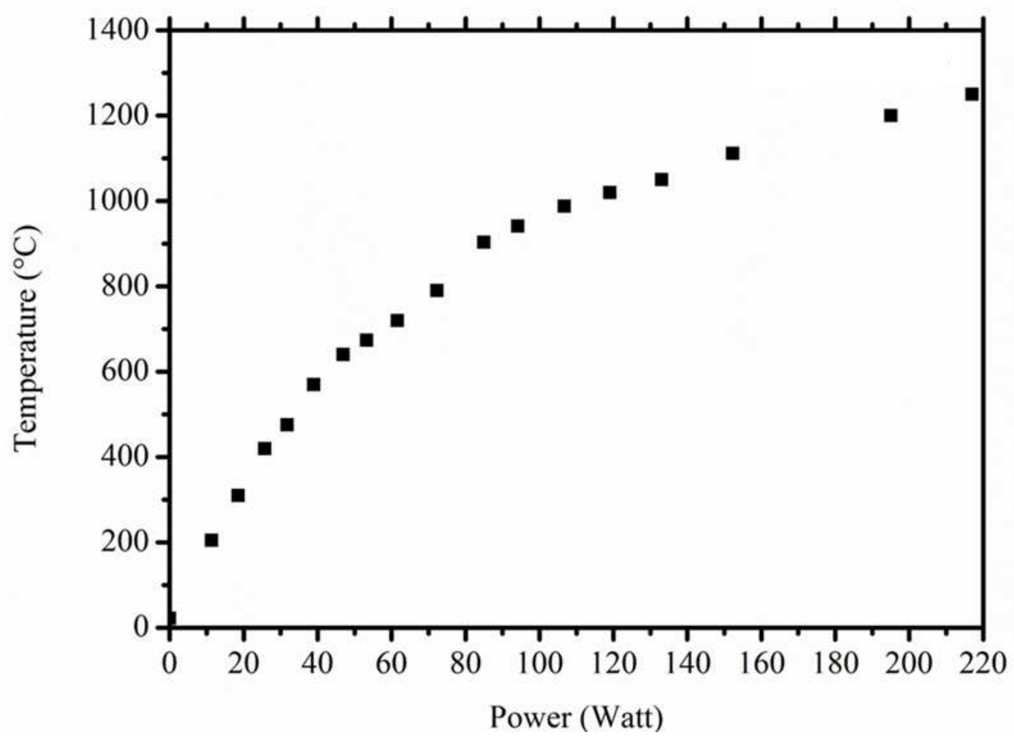

Figure 27: Characteristic curve of the temperature against the used power output.

7.2 Furnace in oxidation atmosphere – parameters used

The powder sample was put on a half open Al_2O_3 cylindrical holder with a radius of ~0.8 mm. For the experiment, the powder sample was inserted into the quartz tube *via* a quartz rod to the exact same position of the k-type tip contact for temperature calibration. The quartz tube itself is highly mechanically and thermally stable, and, therefore, suitable for these annealing experiments. The position of the holder was determined by a theodolite. The atmosphere around the sample was controlled *via* a continuous low flow of 100 sccm (standard cubic centimeters per minute) of synthetic air through the quartz tube regulated by a mass flow controller (MFC). Before connecting the MFC, a pressure regulator was installed to set the right pressure of

---

[2] P. Biplab, J. L. Schroeder, S. Kerdsongpanya, N. V. Nong, N. Schell, D. Ostach, J. Lu, J. Birch and P. Eklund, "Mechanism of Formation of the Thermoelectric Layered Cobaltate Ca 3 Co 4 O 9 by Annealing of CaO–CoO Thin Films," *Adv. Electron. Mater.,* vol. 1, p. 1400022, 2015.

maximum ~1.5 bar. Therefore, one side of the quartz tube was directly connected with the synthetic air gas hose pipe. The temperature ramping was done manually with the connected power supply and a watch. The ramping time was ~40 sec to get the maximum temperature of 1000°C, 1100°C and 1250°C. All SR-XRPD measurements were performed at the HEMS beamline P07B. The x-ray energy was set to 53.7 keV and the slit-defined beam size was 0.5 x 0.5 mm^2. The x-ray diffractograms were captured with 5 sec exposure times using the two-dimensional area detector Perkin-Elmer XRD 1621 with a pixel size of 200 µm x 200 µm. The detector was positioned 1418 mm from the sample.

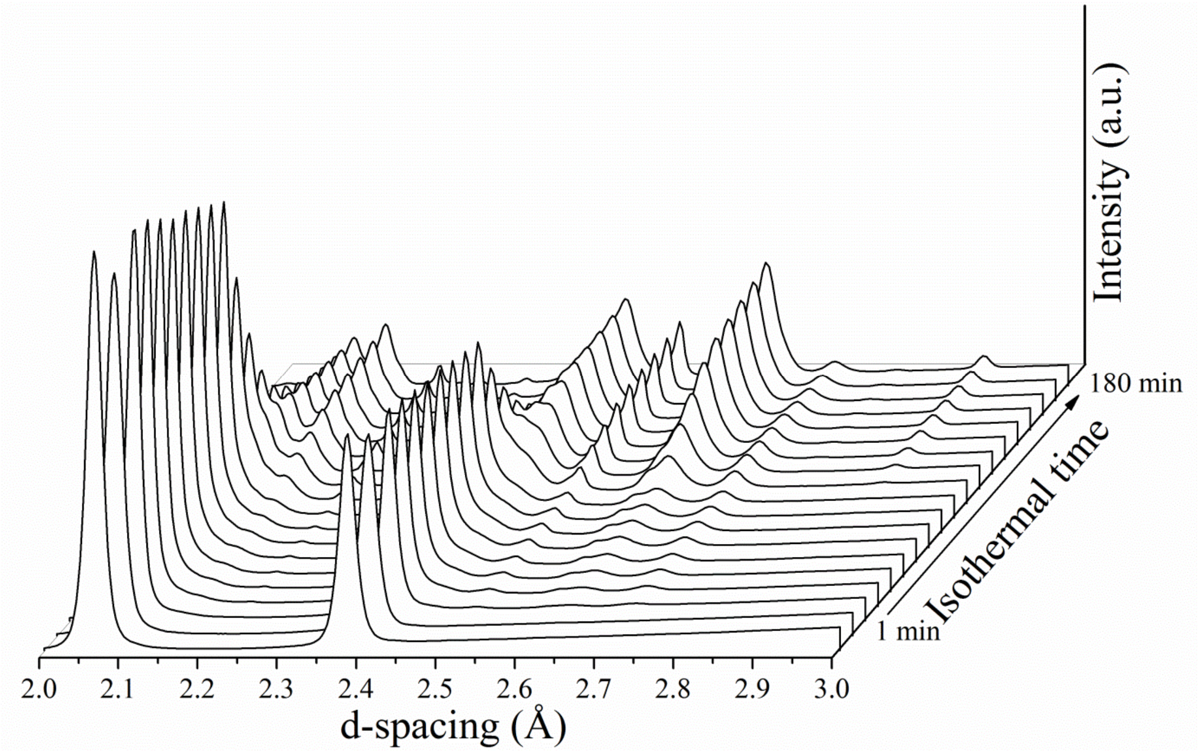

Figure 28: Time selected diffractogram of the in-situ SR-XRPD measurements of TiCrAlN powder.

Figure 28 visualizes 1D-lineouts for various annealing times of the diffraction patterns. The procedure is described in Chapter 6.2. In the following chapter the phase evolution, the oxide growth and the oxidation process is described providing kinetic information on the TiCrAlN samples

Chapter 8

8. Results

The experiments performed in this thesis are very closely related to a real-time cutting situation. To understand the oxidation behaviour of TiCrAlN coatings during the cutting process, I investigated the growth of oxides and related oxidation mechanisms by using *in-situ* SR-XRPD. According to my knowledge, this high temperature *in-situ* SR-XRPD real-time oxidation experiment on TiCrAlN material system has not been reported in the literature yet.

The TiCrAlN powders were extracted from the coated iron foils. Compared to the coating on a substrate, the powder offers much larger surface area for the oxidation reaction and, therefore, some results might not have direct correspondence to a real-time cutting process. However, the advantages of the powder are a stronger signal to noise ratio for easier analysis of the diffraction signals, and because there are no coating-substrate reactions it is the best way to study the phase evolution. Therefore, TiCrAlN powders were used to perform *in-situ* SR-XRPD. In addition to that, *in-situ* SR-XRPD vacuum annealing experiments on TiCrAlN powder were also performed to investigate long-term effects. Additionally, I have performed annealing experiments in an air atmosphere with TiCrAlN composition on a WC-Co substrate. A real-time oxidation situation with fast annealing in air at 3000 K min^{-1} led to a bending of the substrate and the coating and, therefore, to a misalignment of the sample out of the optical axis of the synchrotron radiation (see Chapter 5).

This Chapter presents the results of the *in-situ* SR-XRPD real-time oxidation measurements. The first section summarizes the qualitative analysis of the SR-XRPD lineouts. The second section summarizes the results of the annealing *in-situ* WAXS experiment in vacuum which have been submitted for publication. The third section illustrates the quantitative analysis of the *in-situ* oxidation behaviour of the coating. The fourth section summarizes the *in-situ* SR-XRPD oxidation measurements of the oxides. The fifth section presents the kinetic reaction analysis. The sixth section gives a brief comparison to h-AlN evolution in vacuum and the seventh section summarizes the relationship between coating, the oxide growth and the behaviour of the h-AlN.

8.1 SR-XRPD lineouts

Figure 29 shows x-ray diffractograms in the d-spacing range from 2 Å to 3 Å of the powder samples $Ti_{0.16}Cr_{0.36}Al_{0.48}N$ of the real-time oxidation process at 1000 °C [88].

The peaks in as-deposited (a.d.) $Ti_{0.16}Cr_{0.36}Al_{0.48}N$, at d = 2.38 Å and d = 2.06 Å, are detected corresponding to c-TiCrAlN (111) and (200) [52] [20], while no other phases are observed. The lattice constant is a = 4.12 Å and agrees with the estimated lattice parameters [33]. These peaks are shifted to higher d-spacing values within 0.75 min which indicates a thermal expansion.

After reaching 1000 °C, the peak intensity of the c-TiCrAlN phase starts to decrease rapidly and slows down with time until it is totally vanished after ~180 min. However, for (111) and the (200) peak, a low peak intensity can be still detected after ~120 min. At the same time of the decrease of the peak intensity of the c-TiCrAlN, convoluted peaks originating from α-Al_2O_3, α-Cr_2O_3 and α-$(Cr,Al)_2O_3$ at d = 2.62 Å, d = 2.44 Å, d = 2.12 Å start to grow after 0.75 min. These convoluted peaks are also observed in an *ex-situ* oxidation process of TiCrAlN [52] [20]. It is seen that the convoluted peaks, corresponding to α-Cr_2O_3 (d = 2.60 Å) and to Al_2O_3 (d = 2.62 Å), grow together. With further isothermal time the peak intensity at d = 2.62 Å grows much stronger compared to the peak intensity at d = 2.60 Å. After 180 min the peaks are overlapped and only one broad peak is detected. The dominating peak here is the Al_2O_3 at d = 2.62 Å. Weak peaks belonging to the TiO_2 phase can be also detected at d = 2.49 Å, d = 2.32 Å, d = 2.21 Å, and d = 2.07 Å which are also observed in an *ex-situ* oxidation experiment of TiCrAlN [52] [20]. The onset of the forming of TiO_2 phase has a time delay of 0.5 min compared to the α-$(Cr,Al)_2O_3$. The time delay is more clearly seen at d = 2.32 Å. Eventually, high intensity peaks belonging to α-Al_2O_3 at d = 2.45 Å and d = 2.15 Å can be also detected. Additionally, asymmetric or overlapped peaks of h-Cr_2N and α-Al_2O_3 also appear. The h-Cr_2N phase was found during c-Cr phase formation in decomposed TiCrAlN and CrAlN coatings [52] [20] [85] [48]. However, c-Cr was not observed in my x-ray diffractograms.

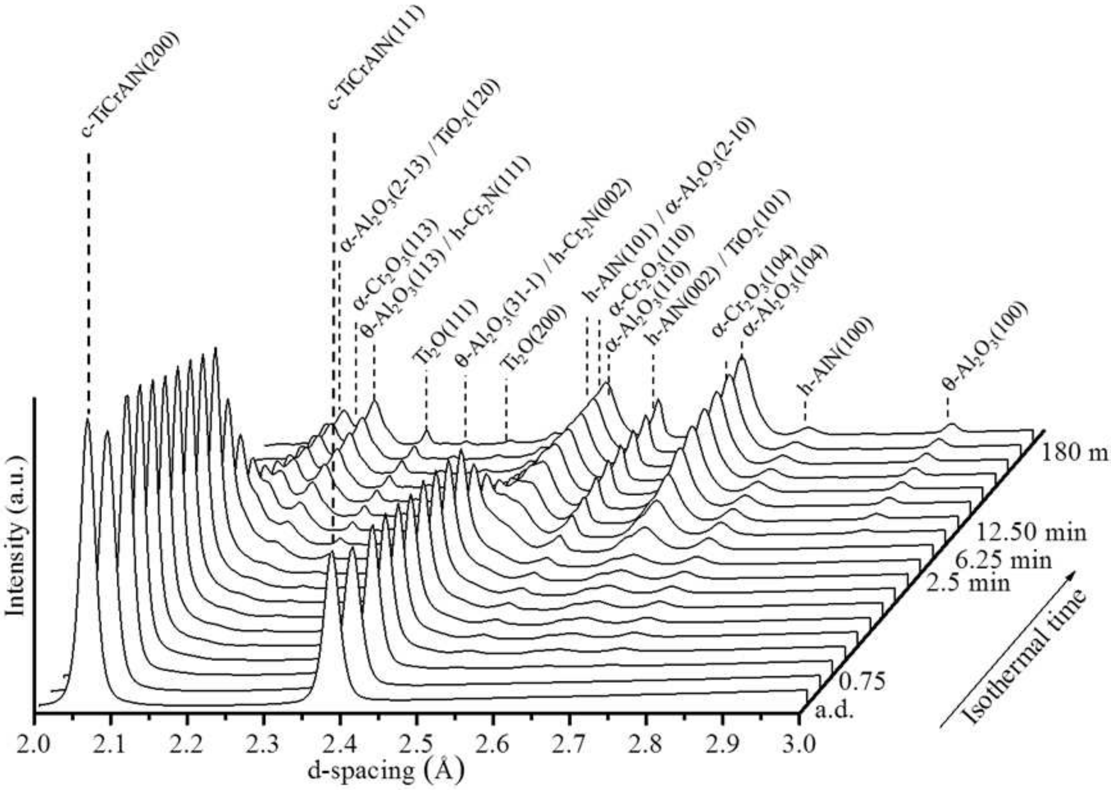

Figure 29: The *in-situ* x-ray diffractogram of $Ti_{0.16}Cr_{0.36}Al_{0.48}N$ in the range from 2 Å to 3 Å of the as-deposited samples (a.d.), after heating in air up to 1000 °C with a heating rate of 3000 K min^{-1} (0.75 min), and after isothermal times with additional selected indicated time steps [88].

After 0.75 min, peaks at d = 2.71 Å and d = 2.51 Å are detected corresponding to h-AlN phase, (100) and (002). The h-AlN phase formation was also observed in *ex-situ* annealing experiments of TiAlN, CrAlN and TiCrAlN [4] [20] [35] [89]. During further isothermal times an additional peak at d = 2.38 Å belonging to h-AlN (101) can also be detected (see Chapter 6.9, the red dashed line). After 11 min, the peak intensity of the h-AlN (100) starts to decrease, whereas the h-AlN (002) does not show this behavior. It is clearly seen that the h-AlN (002) peak is asymmetric. This suggests overlapped peaks originating from the above mentioned TiO_2 phase and the h-AlN phase. After ~180 min both peaks are overlapped and only one clear peak at d = 2.51 Å can be detected, which indicates that this peak is dominated by a TiO_2. After 14 min, the peak intensity of the h-AlN (101) starts to decrease and shows the same behavior like h-AlN (100) but with a short time delay of 3 min. At the same time of the decrease of the h-AlN phase, a new phase starts to growth at d = 2.89 Å and d = 2.26 Å after 11 min of annealing which is identified as θ-Al_2O_3 phase. Here, a transformation takes place from h-AlN into θ-Al_2O_3, which was also observed in an *ex-situ* oxidation process of CrAlN [90].

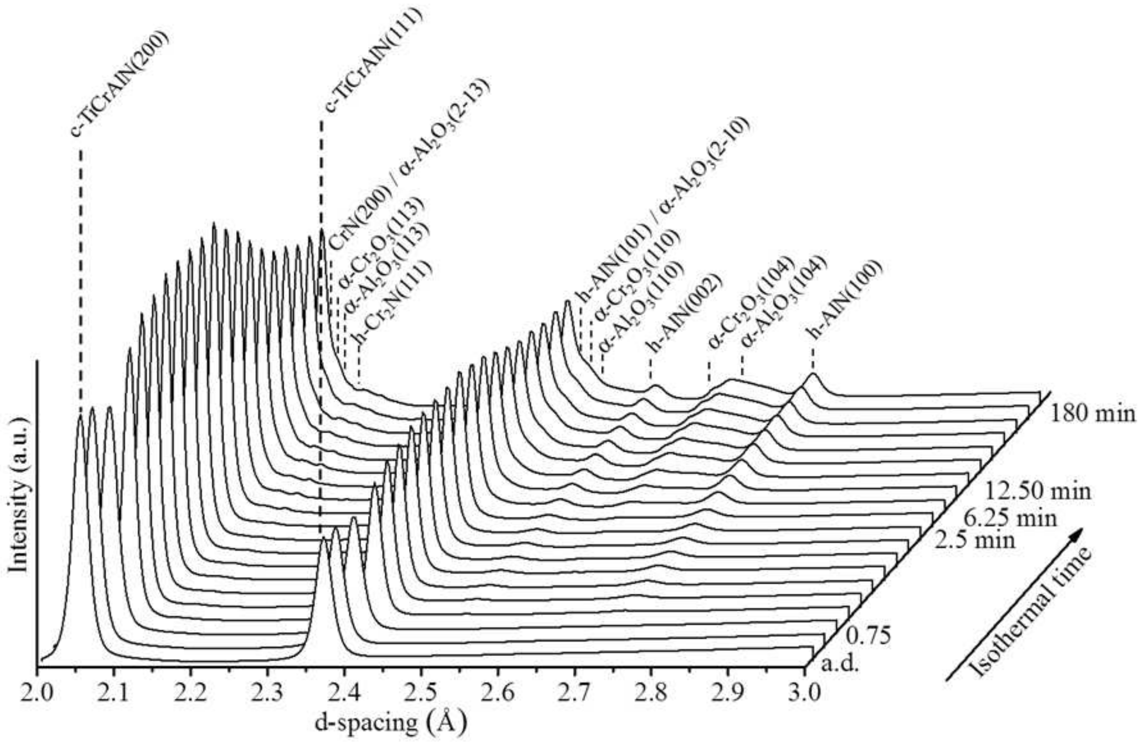

Figure 30: The *in-situ* x-ray diffractogram of $Ti_{0.03}Cr_{0.38}Al_{0.59}N$ in the range from 2 Å to 3 Å of the as-deposited samples (a.d.), after heating in air up to 1000 °C with a heating rate of 3000 K min^{-1} (0.75 min), and after isothermal times with additional selected indicated time steps [88].

Figure 30 shows x-ray diffractograms in the d-spacing range from 2 Å to 3 Å of the powder samples $Ti_{0.03}Cr_{0.38}Al_{0.59}N$ of the real-time oxidation process at 1000 °C [88].

For as-deposited $Ti_{0.03}Cr_{0.38}Al_{0.59}N$, the same cubic structure is detected as seen for $Ti_{0.16}Cr_{0.36}Al_{0.48}N$, while no other phases are observed. The lattice constant is a = 4.10 Å and agrees with the estimated lattice parameters [33]. Here again, theses peaks are shifted to higher d-spacing values within 0.75 min which indicates a thermal expansion. After reaching 1000 °C, the peak intensity starts to decrease very slowly compared to $Ti_{0.16}Cr_{0.36}Al_{0.48}N$ and after 180 min the c-TiCrAlN phase is still clearly detectable compared to $Ti_{0.16}Cr_{0.36}Al_{0.48}N$. With further annealing time a convoluted peak originating from α-Al_2O_3, α-Cr_2O_3 and α-$(Cr,Al)_2O_3$ close to the c-TiCrAlN (111) and (200) can be detected. A convoluted peak originating from α-Al_2O_3, α-Cr_2O_3 and α-$(Cr,Al)_2O_3$ at d = 2.60 Å and d = 2.62 Å can be also clearly detected. In comparison to $Ti_{0.16}Cr_{0.36}Al_{0.48}N$, the onset of the growth of these convoluted oxide phases has a ~3 min time delay and no dominating peak can be established. Furthermore, the peak intensity slowly grows compared to the convoluted peak intensities of $Ti_{0.16}Cr_{0.36}Al_{0.48}N$. Before that, after 0.75 min annealing a peak at d = 2.14 Å is also detected and belongs to the h-Cr_2N phase. The peak intensity has its maximum after ~12 min. It can be seen that the α-Al_2O_3 starts to grow at first at d = 2.62 Å and ~3 min later the α-Cr_2O_3 peak at d = 2.60 Å follows. After 0.75 min, peaks at d = 2.71 Å and d = 2.51 Å are detected corresponding to h-AlN phase (100) and (002). The increase in the peak intensity of the h-AlN phase is rapid in the beginning and slows down with time. In comparison to $Ti_{0.16}Cr_{0.36}Al_{0.48}N$, the h-AlN (002) peak at d = 2.51 Å shows no asymmetric shape, so no overlapping with TiO_2 can be seen. However, the h-AlN phase formation and the growth of the oxides show a significant time delay compared to $Ti_{0.16}Cr_{0.36}Al_{0.48}N$. For $Ti_{0.03}Cr_{0.38}Al_{0.59}N$, at first the h-AlN starts to grow and after ~3 min the convoluted oxides start to grow. For 1100 °C (not shown), higher peak intensities of the oxide phases are observed for $Ti_{0.16}Cr_{0.36}Al_{0.48}N$ coatings, whereas for $Ti_{0.03}Cr_{0.38}Al_{0.59}N$ the peak intensities of the observed oxide phases are slightly higher compared to the peak intensities of the oxide phases at 1000 °C. No new phases were observed for $Ti_{0.03}Cr_{0.38}Al_{0.59}N$ and $Ti_{0.16}Cr_{0.36}Al_{0.48}N$ at 1100 °C.

Figure 31 illustrates the last lineouts of the $Ti_{0.03}Cr_{0.38}Al_{0.59}N$ at 1000 °C after 180 min annealing, at 1100 °C after 180 min annealing and the time evolution of the oxidation process at 1250 °C for selected time steps. At first sight, both last lineouts after 180 min at 1000 °C and at 1100 °C, show small differences in the evolution or changes of the oxide phases, as shortly mentioned above. However, these differences will be discussed in the next sections.

At d = 2.89 Å a new emerging phase, identified as an oxide θ-Al_2O_3 (100), starts to grow after ~2 min of annealing. This phase does not show up at 1000 °C or 1100 °C compared to $Ti_{0.16}Cr_{0.36}Al_{0.48}N$, where it shows up. At d = 2.70 Å, the h-AlN (100) shows up at 1000 °C and 1100 °C, whereas at 1250 °C, the h-AlN (100) grows rapidly within the first 2 min of annealing and then starts to decrease rapidly. Here, this supports again the transformation of h-AlN into of θ-Al_2O_3 (100) as mentioned above, but here at 1250 °C. At d = 2.60 Å, the convoluted α-Al_2O_3, α-Cr_2O_3 and α-$(Cr,Al)_2O_3$ show up. The emerging oxide phases show slightly higher intensity for higher temperatures. For 1250 °C, the convoluted peak α-$(Cr,Al)_2O_3$ shows the same behaviour as shown in Figure 29 for $Ti_{0.16}Cr_{0.36}Al_{0.48}N$ at 1000 °C. For $Ti_{0.03}Cr_{0.38}Al_{0.59}N$, both peaks grow together and after ~100 min one complete peak can be seen. At d = 2.43 Å convoluted peaks α-Al_2O_3, α-Cr_2O_3 show up. These peaks can be recognized due to the asymmetric shape of the peak at 1000 °C and 1100 °C, as shown in Figure 29 for 1000 °C. At 1250 °C, this oxide peak starts to grow clearly and after ~25 min no intensity change can be measured. For 1250 °C, the c-TiCrAlN (111) and

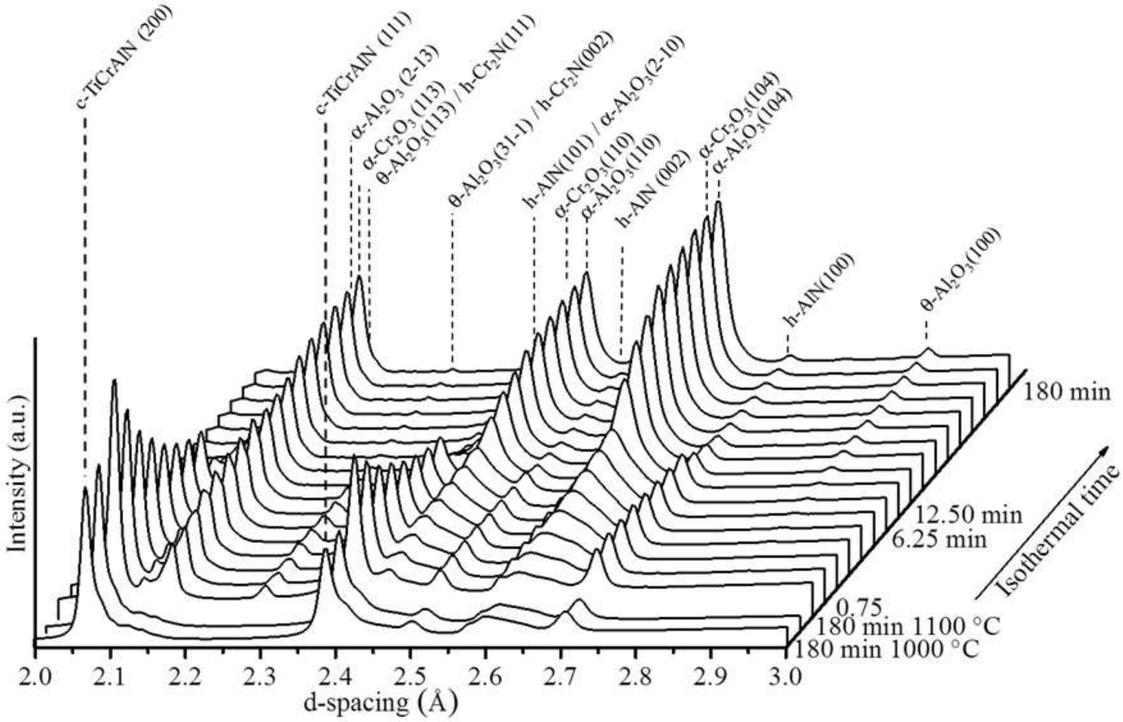

Figure 31: *In-situ* time resolved SR-XRPD of $Ti_{0.03}Cr_{0.38}Al_{0.59}N$ annealed in air at 1000 °C, 1100 °C and 1250 °C with additional indicated isothermal time steps. The first two lineouts represent the last data lineout, after 180 min at 1000 °C, and after 180 min at 1100 °C. For a better overview, the 1250 °C lineout starts after 0.75 min.

(200) peaks start to decrease whereas for 1000 °C and 1100 °C these coating peaks are still clearly detectable.

8.1.1 Discussion

The impressive result, seen directly from the lineout, is that the cubic structure for $Ti_{0.03}Cr_{0.38}Al_{0.59}N$ is clearly detectable, for 1000 °C and 1100 °C, whereas for $Ti_{0.16}Cr_{0.36}Al_{0.48}N$ the cubic structure obviously vanished after 180 min. In the literature similar phenomena were also observed for *ex-situ* oxidation experiments of c-TiCrAlN coatings with low Ti-content [20] [85], but under normal laboratory conditions. It is known, that Ti-rich TiCrAlN coatings show degraded oxidation resistance compared to Cr-rich TiCrAlN coatings. The results from my lineouts, here, are consistent with the *ex-situ* oxidation study of TiCrAlN of Forsén *et al.*, who showed a trend in the degraded oxidation resistance with increasing Ti-content in TiCrAlN coatings [20].

The observation of the oxide phases in my *in-situ* oxidation experiment agrees with early *ex-situ* studies on the oxidation resistance of TiAlN and CrAlN coatings. On the one hand, in TiAlN coatings a porous TiO_2 layer formed between the top layer Al_2O_3 and the bottom TiAlN coating due to inward diffusion of oxygen [91] [92], which reduces the oxidation resistance. On the other hand, CrAlN coatings can form a dense convoluted $(Cr,Al)_2O_3$ oxide scale on the surface which results in an effective blockage of the inward attack of oxygen and the outward diffusion of the coatings species [26] [15]. Additionally, it is known that crystalline or amorphous α-$(Cr,Al)_2O_3$ acts as good oxygen diffusion barrier [37]. These observed phenomena in the literature can partially help to describe the oxidation process here in my thesis.

Therefore, one possible explanation for the good oxidation resistance in $Ti_{0.03}Cr_{0.38}Al_{0.59}N$ is that the oxidation resistance is likely related to the formation of a thin dense convoluted protective oxide layer consisting of α-Cr_2O_3 and α-Al_2O_3 (see lineouts and description in 8.1), suppressing the further diffusion and penetration of oxygen inside the coatings [39]. This explanation is supported by the fact that only a convoluted $(Cr,Al)_2O_3$ oxide scale is formed and no TiO_2 is observed, as seen from the lineouts in Figure 29. In the literature mentioned [39], the CrTiAlN coating still retains basically its crystalline structure after oxidation at 900 °C. In my *in-situ* oxidation experiment, the $Ti_{0.03}Cr_{0.38}Al_{0.59}N$ sample retains its cubic structure after oxidation at a much higher 1100 °C. The difference in the temperature is due to different compositions and microstructure, powder used here, and coating on steel substrate used in [39].

In *e.g.* TiAlN, the promotion of α-Al_2O_3 has been suggested to be the reason for the improved oxidation resistance with increasing Al-content in *ex-situ* oxidation experiments [7] [8] [15] [93]. However, the higher Al-content is not mirrored in the XRD-lineouts of $Ti_{0.03}Cr_{0.38}Al_{0.59}N$. The thin α-$(Cr,Al)_2O_3$ protective layer observed in $Ti_{0.03}Cr_{0.38}Al_{0.59}N$ is clearly more effective (to maintain the cubic structure) compared to TiO_2, as seen in the lineouts with higher Ti-content ($Ti_{0.16}Cr_{0.36}Al_{0.48}N$) and in the lineouts with low Ti-content ($Ti_{0.03}Cr_{0.38}Al_{0.59}N$). Similar observations were also made by Forsén *et al.* [20].

It is known that with increasing Ti-content the oxidation resistance becomes worse [20]. The porous TiO_2 benefits the inward diffusion of the oxygen and this attacks the $Ti_{0.16}Cr_{0.36}Al_{0.48}N$ coating and leads finally to the promoted growth of the α-Al_2O_3 phase, as seen in the $Ti_{0.16}Cr_{0.36}Al_{0.48}N$ coating.

TiO_2 formation can be associated with compressive and local stress generation during its formation leading to crack formation in the oxide layer [91] [92] which results in a reduced protection [93]. Therefore, the promotion of porous TiO_2 affects the oxidation resistance negatively. Remember Figure 13 on page 25. The bending of the sample with higher Ti-content can be likely associated with this explanation, whereas no bending is observed in the coating with low Ti-content. The reaction between the coating and the substrate plays also a role and will be not discussed here.

The onset of the oxidation process starts at the same time when the mentioned convoluted oxide peaks and new emerging oxide peaks start to grow, and simultaneously, when the peak intensity of the cubic structure starts to decrease. The coating $Ti_{0.03}Cr_{0.38}Al_{0.59}N$ shows a time delay of ~3 min annealing, at 1000 °C. No oxide growth and no decrease of the cubic structure are observed within ~3 min. Furthermore, the fact that the h-AlN phase transformation appears demonstrates two important facets.

The h-AlN phase appears at 1000 °C at first and then the oxide scale grows. Secondly, the appearance of the h-AlN phase formation indicates a decomposition of c-TiCrAlN, which was also observed in TiAlN, CrAlN and TiCrAlN [4] [20] [35] [89].

At this point it has to be mentioned that from the annealing experiments in TiAlN, CrAlN and TiCrAlN in [4] [20] [35] [89] it is known, that the peak intensity of the cubic structure can also decrease, but due to the decomposition process. Therefore, in my *in-situ* oxidation experiment the decrease in the peak intensity of the cubic structure indicates mainly an oxidation process, due to the simultaneous growth of oxides, and obviously additionally a decomposition of the c-TiCrAlN, in both compositions.

However, only the h-AlN phase of the decomposition products appears. We will see in section 8.2, that in the *in-situ* vacuum annealing experiment more decomposition products appear.

With the outstanding *in-situ* SR-XRPD method it is possible to measure the phase evolution of the oxide phases, the coating and the h-AlN phase separately. This is not possible with a normal x-ray lab source. At this point the problem with overlapped peaks must be discussed. In the literature [20] [52] [85], the identified oxide phases of the XRD measurements are often overlapped with other phases due to the very close lattice constant. A 100 % identified phase is not possible and a correlation is very difficult. This fact is also true for the synchrotron radiation data. For example, in the literature [85] the h-AlN is overlapped with the Al_2O_3 or TiO_2 at one specific d-spacing range, as shown here in this section. However, from higher resolution of the synchrotron radiation data, the evolution of convoluted oxide peaks could be analyzed separately in combination with peak fitting procedure.

The major difficulty for the quaternary TiCrAlN system is to find the origin of the oxidation mechanism and its inner working. For example, J. Lin *et al.* have reported an improved oxidation resistance in $Ti_{0.10}Cr_{0.61}Al_{0.29}$ (coating on bulk annealed at 1000 °C). One explanation is that the improved oxidation resistance is likely related to a strong preferred orientation of the coating.

These kinds of explanations are not sufficient and provide only an assumption of the improved oxidation resistance related to the observations. Summarizing the literature, many explanations to describe the oxidation process in quaternary TiCrAlN are mostly suggestions or assumptions and based on the well known ternary systems TiAlN and CrAlN. Therefore, it is important for the cutting industry (*e.g.* SECO Tools, LMT Fette Werkzeugtechnik) to understand, why the TiCrAlN coating shows superior properties, and to find out enhanced explanations for the oxidation process and also for other mechanisms like hardness, thermal stability, etc.

8.2 *In-situ* SR-XRPD in vacuum

As described in the introduction of Chapter 8, to approach a real cutting situation, we also performed annealing experiments in vacuum [94], besides the real-time oxidation experiment in air. Only long-time effects were measured and they cannot really replace a real cutting situation, but, these experiments are also a methodological approach to find out what effects can appear in coatings of a cutting tool, which mechanisms, which phase transformation, thermal stability, etc.. In this following section 8.2 the results and the description of the experimental setup, taken from [94], are presented. The background of this vacuum experiment is as follows.

Cubic c-$Ti_{1-x}Al_xN$ coatings are extensively used in hard metal cutting tool inserts due to their superior mechanical properties [95]. The high hardness after exposing the coating to high temperatures is related to spinodal decomposition [12] [13] [14] [20] [96] [97] resulting in c-TiN and c-AlN rich domains where the variations in elastic properties and the strain between domains give rise to age hardening. However, the subsequent transformation of c-AlN to hexagonal h-AlN following the spinodal decomposition [96] reduces the mechanical properties of the alloy due to loss of coherency between c-TiN and c-AlN domains [98] [99]. Therefore, to enhance thermal stability the h-AlN phase formation has to be suppressed during decomposition, and this was also demonstrated in TiAlN multilayers [10] [49] or in other quaternary systems [20] [33] [40]. Introducing Cr leads to lower coherency strain between Ti- and Al-rich domains [10] [48], and the detrimental effect on the mechanical properties by h-AlN formation is also less strong due to formation of semi-coherent interfaces between h-AlN and c-TiCrN domains [20] [48] [49]. The addition of Cr in TiCrAlN-alloys has shown to yield superior mechanical properties after high temperature annealing and wear resistance compared to TiAlN [40] [39], also as mentioned in Chapter 2.3.

In particular, Forsén *et al.* describe two co-occurring and competing decomposition mechanism for $Ti_{0.11}Cr_{0.28}Al_{0.61}N$. One mechanism is the precipitation of the h-AlN domains at the grain boundaries, the observed decomposition route in CrAlN coatings [100] [20]. The other mechanism is the spinodal decomposition route of the grain interiors into TiCr- and Al-rich c-TiCrAlN domains which are similar to the observed decomposition route in TiAlN coatings [12] [13] [14] [20] [96] or in TiCrAlN coatings [48]. Consequently for $Ti_xCr_{1-x}Al_{0.61}N$, there is a transition of the decomposition process from nucleation and growth process of h-AlN precipitates at grain boundaries for $x = 0$ to a spinodal decomposition route of the grain interiors into TiCr- and Al-rich c-TiCrAlN domains $x = 0$ [20]. With the condition $0 < x < 1$ for the compositions, these two mechanism are co-occurring and one may dominate over the other depending on x [20].

Therefore, the formation of h-AlN still limits the high temperature properties and the details regarding its transformation is lacking. Summarizing, the evolution of the h-AlN and the decomposition process of the c-TiCrAlN are investigated in this vacuum experiment.

In this annealing experiment the same powder samples a.d. $Ti_{0.16}Cr_{0.36}Al_{0.48}N$ and a.d. $Ti_{0.03}Cr_{0.38}Al_{0.59}N$, as described in Chapter 8.1, are annealed in a vacuum furnace. The *in-situ* x-ray scattering experiments were performed at PETRA III P07, DESY in Hamburg using an 80 keV x-ray beam with a defined slit size of $500 \times 500\ \mu m^2$. Isothermal anneals were carried out at a working pressure of 1.6 mPa for 3-5 hours and isothermal annealing temperatures (T_{max}) were between 1000 °C and 1150 °C with a heating and cooling rate of $20\ K\ min^{-1}$. The x-ray beam was let through the vacuum chamber by x-ray transparent viewports, and the diffracted x-rays were recorded with a two-dimensional area detector (Perkin Elmer) with a pixel size of 200 by $200\ \mu m^2$. The detector was placed 2155 mm from the sample and an exposure time of 4 s was used. In Figure 32, the intensity *versus* d-spacing lineouts generated from two-dimensional exposures (as described in Chapter 6.2) are shown for selected annealing temperatures and times. For a better presentation of the decomposed phases, only a part of the data is shown, *i.e.* centered at the c-TiCrAlN 220 and h-AlN 100 signals. In the lineout, both $Ti_{0.16}Cr_{0.36}Al_{0.48}N$ and $Ti_{0.03}Cr_{0.38}Al_{0.59}N$ display only the c-TiCrAlN phase in the as-deposited state and the lattice constants are $a(Ti_{0.16}Cr_{0.36}Al_{0.48}N) = 4.12$ Å and $a(Ti_{0.03}Cr_{0.38}Al_{0.59}N) = 4.10$ Å, as already mentioned in section 8.1. After ramping the temperature to 1150 °C, additional peaks from the h-AlN phase appear, indicating decomposition of the c-TiCrAlN phase. This phase also appears in my real-time

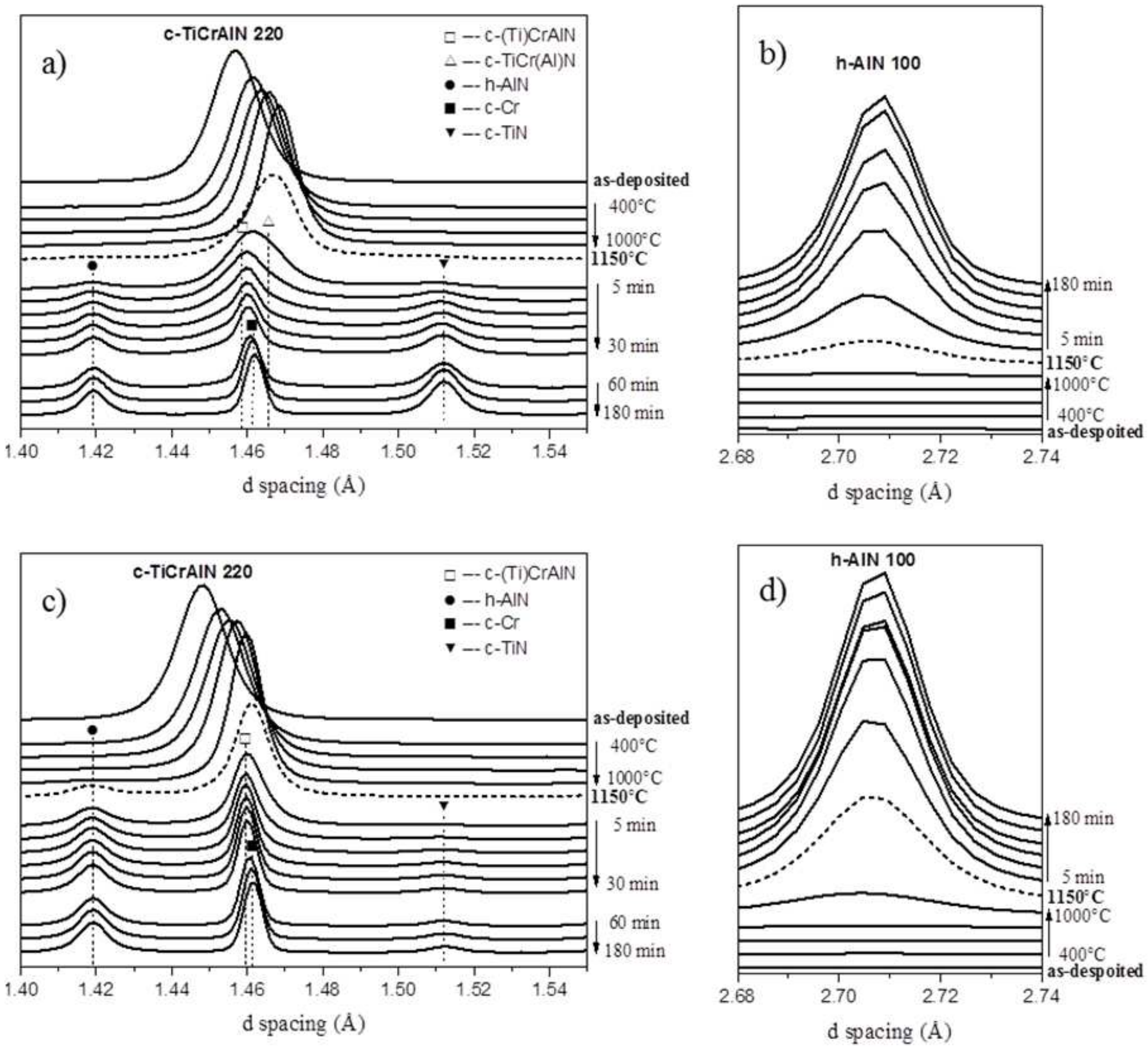

Figure 32: Lineouts of the samples (a,b) $Ti_{0.16}Cr_{0.36}Al_{0.48}N$ and (c,d) $Ti_{0.03}Cr_{0.38}Al_{0.59}N$ while ramping to 1150 °C (dashed line) with 20 K min^{-1} and holding for 180 min. Illustrated are the (b,d) h-AlN and (a,c) c-TiCrALN. The legend marks the indicated phases. Taken from [94].

oxidation experiment. Also, the positions of the peaks from c-TiCrAlN shift to higher d-spacing due to thermal expansion. With regard to the peak position of the c-TiCrAlN in Figure 32 a) and c), obviously, the d-spacing positions are shifted in different ways. For $Ti_{0.16}Cr_{0.36}Al_{0.48}N$, the c-TiCrAlN peak shifts to higher d-spacing and shifts back, whereas this behaviour is not observed for $Ti_{0.03}Cr_{0.38}Al_{0.59}N$. Additionally, the onset of the decomposition can be extracted from the FWHM of the c-TiCrAlN peak. Here, the FWHM of $Ti_{0.16}Cr_{0.36}Al_{0.48}N$ is described. For the as-deposited coating, the FWHM decreases during annealing at temperatures below 1000 °C. This is an effect of point defect (interstitials and vacancies) annihilation commonly observed during annealing of arc evaporated transition metal nitrides [101] [102]. Above 1000 °C, the FWHM increases for $Ti_{0.16}Cr_{0.36}Al_{0.48}N$ which is attributed to the described process as follows. In Figure 32 a), it is observed that during the first 30 min of isothermal annealing, so after reaching $T_{max,}$ there are a large peak broadening for the c-TiCrAlN (220). They can be interpreted as domains enriched in c-AlN (c-(Ti)CrAlN) and c-TiN (c-TiCr(Al)N) respectively, as seen in Figure 32. After some minutes of isothermal annealing the FWHM decreases and simultaneously pure c-Cr, c-TiN and h-AlN have formed and grown. And after isothermal annealing for 180 min a complete transformation of these decomposition products, c-Cr, c-TiN and h-AlN, has been reached. In the lineouts from the $Ti_{0.03}Cr_{0.38}Al_{0.59}N$ sample in Figure 32 c), no peak broadening corresponding to c-TiN or c-AlN enriched domains are observed. Furthermore, the peak broadening seen for $Ti_{0.16}Cr_{0.36}Al_{0.48}N$ vanishes after 30 min of isothermal annealing and the composition of the remaining cubic phase is close to c-Cr. In this experiment, the decrease of the peak intensities of c-TiCrAlN is associated with the observed decomposition. No oxides are formed.

The first appearance of the h-AlN phase is best seen from the (100) diffraction signal (d ~ 2.7 Å) which is first observed at 1000 °C in $Ti_{0.03}Cr_{0.38}Al_{0.59}N$ in Figure 32 d) and at 1150 °C for $Ti_{0.16}Cr_{0.36}Al_{0.48}N$ in Figure 32 b).

8.2.1 Discussion

The results in this vacuum experiment show directly that there are two different decomposition routes which can be associated with two co-occurring mechanisms of decomposition. In the studies of c-$Ti_xCr_{1-x}Al_{0.61}N$ [20] alloys, the two co-occurring mechanisms of decomposition are the spinodal decomposition of the c-TiCrAlN phase and the direct precipitation of h-AlN from the c-(Ti)CrAlN phase. The spinodal decomposition is the decomposition of one metastable phase into two co-occurring metastable or stable phases. In our case in this *in-situ* annealing experiment, it is the decomposition route of c-TiCrAlN into enriched c-AlN (c-(Ti)CrAlN) and c-TiN (c-TiCr(Al)N). Therefore, in $Ti_{0.16}Cr_{0.36}Al_{0.48}N$, the evolution of the compositional modulated microstructure is consistent with spinodal decomposition.

In contrast, $Ti_{0.03}Cr_{0.38}Al_{0.59}N$ does not display this behaviour. Only nucleation and growth of the h-AlN and two cubic phases, c-TiN and c-CrAlN, appear. Furthermore, the presence of the phases, the decomposition products c-Cr, c-TiN and h-AlN at the end of isothermal annealing, suggests, that a complete decomposition of the c-TiCrAlN phase into its equilibrium phases have occurred. This applies for both compositions. Additionally, for both compositions, the h-AlN phase is expected to precipitate from the c-CrAlN phase [35]. However, the earlier observation of h-AlN (at 1000 °C, see Figure 32 d) in $Ti_{0.03}Cr_{0.38}Al_{0.59}N$ sample indicates that c-CrAlN forms earlier in this sample. In contrast, in $Ti_{0.16}Cr_{0.36}Al_{0.48}N$, there are relatively more stable c-CrAlN domains, where h-AlN precipitates and is surrounded by c-TiCrN domains, compared to $Ti_{0.03}Cr_{0.38}Al_{0.59}N$. The stability is given by a reduced lattice coherency strain with the presence of Cr in TiAlN alloys [49]. In a simple sentence: c-CrAlN domains caused by spinodal decomposition in $Ti_{0.16}Cr_{0.36}Al_{0.48}N$ are more stable (higher thermal stability) compared to the c-CrAlN domains in $Ti_{0.03}Cr_{0.38}Al_{0.59}N$. This is the reason why the formation of h-AlN is suppressed in $Ti_{0.16}Cr_{0.36}Al_{0.48}N$, and this is supported by the fact that the h-AlN appears at 1150 °C, a higher temperature, and not at 1000 °C (as shown for $Ti_{0.03}Cr_{0.38}Al_{0.59}N$). The observed different behaviour of the shift of the peak position of the c-TiCrAlN, *i.e.* the d-spacing, and the trace of FWHM for both compositions also indicates the different decomposition processes. This was described above.

To summarize the observation in the vacuum experiment, at first, there are two different decomposition processes observed in $Ti_{0.16}Cr_{0.36}Al_{0.48}N$ and $Ti_{0.03}Cr_{0.38}Al_{0.59}N$. Secondly, the FWHM behaviour and the shape of the d-spacing for $Ti_{0.16}Cr_{0.36}Al_{0.48}N$ is associated to the spinodal decomposition. Thirdly, c-CrAlN domains, and therefore h-AlN, are surrounded by c-TiN enriched c-TiCr(Al)N domains and c-AlN enriched c-(Ti)CrAlN domains in $Ti_{0.16}Cr_{0.36}Al_{0.48}N$.

We will see in the next section 8.3 that some results of the vacuum annealing experiment are also mirrored in my real-time oxidation experiment.

8.3 *In-situ* oxidation behaviour of TiCrAlN coatings

This chapter starts with the presentation of the time resolved phase evolution of the c-TiCrAlN coating in a real-time oxidation process. The data is extracted by the methodological analysis described in Chapter 6.9. In Figure 33, the time resolved normalized integrated intensity of the a) c-TiCrAlN (111) of $Ti_{0.03}Cr_{0.36}Al_{0.59}N$ and b) c -TiCrAlN (111) of $Ti_{0.16}Cr_{0.36}Al_{0.48}N$ are shown *versus* the isothermal time.

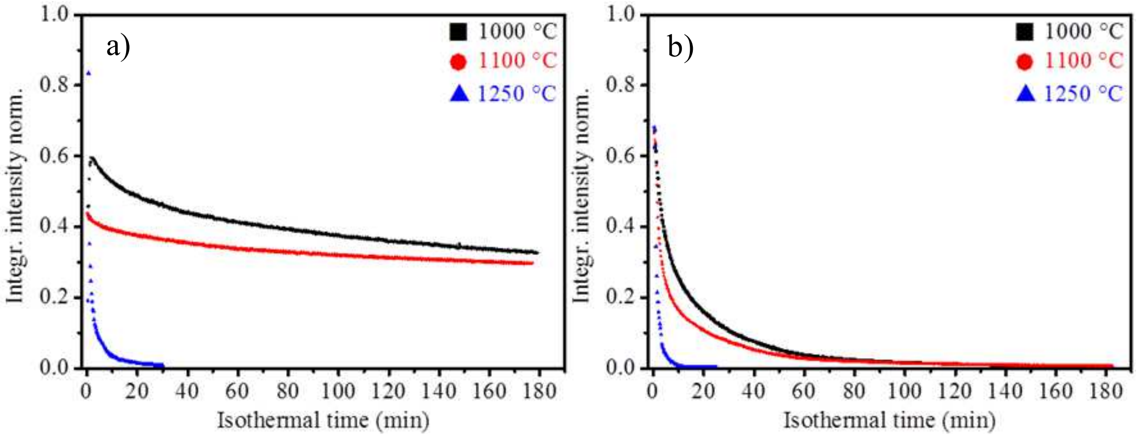

Figure 33: a) Normalized integrated intensity of $Ti_{0.03}Cr_{0.36}Al_{0.59}N$ of the c-TiCrAlN (111) peak for 1000 °C, 1100 °C and 1250 °C and b) the normalized integrated intensity of $Ti_{0.16}Cr_{0.36}Al_{0.48}N$ of the c-TiCrAlN (111) peak for 1000 °C, 1100 °C and 1250 °C **[88]**.

In Figure 33 a), the normalized integrated intensity decreases very slowly after reaching 1000 °C and 1100 °C (at 0 isotherm al time). After ~180 min, the intensity looses about 20 % - 30 %. This illustrated phase evolution supports the fact that the cubic structure of the $Ti_{0.03}Cr_{0.36}Al_{0.59}N$ is still remaining, also at 1100 °C, and the difference is a lower intensity compared to the intensity at 1000 °C. For 1250 °C, the intensity decreases within 30 min indicating a total oxidation of the cubic structure as observed in the lineouts in Figure 31. In Figure 33 b), for 1000 °C and 1100 °C the peak intensity of the c-TiCrAlN (111) vanishes within ~180 min indicating a total oxidation of the coating. For 1250 °C, the peak intensity vanishes within 10 min indicating a faster oxidation of the coating.

8.3.1 Microstructural analysis

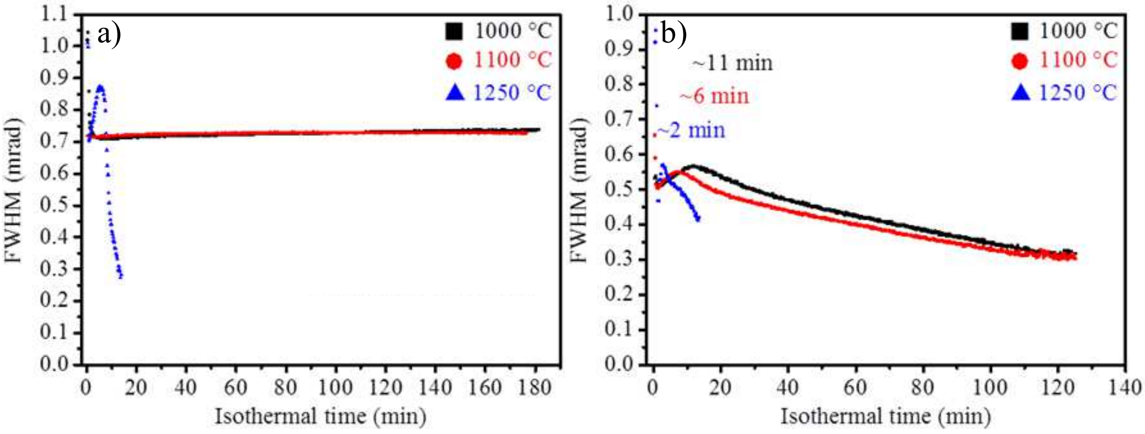

Figure 34: FWHM as a function of isothermal time of a) $Ti_{0.03}Cr_{0.38}Al_{0.59}N$ c-TiCrAlN (111) and b) $Ti_{0.16}Cr_{0.36}Al_{0.48}N$ c-TiCrAlN (111).

The FWHM values of the c-TiCrAlN (111) coating are seen in Figure 34 for a) $Ti_{0.03}Cr_{0.38}Al_{0.59}N$ and b) $Ti_{0.16}Cr_{0.36}Al_{0.48}N$. The instrumental broadening (0.21 mrad) of the peaks are included. The FWHM for the as-deposited state for both coatings is ~1 mrad. In Figure 34 b), the FHWM shapes can be described as follows. In the beginning of the annealing process the FWHM drops down within 1 min for all indicated temperatures. An effect of point defect annihilation, which was also commonly observed during annealing of arc evaporated transition metal nitrides [94] [101] [102], can appear here. This effect is mirrored in an increase of the integrated intensity of the measured c-TiCrAlN peaks in both compositions which can be indicated as a re-orientation and grain growth. The peak broadening is inversely related to domain size, as described in Chapter 6 and implied by the Scherrer equation, so the decrease in FWHM with isothermal time and temperature is related to an increase of the domain size and decrease of micro-strain, whereas a peak broadening indicates a reduction in grain size or an increase of microstress [93]. In Figure 34 b), after reaching the local minimum of the FWHM shape, the broadening increases within ~11 min (~0.58 mrad), ~6 min(~0.55 mrad), or ~2 min(~0.58 mrad) depending on the temperature. This can be attributed to the onset of a decomposition process which was also observed in the vacuum annealing experiment in section 8.2. After reaching the local maximum in the peak broadening, the FWHM slowly decreases. The different values between the local maximum and the end of annealing time are not large. In Figure 34 a), the FWHM of $Ti_{0.03}Cr_{0.38}Al_{0.59}N$ does not show this behaviour compared to the composition $Ti_{0.16}Cr_{0.36}Al_{0.48}N$. Here, there is a decrease in the FWHM within the first 1 min, an increase of the FWHM is not observed. A plateau value is reached (~0.74 mrad). But for 1250 °C, a decrease and an increase of the FWHM can be measured within 10 min. By comparing the FWHM of both samples, $Ti_{0.03}Cr_{0.38}Al_{0.59}N$ shows a smaller domain size, or higher microstrain.

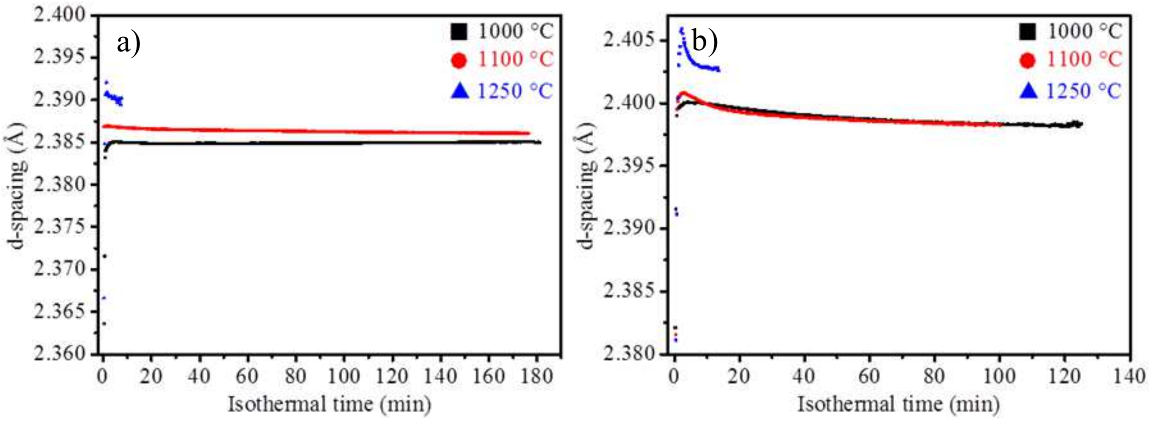

Figure 35: d-spacing of a) $Ti_{0.03}Cr_{0.38}Al_{0.59}$ (111) and b) $Ti_{0.16}Cr_{0.36}Al_{0.48}N$ (111) as a function of isothermal time.

Figure 35 shows the shift in d-spacing of the c-TiCrAlN (111) for a) $Ti_{0.03}Cr_{0.38}Al_{0.59}N$ and b) $Ti_{0.16}Cr_{0.36}Al_{0.48}N$ for the indicated temperatures. For all temperatures, d-spacing increases within 1 min which can be attributed to the thermal expansion. In Figure 35 a), for 1000 °C and 1100 °C the d-spacing increases within 1 min and shows a plateau after reaching its maximum value. For high temperatures, the d-spacing is shifted to higher values. For 1250 °C, only the first 10 min could be analysed due to the vanished c-TiCrAlN peak. In Figure 35 b), after 1 min the d-spacing further increases and shows a "peak". For 1000 °C, a low increase can be seen. After that, the d-spacing slowly decreases followed by a plateau. The reason why the d-spacing shows nearly the same values at 1000 °C and 1100 °C after 60 min could be due to the decreased resolution of c-TiAlN (111) peak caused by the strong oxidation of the cubic structure. For 1100 °C and 1250 °C, the increase is more pronounced. This peak can be attributed to the early stage of the decomposition process as surmised in the FWHM in Figure 34 at the same time scale.

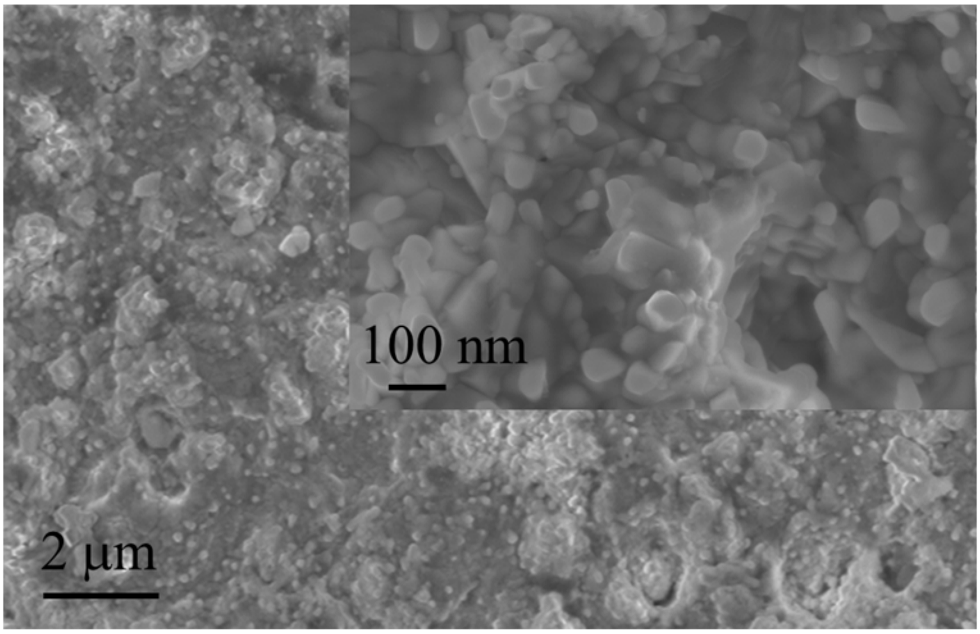

Figure 36: SEM of grains of $Ti_{0.03}Cr_{0.38}Al_{0.59}N$ coating surface after 1 min annealing at 1250 °C

In Figure 36 grains of the $Ti_{0.03}Cr_{0.38}Al_{0.59}N$ coatings are illustrated. The measured grain size is about 55-100 nm at 1250 °C after 1 min isothermal annealing based on the SEM. Based on the *in-situ* SR-XRPD the estimated mean grain size is 57-92 nm thus lying in the same range. The oxidation process of the SR-XRPD measurements is shown in Figure 37. Here, the 2D patterns from a) to c) show that no texture will form during the isothermal time of ~180 min at 1100 °C. On the right side of each pattern is the colored intensity scale. In the middle of the pattern the beam stop is located and around the beam stop a broad ring appears. This can be identified as a halo caused from the scattering of the quartz tube of the experimental setup by the synchrotron radiation.

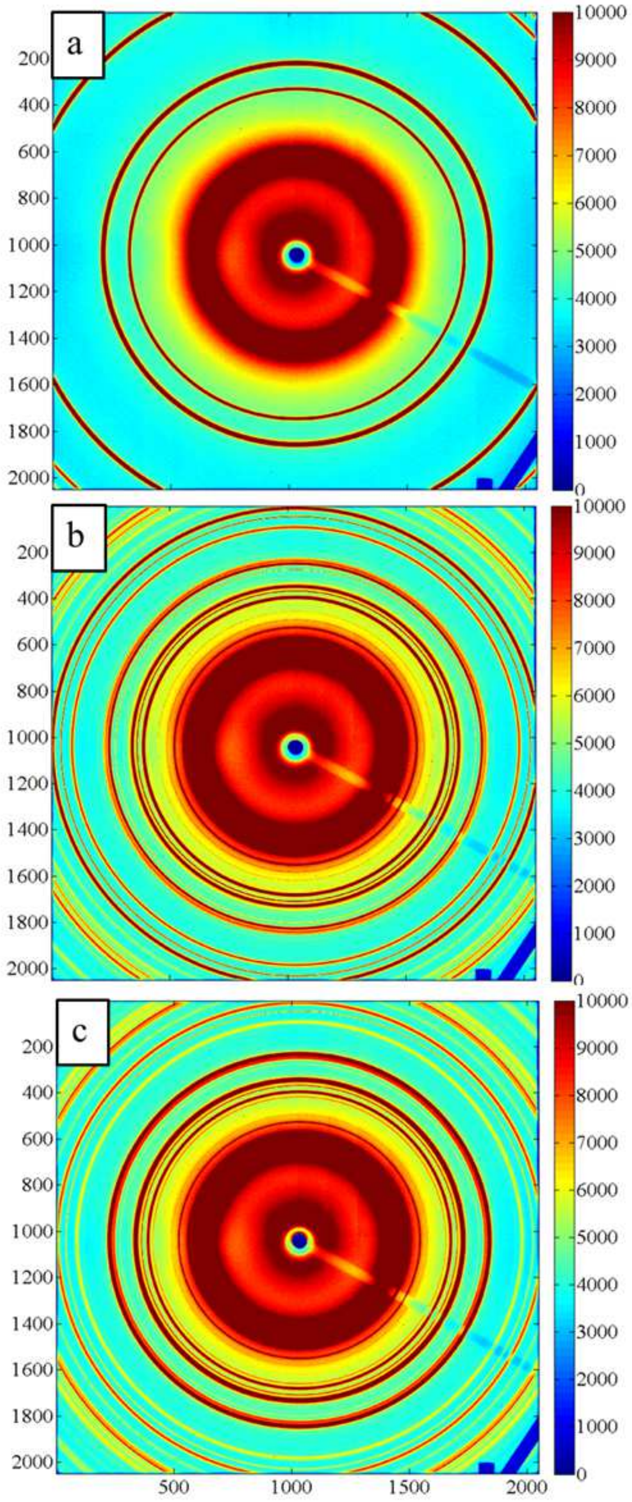

Figure 37: 2D diffraction pattern of the annealing process of $Ti_{0.16}Cr_{0.36}Al_{0.48}N$ at 1100 °C. a) as-deposited coating, b) early stage of the oxidation process after 13 min and c) last 2D diffraction pattern after 180 min.

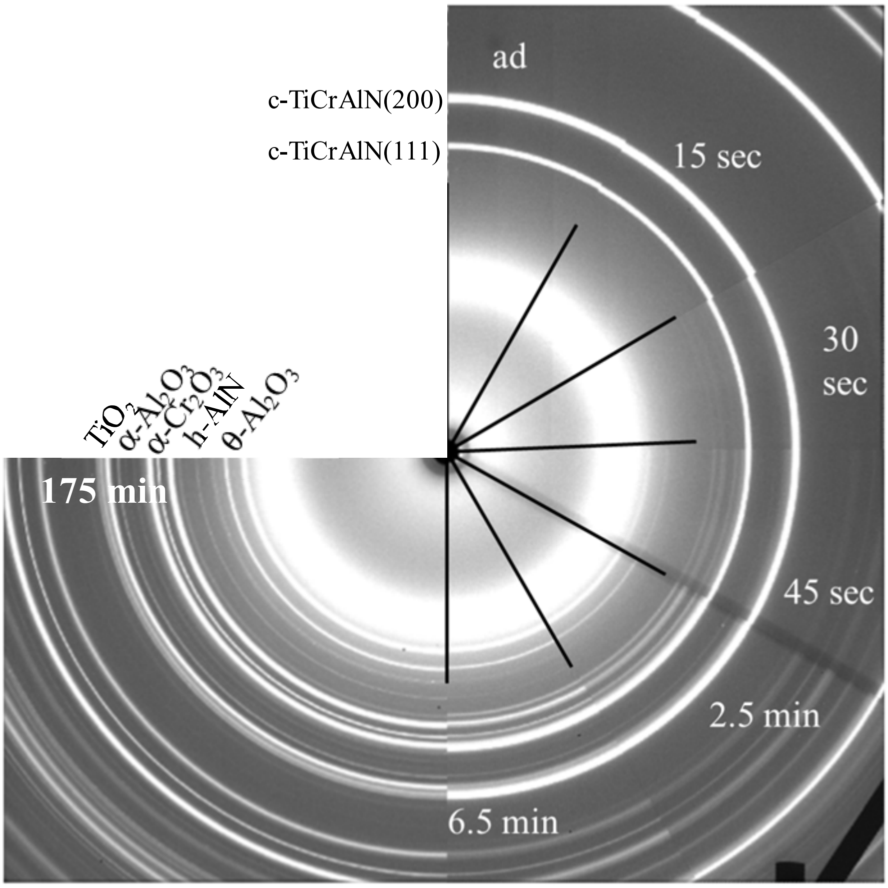

Figure 38: 2-D diffraction pattern of $Ti_{0.16}Cr_{0.36}Al_{0.48}N$ powder sample at 1100°C measured with the synchrotron radiation energy of 53.7 keV. Clockwise the indicated time steps of the isothermal time during the oxidation process. For a detailed view of the oxides, see Figure 29.

In Figure 38, a 2-D diffraction pattern is shown of the oxidation process of the $Ti_{0.16}Cr_{0.36}Al_{0.48}N$ powder sample at 1100 °C. The illustration is subdivided into 7 sections to reveal an overview of the oxidation process. Each section represents a defined time step of the annealing process of the oxidation experiment. On the right side the isothermal time from the as-deposited state (ad) until 6.5 min is illustrated and on the left side the last pattern of the annealing oxidation experiment is shown.

The ad section represents the beginning of the annealing. The c-TiCrAlN phases are easily seen. The inner Deby-Scherrer ring is the (111) and the outer one the (200). The short one at the edge is the (220). At 15 sec a small shift to the inner direction of the Debye-Scherrer rings of the c-TiCrAlN coating can be seen which is stronger at 30 sec. This is caused by the fast thermal expansion which results in a decreasing of the

2θ angle respectively increasing of the d-spacing and was also shown in Figure 35. At this time, new Debye-Scherrer rings with low intensity appear. This marks the beginning of the oxidation process. These diffraction rings become stronger with longer isothermal time. In this diffraction pattern, it seems that the intensity and the width of c-TiCrAlN become stronger and broader within 6.5 min. But in this case, there is an overlap of 4 phases of the coating, some oxides and h-AlN. After ~3 hours, the coating is totally oxidized. A strong contrast between the onset of the oxidation process and the end can be easily seen at the edge between 6.5 min and ~180 min for the c-TiCrAlN.

8.3.2 Discussion

With the methodological approach, as described in Chapter 6.9, it is possible to analyze the real-time oxidation process. The method enabled to analyze the heavily oxidized and partially overlapped c-TiCrAlN peak (overlapped with α-Al_2O_3 and α-Cr_2O_3) with an additionally strong peak position shift.

By comparing these two results, *i.e.* the evolution of the integrated intensity *versus* the isothermal time in Figure 33, it is obvious that the coating with less Ti-content and high Al-content shows a much better oxidation resistance than the coating with higher Ti-content and lower Al-content. $Ti_{0.03}Cr_{0.38}Al_{0.59}N$ shows an outstanding oxidation behaviour up to 1250 °C and confirms the rough observation from the lineouts at 1000 °C in section 8.1. The relevant cubic phases are clearly detectable after 180 min for Ti 3 at. % at 1000 °C and 1100 °C compared to the coating for Ti 16 at. % respectively. At 1250 °C, a total oxidation of the coating for $Ti_{0.03}Cr_{0.38}Al_{0.59}N$ is measured within 30 min, whereas for $Ti_{0.16}Cr_{0.36}Al_{0.48}N$ a total oxidation is measured within 10 min. The oxidation resistance of $Ti_{0.03}Cr_{0.38}Al_{0.59}N$ shows an improvement of 300 % up to 1250 °C, based on this timescale and on this temperature.

In the real-time annealing oxidation process, the c-TiCrAlN phase expands in the early stage of the decomposition process. This is mirrored in the d-spacing behaviour, the measured “peak”, and additionally, the thermal expansion, which was also observed in our *in-situ* vacuum annealing experiment for $Ti_{0.16}Cr_{0.36}Al_{0.48}N$ in [94], as the shift of the peak position in Figure 32 in section 8.2. This additional increase in the d-spacing shift cannot be seen in Figure 35 for $Ti_{0.03}Cr_{0.38}Al_{0.59}N$. Here in $Ti_{0.03}Cr_{0.38}Al_{0.59}N$, obviously, the observed effect is only thermal expansion in this coating.

An explanation for the stronger peak-shift, in $Ti_{0.16}Cr_{0.36}Al_{0.48}N$, could be the appearance of strained crystallites in the early stage of the decomposition process [73] [89], which were also observed in *in-situ* annealing experiments of TiAlN. A volume expansion of surrounded domains associated with a phase transformation, therefore in my oxidation experiment the transformation of c-TiCrAlN into convoluted oxides, into the domains (observed and described in section 8.2), and the h-AlN phase, can be also possible. Similar phenomena were also observed in annealed TiAlN for the cubic to hexagonal transformation [89]. The following decrease of the d-spacing shift corresponds to the onset of the forming and growth of the decomposition products, but the decomposition products themselves cannot be measured in my real-time oxidation experiment due to the oxidation effect on this sample.

The increase of the FWHM after reaching the according temperature indicates a phase separation into c-AlN and CrN components by spinodal decomposition, according to *ex-situ* annealing experiments of other authors [103] [104] [105] [106] [107], or in our case into enriched c-AlN (c-(Ti)CrAlN) and c-TiN (c-TiCr(Al)N) domains (see section 8.2). The following decrease can be related to the oxidation process and the observed forming of domains mentioned in Chapter 8.2. Nevertheless, the measured time resolved full shape of the FWHM in this quaternary compositional TiCrAlN system under oxidation atmosphere was not measured and reported in the literature yet. Based on other systems, binary or ternary systems closed to the TiCrAlN system, only parts of the FWHM progression can be found in the literature. Furthermore, the annealing time varies in the literature which makes an interpretation more difficult.

As we know from the literature [20] [48] (see also Chapter 2.3), the elements in the c-TiCrAlN in the annealing process segregated forming a structure containing h-AlN and c-(Ti)CrAlN domains located in the grain boundaries, and the grains are decomposed into coherent TiCr- and Al-rich c-TiCrAlN domains [20] [48]. This processes are observed in the quaternary TiCrAlN system in a vacuum environment [20] [48], and a similar process appears in our report as discussed in 8.2.1. Therefore, it is concluded that two co-occurring decomposition mechanisms [20] can happen, dependent on the Ti-content. One mechanism describes the spinodal decomposition as a dominating mechanism [20], with higher Ti-content, and the other one is the precipitation and growth of h-AlN domains at the grain boundaries [20], which was observed in CrAlN [100]. These two co-occurring decomposition mechanisms are responsible for higher hardness in TiCrAlN with high Ti-content compared to less Ti-content.

The behaviour of d-spacing shift and the behaviour of the FWHM in my real-time oxidation experiment for $Ti_{0.16}Cr_{0.36}Al_{0.48}N$ show a similar trend, as the described FWHM and d-spacing shift in our *in-situ* vacuum annealing experiment for $Ti_{0.16}Cr_{0.36}Al_{0.48}N$ in section 8.2. Both behaviours, the d-spacing shift and the trend of the FWHM, are associated with the spinodal decomposition. Therefore, I assume that the decomposition mechanisms, observed in our vacuum experiment [94], also appear in the real-time oxidation process, but it is overlapped with the additional effect of the oxidation process. And additionally, my assumption is that the spinodal decomposition has negative effect on $Ti_{0.16}Cr_{0.36}Al_{0.48}N$ in air, *i.e.* the stronger oxidation of the cubic structure as shown in Figure 33.

However, in my *in-situ* oxidation experiment obviously the formed oxide scales α-$(Cr,Al)_2O_3$, in $Ti_{0.03}Cr_{0.38}Al_{0.59}N$, provide a nearly protective effect against a complete decomposition into the decomposition products (see section 8.2) of the metastable c-TiCrAlN phase. The protective effect against a complete decomposition is better in $Ti_{0.03}Cr_{0.38}Al_{0.59}N$ compared to $Ti_{0.16}Cr_{0.36}Al_{0.48}N$. The evidence for this statement is supported by the fact that the described behaviours of the FWHM and d-spacing shift only appear in $Ti_{0.16}Cr_{0.36}Al_{0.48}N$, but in both experimental setups in vacuum and in air. Therefore obviously, the formed oxide scale, composed of α-$(Cr,Al)_2O_3$ and TiO_2, in $Ti_{0.16}Cr_{0.36}Al_{0.48}N$ provides a less protective effect against the spinodal decomposition in my real-time oxidation experiment.

From the peak evolution of the c-TiCrAlN in the vacuum experiment (see Figure 32), a strong decrease of the peak intensity (c-TiCrAlN) can be seen directly in both lineouts (the *in-situ* evolution of intensity *vs.* isothermal time is not shown).

By comparing the intensity of the annealed $Ti_{0.03}Cr_{0.38}Al_{0.59}N$ in vacuum with the intensity of the annealed $Ti_{0.03}Cr_{0.38}Al_{0.59}N$ in air, the cubic structure is still remaining after 180 min in the real-time oxidation experiment and only a low decrease of the peak intensity is observed. This low decrease of the integrated intensity is therefore connected with the simultaneous growth of oxides and the growth of h-AlN. This is not the case for $Ti_{0.16}Cr_{0.36}Al_{0.48}N$. Here, no cubic structure is remaining due to the oxidation process. Nevertheless, in both compositions a complete decomposition is prevented or at least is nearly hindered, as we will see in section 8.6.

It was not possible to see directly the decomposition product and decomposition parts from the XRD-pattern of the c-TiCrAlN, *i.e.* the broadening of FWHM (the interpreted c-AlN (c-(Ti)CrAlN) and c-TiN (c-TiCr(Al)N), the c-Cr and the c-TiN, due to the oxidation effect. Additionally, it seems that the c-(Ti)CrAlN domains, in $Ti_{0.16}Cr_{0.36}Al_{0.48}N$, caused by the spinodal decomposition in our c-TiCrAlN material system, as described in 8.2.1, are not stable under the oxidation aspect, whereas theses domains are stable under vacuum environment [94]. The decomposition of the c-(Ti)CrAlN domains into coherent TiCr- and Al-rich c-TiCrAlN domains, as mentioned above, can be responsible for the worse oxidation resistance. As we know from section 8.1.1, Ti rich coatings like TiAlN, can form porous TiO_2, which shows a negative effect on the oxidation resistance. Therefore, Ti- enriched domains located at the grain boundaries can show a similar effect. This benefits further oxidation and growth of oxides, as we will see in section 8.4.

Another situation appears for $Ti_{0.03}Cr_{0.38}Al_{0.59}N$. In our vacuum annealing experiment only nucleation and growth of CrAlN appear [94]. But we know from the literature (see Chapter 2.2) that annealed CrAlN in air can form a dense mixture structure of Al_2O_3 and Cr_2O_3. Obviously, further diffusion of oxygen into the grains is prevented, thus also nearly preventing the complete decomposition of c-CrAlN, which, thus, raises the oxidation resistance temperature. A similar phenomenon was also observed by *ex-situ* oxidation experiment of CrAlN by Reiter *et. al.* [37]. Here, the assumption was that the complete decomposition of the c-CrAlN (decomposition products are h-AlN, CrN and Cr) are prevented by the Cr_2O_3-Al_2O_3 oxide scale. From my real-time oxidation experiment I propose the same assumption, however, for c-TiCrAlN material system.

The sample $Ti_{0.03}Cr_{0.38}Al_{0.59}N$ shows an excellent oxidation resistance and can be a candidate for high end industrial applications under extreme conditions. One has to consider, that a powder sample shows much more surface area. The powder sample compared to a bulk material or coating surface has a major surface target area for incoming oxides. So, it can be concluded that this compositions $Ti_{0.03}Cr_{0.38}Al_{0.59}N$ will also show an impressive oxidation resistance as a coating for cutting tools.

8.4 Oxidation – *in-situ* growth of oxides

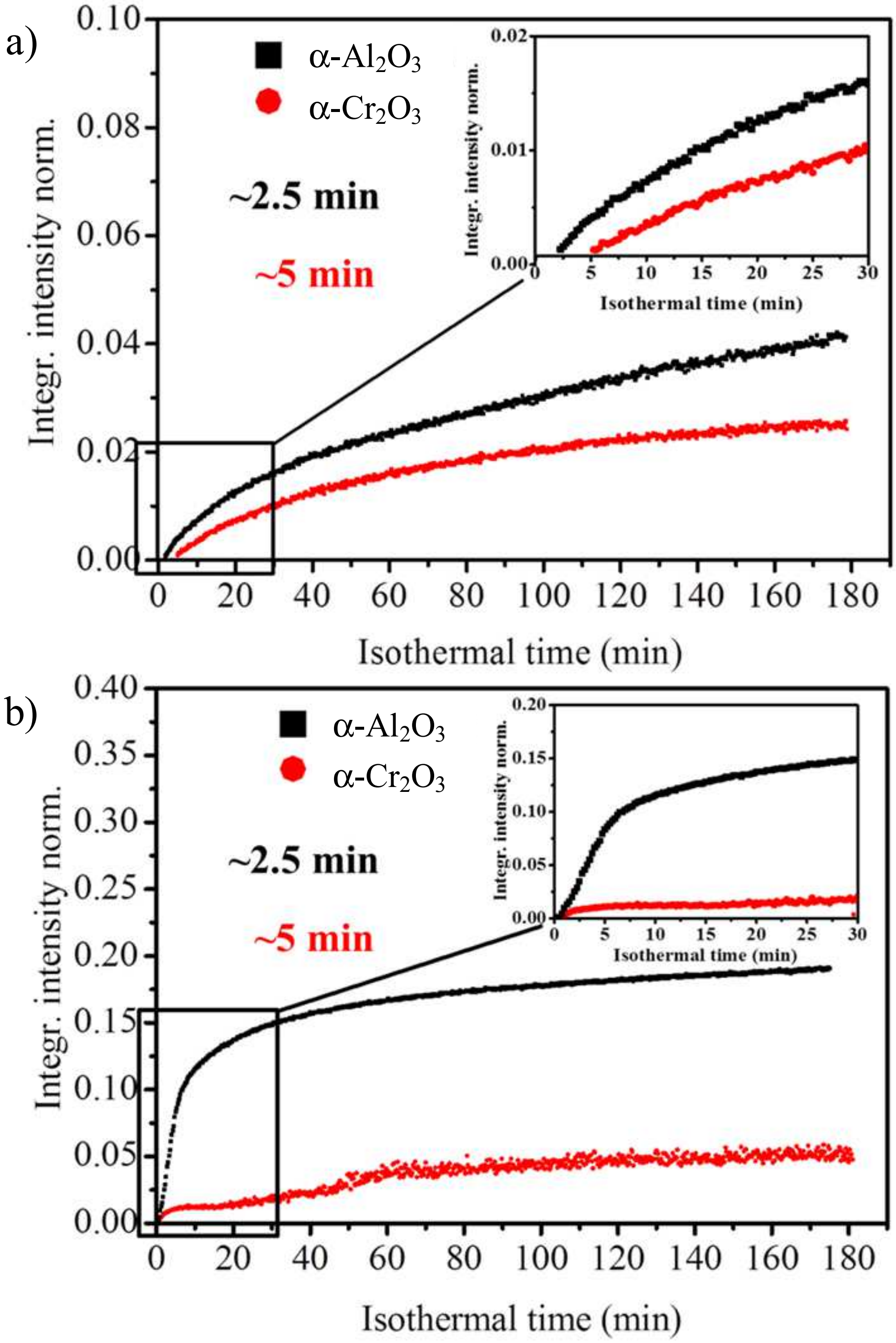

Figure 39: Normalized integrated intensity as a function of isothermal time of (black) α-Al_2O_3(104) and (red) α-Cr_2O_3(104) of a) $Ti_{0.03}Cr_{0.38}Al_{0.59}N$ and b) $Ti_{0.16}Cr_{0.36}Al_{0.48}N$ at 1000 °C. The inset in right upper corner shows a magnification of the square frame in the left bottom corner.

Figure 39 a) and b) show the time resolved normalized integrated intensity as a function of isothermal time of the new emerging convoluted oxide phases α-Al_2O_3(104)(black) and α-Cr_2O_3(104)(red) separately at d = 2.62 Å and d = 2.60 Å (from Figure 29) at 1000 °C of both compositions. In Figure 39 a), it can be clearly seen, that the onset of the emerging phases are not at the same time for the composition with low Ti-content and high Al-content, $Ti_{0.03}Cr_{0.38}Al_{0.59}N$. The α-Al_2O_3 starts to grow after ~2.5 min, as indicated in Figure 39 a), after reaching 1000 °C. The growth of the α-Cr_2O_3 is delayed by additional 2.5 min, the onset starts at ~5 min, as indicated in Figure 39 a). The inset shows a magnification of the first 30 min of the time resolved evolution of the described oxide phases. After 10 min both phases grow with the same rate and after 80 minutes it seems that α-Al_2O_3 constantly grows whereas the α-Cr_2O_3 growth slows down with time. The α-Al_2O_3 (black) is still growing after 180 min whereas α-Cr_2O_3 shows a trend to reach a saturated value. The value is 0.025 after 180 min, respectively 0.04.

Figure 39 b) shows the same oxide phases as in Figure 39 a) but for $Ti_{0.16}Cr_{0.36}Al_{0.48}N$, high Ti-content an low Al-content. Both phases start to grow together and do not show any time delay. After ~5 min the α-Cr_2O_3 seems to reach a saturated value of 0.02, it holds this value for 20 min, and after 20 min the phase slowly grows to the normalized integrated intensity value 0.05 after 180 min. It reaches a saturated value 0.05 after 60 min. The value is 2 times higher in comparison to the $Ti_{0.03}Cr_{0.38}Al_{0.59}N$ coating. In summary, the normalized integrated intensity value 0.02 for α-Cr_2O_3 is reached after ~5 min in $Ti_{0.16}Cr_{0.36}Al_{0.48}N$, whereas the value 0.02 for α-Cr_2O_3 in $Ti_{0.03}Cr_{0.38}Al_{0.59}N$ is reached after ~100 min.

In Figure 39 b), the α-Al_2O_3 (black) phase rapidly grows within 10 min and slows down with time. After 180 min a normalized integrated intensity value 0.18 is reached. In Figure 39 a), $Ti_{0.03}Cr_{0.38}Al_{0.59}N$, the normalized integrated intensity value 0.04 is reached after 180 min. The composition $Ti_{0.03}Cr_{0.38}Al_{0.59}N$ with low Ti-content and high Al-content shows a much lower normalized integrated intensity value (0.04) of the α-Al_2O_3 than the composition $Ti_{0.16}Cr_{0.36}Al_{0.48}N$ with high Ti-content and low Al-content (0.18).

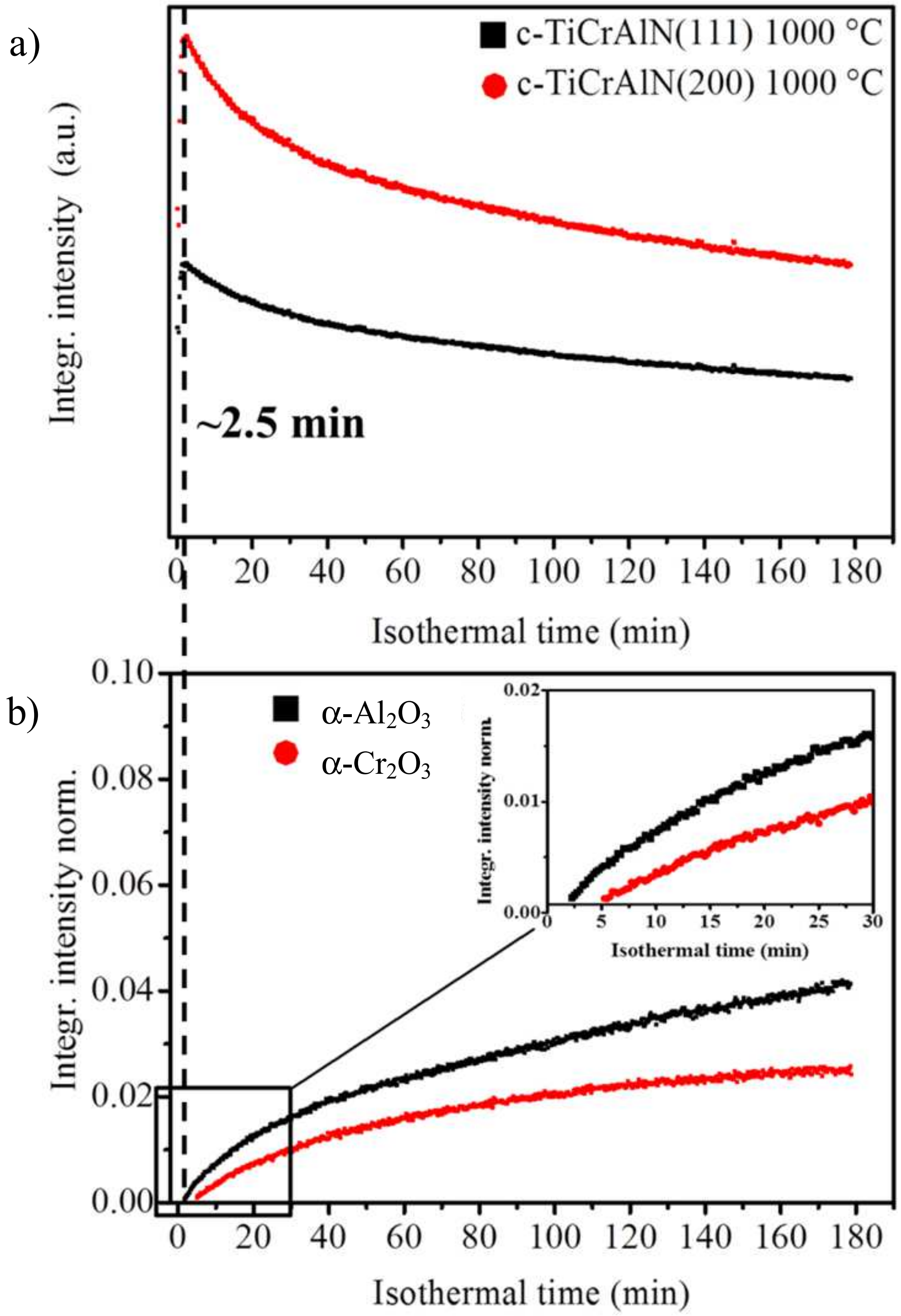

Figure 40: a) Integrated intensity of the c-TiCrAlN (111) and (220) as a function of isothermal time at 1000 °C of $Ti_{0.03}Cr_{0.38}Al_{0.59}N$. b) see Figure 39 a). The vertical black dashed line marks the onset of the oxidation of the coating and the transformation of the oxides (black) α-Al_2O_3(104) and (red) α-Cr_2O_3(104). ~2.5 min (black for α-Al_2O_3) and ~5 min (red for α-Cr_2O_3) mark the start time of the transformation.

Figure 40 a) illustrates the integrated intensity as a function of isothermal time of the c-TiCrAlN (111) and (200) of $Ti_{0.03}Cr_{0.38}Al_{0.59}N$, and Figure 40 b) illustrates the transformation of the emerging oxides. The onset of the decrease of the intensity in Figure 40 a) and the beginning of the growth of oxides in Figure 40 b) are marked with the dashed black line. Additionally, the intensity of c-TiCrAlN (111) increases within the first ~2.5 min after reaching 1000 °C. This corresponds to the same observed time delay before the onset of the emerging oxides from the lineouts in Figure 29. The increase indicates likely a strong reorientation of the crystallites in the indicated lattice planes. In comparison to $Ti_{0.03}Cr_{0.38}Al_{0.59}N$, the increase of the intensity of coating peaks is also observed for $Ti_{0.16}Cr_{0.36}Al_{0.48}N$, but within the ramping time to T_{max} 1000 °C. After reaching T_{max}, the peak intensity of $Ti_{0.16}Cr_{0.36}Al_{0.48}N$ decreases immediately and does not show a continued increase as shown in Figure 40a).

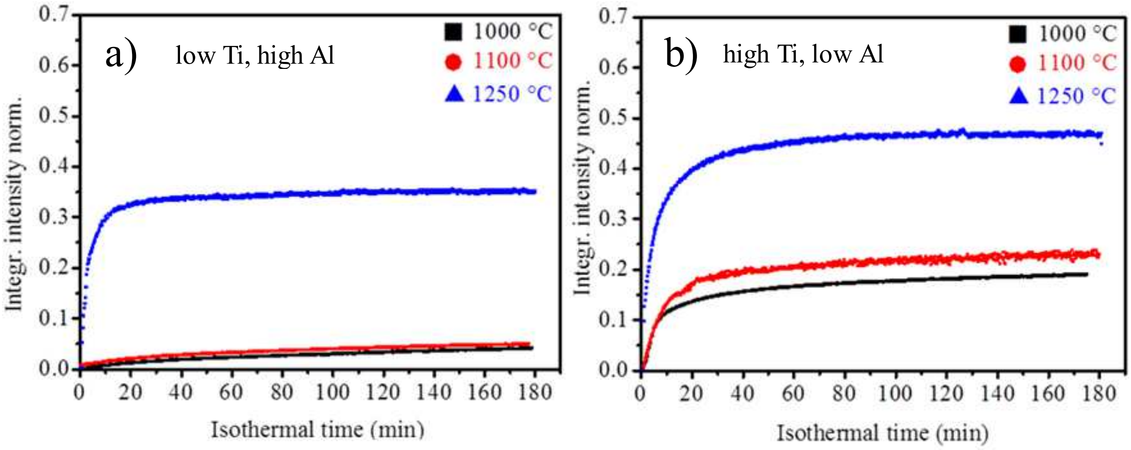

Figure 41: The normalized integrated intensity of the Al_2O_3 at d = 2.60 Å as a function of isothermal time for 1000 °C, 1100 °C and 1250 °C of a) $Ti_{0.03}Cr_{0.38}Al_{0.59}N$ and b) $Ti_{0.16}Cr_{0.36}Al_{0.48}$

Figure 41 illustrates the normalized integrated intensity *versus* isothermal time of α-Al_2O_3 for a) $Ti_{0.03}Cr_{0.38}Al_{0.59}N$ and b) $Ti_{0.16}Cr_{0.36}Al_{0.48}N$ for 1000 °C, 1100 °C and 1250 °C. In Figure 41 a), the normalized integrated intensity for 1000 °C and 1100 °C shows small differences in the time evolution of the emerging oxide phase. The normalized integrated intensity values after 180 min are 0.04 for 1000 °C and 0.05 for 1100 °C and no plateau of normalized integrated intensity can be observed after

180 min. At 1250 °C, the integrated intensity rapidly grows within 10 min in the beginning of the transformation and saturates within additional 10 min. The normalized integrated intensity value for 1250 °C is 7 times higher than the normalized integrated intensity value for 1000 °C, respectively 1100 °C. The plateau can be indicated as a full transformation of the α-Al_2O_3 oxide or at least as part of a full transformation of the coating into an oxide. This fact is strongly supported by Figure 33 a) and b). The drastic decrease of the c-TiCrAlN (200) can be clearly seen for 1250 °C within 30 min

Figure 41 b) shows a similar scenario. For 1000 °C and 1100 °C the transformation rapidly grows and slows down with time. After 180 min the normalized integrated intensity values are 0.18 for 1000 °C and 0.22 for 1100 °C and the difference between these temperatures are slightly higher compared to Figure 41 a) $Ti_{0.03}Cr_{0.38}Al_{0.59}N$. Compared to the $Ti_{0.03}Cr_{0.38}Al_{0.59}N$ coating, the values are 4-5 times higher.

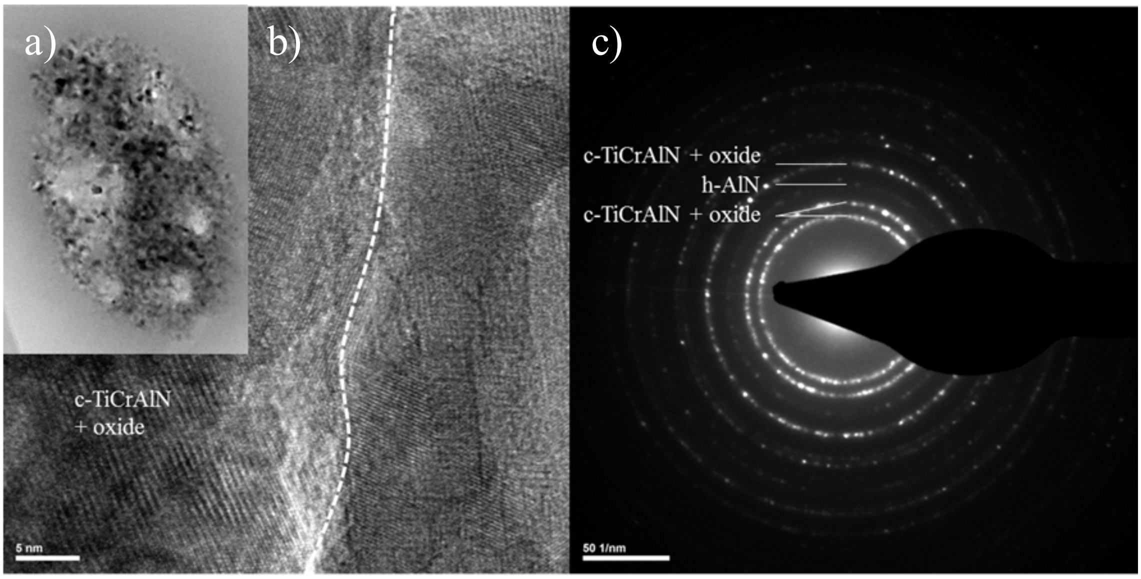

Figure 42: a) STEM micrograph showing a $Ti_{0.03}Cr_{0.38}Al_{0.59}N$ powder particle after 5 min annealing at 1250 °C in Air. b) HRTEM micrograph showing overlapped domains of oxides and c-TiCrAlN domains. The dashed line marks a grain boundary. c) SAED pattern from the area of the powder particle in b).

For 1250 °C the normalized integrated intensity values is 0.48 after 180 min and a plateau can be observed.

In Figure 42, a STEM pattern of a contaminated powder particle of $Ti_{0.03}Cr_{0.38}Al_{0.59}N$ is illustrated. Figure 42 a) illustrates the powder particle, Figure 42 b) presents a HRTEM micrograph of a part of the particle in a) and Figure 42 c) presents a SAED of an area of b). Unfortunately, the shown domains are strongly overlapped with oxides and a definite conclusion cannot be drawn. Nevertheless, the selected SAED was close to the grain boundaries. From c), a precipitation of h-AlN and oxides along the grain boundaries can be surmised. This can be used as an explanation for the h-AlN behaviour in 8.6.

8.4.1 Discussion

According to the structure factors, I study the α-Al_2O_3(104) peak, see Figure 29, with the highest intensity for a better signal to noise ratio. The sample with higher Al-content shows a lower integrated intensity of α-Al_2O_3, whereas the sample with lower Al-content shows a higher integrated intensity of α-Al_2O_3. All α-Al_2O_3 peaks show this behaviour. These effects were also observed in the XRD-pattern of TiCrAlN in [85] or [20]. The different peak intensities in the compositions with different Ti-content and Al-content can be related to the thermal stability, and therefore the observed different decomposition mechanism, and the observed oxidation resistance of the TiCrAlN powder samples. The enhanced oxidation resistance for the low Ti-content in $Ti_{0.03}Cr_{0.38}Al_{0.59}N$ is related to the formation of the observed dense convoluted $(Cr,Al)_2O_3$ peak.

Zhou *et al.* have assumed in their report that the higher oxidation resistance of TiCrAlN is likely related to the formation of dense protective oxide layers consisting of α-Cr_2O_3 and Al_2O_3, which supress the further diffusion and penetration of oxygen inside the coatings. Furthermore, the promotion of α-Al_2O_3 has been suggested to be a reason for the improved oxidation resistance [7] [93] [108]. Comparing the evolution of integrated intensity of the c-TiCrAlN of $Ti_{0.16}Cr_{0.36}Al_{0.48}N$ (Figure 33) with the growth of the α-Al_2O_3 of $Ti_{0.16}Cr_{0.36}Al_{0.48}N$ (Figure 41) I can confirm this assumption with my applied peak fitting modelling of the oxidized coating structure and convoluted oxide growth. By summing the integrated intensity of the oxidized c-TiCrAlN (decreased intensity) with the integrated intensity of oxide growth (increased intensity), I nearly get a simple horizontal line (not shown). A plateau of the integrated intensity of α-Al_2O_3 means, in combination with a vanished cubic structure, a complete transformation of the oxidized coating into an oxide.

The decreased oxidation resistance of higher Ti-content in $Ti_{0.16}Cr_{0.36}Al_{0.48}N$ can be attributed to the formation of porous TiO_2 phase in the oxide scale, which was discussed in section 8.1.1. The TiO_2 phase shows a negative effect on the oxidation resistance. As a consequence, the attack of oxygen and the outward diffusion of nitrogen and aluminum/chromium became more significant for higher Ti-content and lower Al-content. This leads to a fast degradation of the c-AlN phases, or here of c- (Ti)CrAlN, in the powder sample and the formation of α-Al_2O_3 and h-AlN.

The outstanding oxidation resistance of $Ti_{0.03}Cr_{0.38}Al_{0.59}N$ can be explained by a slowed down inward attack of oxygen and outward diffusion of Al. This is also seen from the time resolved evolution of the convoluted $(Cr,Al)_2O_3$, the slow growth of the oxides. In this case, there may have been a small amount of Al and Cr in the dense convoluted $(Cr,Al)_2O_3$ scale, but most Al of $Ti_{0.03}Cr_{0.38}Al_{0.59}N$ should remain in the cubic lattice and bond with Cr and N, and be transformed into h-AlN. It is suggested [36] [26] that the adding of Al to CrN is related to an altered bond structure with stronger Al-N bonds, which can suppress nitrogen release and stabilize the cubic structure [20]. The high Al-content in the $Ti_{0.03}Cr_{0.38}Al_{0.59}N$ coating supports this explanation above. This stabilized cubic structure of $Ti_{0.03}Cr_{0.38}Al_{0.59}N$ in the real-time oxidation experiment was also analysed in section 8.3 before. Therefore, this suggestion can be supported.

Furthermore, Zhu *et al.* reported in their *ex-situ* oxidation experiment of CrAlN that α-Al_2O_3 and α-Cr_2O_3 formed simultaneously [109], which, according to my *in-situ* synchrotron data, is here not the case for TiCrAlN with low Ti-content.

Likely due to the higher Al-content and due to the higher affinity of Al to oxidize compared to that of Cr [109], which is seen from my synchrotron radiation data, the inward diffusion of oxygen atoms leads to emerging α-Al_2O_3 phase at first. Due to a low penetrability of oxygen atoms in α-Al_2O_3 [90] [110], the α-Cr_2O_3 forms very slowly and also only a small amount is formed. However, the fact that the h-AlN forms at first and after ~2.5 min α-Al_2O_3 starts to form means that the c-CrAlN domains forms earlier, which was also observed in our *in-situ* annealing vacuum experiment.

8.5 Kinetic analysis

As oxidation is a thermally activated reaction, oxidation rates follow Arrhenius law where the kinetic constant increases with temperature.

In material science phase transitions are one of the most important topics. The crystallization process and other solid state transformations of materials usually involve nucleation and growth. These transformations are described by Kolmogorov-Johnson-Mehl-Avrami KJMA model. This is a most frequently used method, *e.g.*, for oxidation in Al powders [111] and transformation in ceramic coatings [112]. To extract kinetic information of phase transformation and growth kinetics from the experimental synchrotron radiation data this Kolmogorov-Johnson-Mehl-Avrami KJMA equation [113] [114] [115] [116] is used. The equation in its differential form Eq. (6) and after integration Eq. (7) is:

$$\mathbf{df = (1 - f)dx} \tag{6}$$

$$\mathbf{f = 1 - e^{-x}} \tag{7}$$

f is the transformed fraction and x an Arrhenius expression. *f* is obtained by normalizing the integrated intensity (*e.g.* from Figure 23) values with the maximum transformed values.

For the given isothermal conditions x is given by Eq. (8) and Eq. (9):

$$\mathbf{x = (kt)^n} \tag{8}$$

$$\boldsymbol{k = k_0 \mathbf{exp}\left(\frac{-E_A}{RT}\right)} \tag{9}$$

t is the isothermal time, k_0 a pre-exponential constant, *k* transformation rate, n is the shape factor (known as Avrami constant), T the absolute temperature in (Kelvin), R the gas constant and E_A is the activation energy to be determined. The KJMA equation is valid if a random homogenous nucleation in an infinitely large bulk is assumed and the nuclei grow without interfering with other nuclei. For the growth of the oxides it is not strictly fulfilled as it has been reported to nucleate in grain boundaries [111]. There are modified models taking grain boundary nucleation into account [117] and are successfully used [4]. These models modify Eq. (6) with an impingement factor ε. Its differential state and integrated state is shown in Eq. (10) and Eq. (11)

$$\mathbf{df = (1 - f)^{\varepsilon} dx} \tag{10}$$

$$\mathbf{f = 1 - (1 + x(\varepsilon - 1))^{\frac{1}{1-\varepsilon}}} \tag{11}$$

A relation to the impingement factor ε to physical properties is lacking in the literature. Values below unity are related to a weak impingement and values above unity are related to a strong impingement. The probability of nuclei interfering with each other increases, *e.g.* in grain boundaries, if a strong impingement occurs. If the nuclei are positioned far from each other with less risk of interfering, the impingement is weak followed by a slower transformation rate as compared to Eq. (6) [4]. During the transformation in TiCrAlN tests of the impingement factors are performed and values of ε between 0.1 and 3 have been investigated. Therefore Eq. (11) is rewritten to Eq. (12). In case for ε=1 the equation takes the form of Eq. (13)

$$\mathbf{ln\left(\frac{(1 - f)^{(1-\varepsilon)}}{\varepsilon - 1}\right) = n(lnk + lnt)} \tag{12}$$

$$\mathbf{ln(- ln(1 - f)) = n(lnk + lnt)} \tag{13}$$

According to [111] [117] this model describes very well a system with a nucleation and the fitting procedure will be similar to the KJMA equation [4]. However, here this nucleation mechanism is a mixture of the decomposition and nucleation of oxides.

Lines with the corresponding ε values can be obatined by plotting the left side of Eq. (12) vs. ln t for some of the above mentioned impingement factors. The real situation is described by the straight lines which cannot be fulfilled by all ε values, but the best linear fit with the minimum residuum yields the optimum ε value. In Figure 43, a randomly selected number of the impingement factors ε, used for the Eq. (12) and (13), are plotted vs. lnt for $Ti_{0.16}Cr_{0.36}Al_{0.48}N$ at 1100°C.

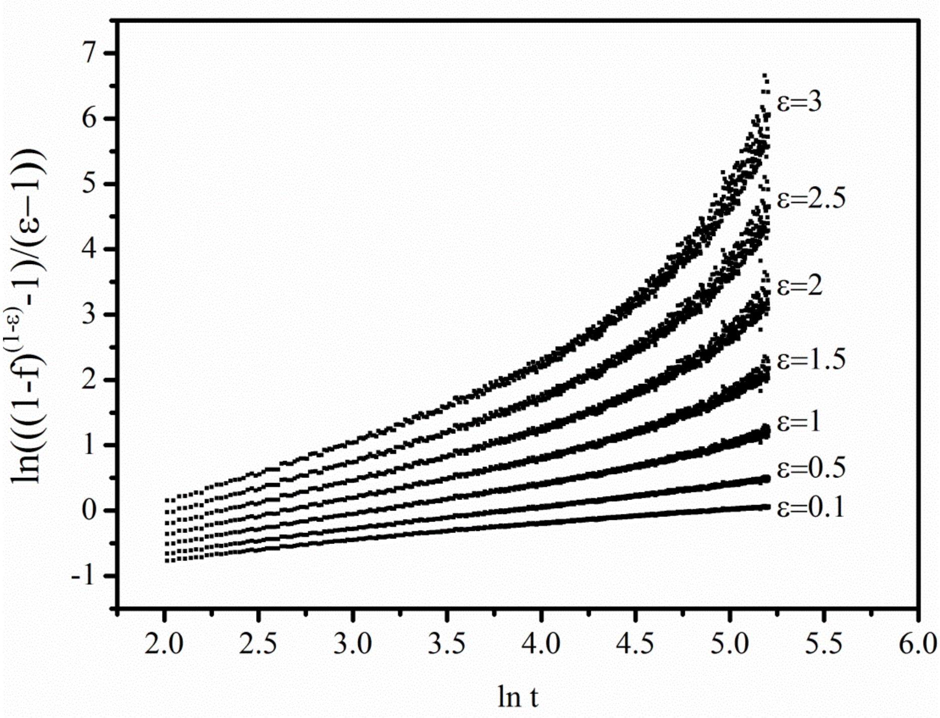

Figure 43: Plots of the Eq.(12) and Eq.(13) *vs.* lnt for randomly selected impingement factors ε.

For low ε-values the plots show a negative curvature and for higher ε-values a positive curvature. This trend can be seen for all samples, investigated phases and temperatures.

The residual plot and the R^2 –values can be compared [4] to determine the quality of the linear plots for all ε-values. In that way the best ε-values can be selected which describes the real situation. Depending on the temperature and the composition, the ε-values between 0.1 and 3 represent the best fits. These steps have to be performed for the other compositions and temperatures. From Eq. (12) and Eq. (13), the intersection with the y-axis is equal to n x ln k. n is the slope of the curve. For the calculation of the activation energy the slope is needed. Therefore, the Eq. (9) can be written as Eq. (14):

$$\ln k = \ln k_0 - \frac{E_A}{RT} \tag{14}$$

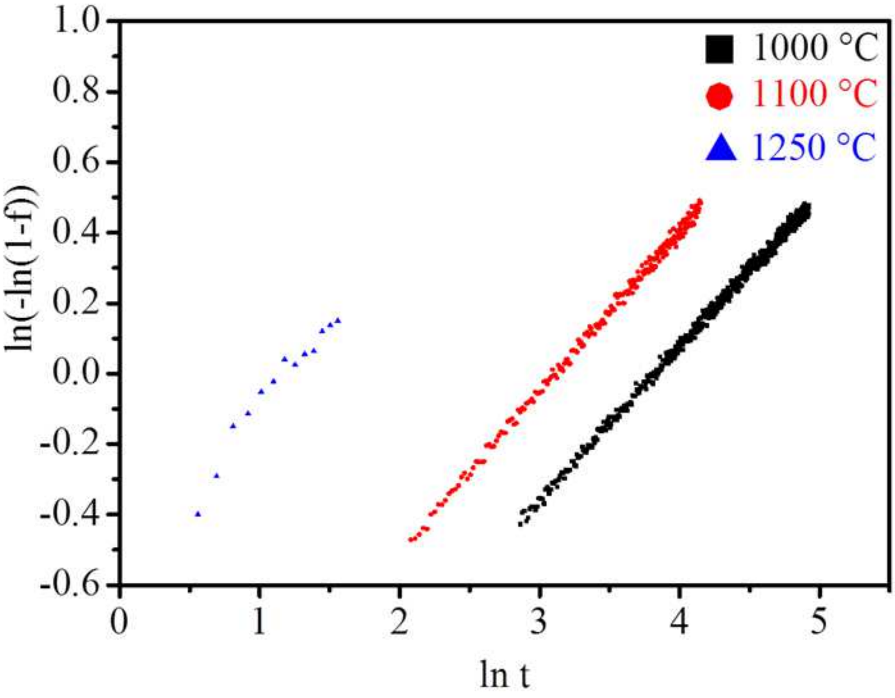

Figure 44: Plots of the KJMA equation vs. lnt at 1000 °C, 1100 °C and 1250 °C for $Ti_{0.16}Cr_{0.36}Al_{0.48}N$. With linear fitting of these straight lines, the slope and the intersection with the y-axis can be calculated.

Plotting ln k *vs*. T^{-1} results in linear functions with a slope determined by the Eq. (14) and finally in Arrhenius Plots. Hence, this equation describes a well-known linear function y = mx+b, where y = ln k, b= ln k_0, m = $-E_A/R$ and x = 1/T. The activation energy is calculated by the slope and multiplied with the gas constant R.

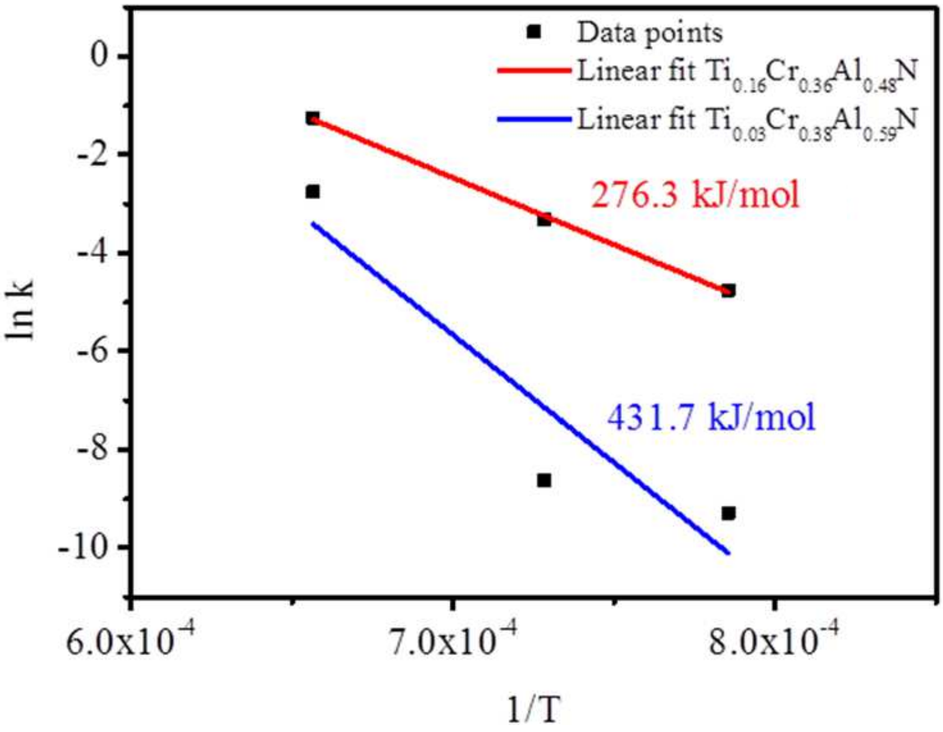

Figure 45: Arrhenius plot of extracted data from Eq.(14), the fitted lines and data points according to Eq.(12) and Eq.(13). Arrhenius plot of α-Al_2O_3.

Figure 45 shows the Arrhenius plot according to Eq.(14) and the corresponding linear fits of α-Al_2O_3 for $Ti_{0.03}Cr_{0.38}Al_{0.59}N$ and $Ti_{0.16}Cr_{0.36}Al_{0.48}N$. A clear difference in the slope of both compositions, and therefore in the activation energy can be seen. For $Ti_{0.03}Cr_{0.38}Al_{0.59}N$ the activation energy is 431.7 kJ mol^{-1} and for $Ti_{0.16}Cr_{0.36}Al_{0.48}N$ $_{59}N$ the activation energy is 276.3 kJ mol^{-1}. Including an impingement parameter whose value depends on the nucleation site (*e.g.* grain boundary or bulk site) [89] [117] has also been tested and results in small changes in the activation energies when the impingement parameter (ε) is varied in the range of 0.5-2.This fact is illustrated in Figure 46.

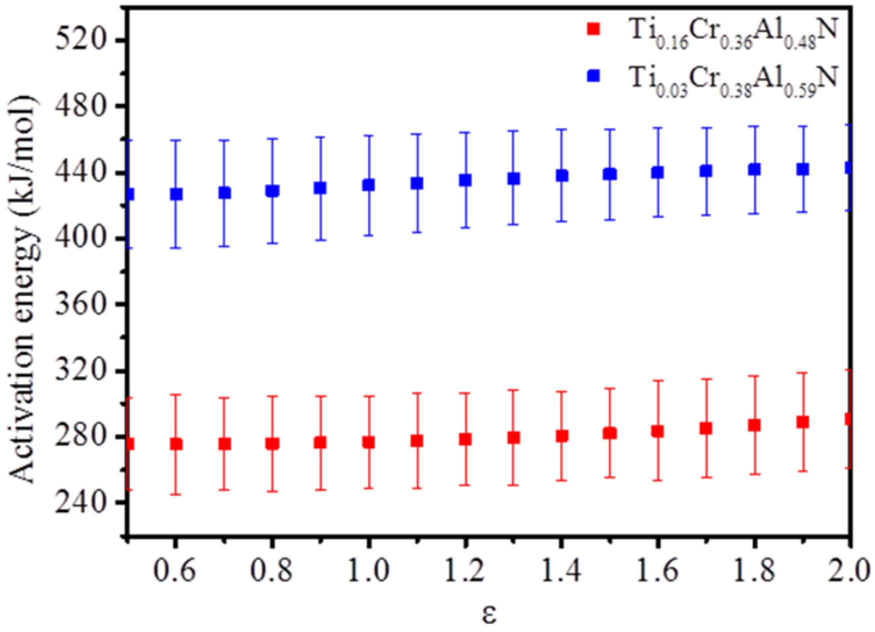

Figure 46: Activation energies *versus* ε–values of both compositions. The error bars are the standard error of the linear fit proceeding.

8.5.1 Discussion

The calculated value 431.7 kJ mol^{-1} of α-Al_2O_3 for $Ti_{0.03}Cr_{0.38}Al_{0.59}N$ agrees very well with the value 450 kJ mol^{-1} determined for the diffusion of oxygen in polycrystalline Al_2O_3 [118] [119] and is in the range of values reported by other authors [120] [121] [122]. The observation in my measurement suggests that the oxide layer is principally α-Al_2O_3. According to my XRD-pattern in Figure 31, only a small amount is transformed into θ-Al_2O_3, specially at higher temperatures, and mainly α-Al_2O_3 is observed with a small amount α-Cr_2O_3.

It is known from the literature, that the Gibbs free energy of α-Al_2O_3 formation is more negative than that of α-Cr_2O_3; therefore, AlN is preferably to be oxidized [123]. However, for lower temperatures (1000 °C and 1100 °C) a continuous α-Al_2O_3 layer did not form, so here a α-$(Cr,Al)_2O_3$ oxide scale, which means that the Al activities in TiCrAlN coatings are not high enough for the coating with low Ti-content and high Al-content.

A similar explanation was also found in [123], however for oxidation of CrAlN [123]. And this has a very positive effect on the coating and this can be a reason why the amount of α-Al_2O_3 are low for the coatings with low for $Ti_{0.03}Cr_{0.38}Al_{0.59}N$.

The reason for a higher activation energy could be as follows. In the literature, there is a transition of the oxide scale, consisting mainly of α-Cr_2O_3 with some amount of α-Al_2O_3 at lower temperature, and at higher temperature α-Al_2O_3 is the main oxide with traces of α-Cr_2O_3 [90] [124].

In $Ti_{0.03}Cr_{0.38}Al_{0.59}N$ a similar conclusion can be drawn. Both oxide scales, α-Al_2O_3 and α-Cr_2O_3 were observed, whereas α-Al_2O_3 dominates slightly over α-Cr_2O_3 at lower temperature (see Figure 39a), and at the highest temperature 1250 °C α-Al_2O_3 is the main oxide (see Figure 41 a)). More energy is needed to oxidize the $Ti_{0.03}Cr_{0.38}Al_{0.59}N$ sample, which shows a higher oxidation resistance. The high Al-content in $Ti_{0.03}Cr_{0.38}Al_{0.59}N$ doesn't mirrored in the peak intensities of α-Al_2O_3 in the XRD-pattern, but, now it shows definitely an affect in the activation energy, a positive impact of the oxidation resistance.

The calculated value 276.3 kJ mol^{-1} of $Ti_{0.16}Cr_{0.36}Al_{0.48}N$ agrees very well with the value 271 kJ mol^{-1} [119], however, the value is higher than the values reported by Suryanarayana [124]. One reason is, as Brown *et al.* reported [119], likely a higher impurity level in the AlN powder used in [124]. Considering that the TiCrAlN coatings and powders used are fabricated with an industrial evaporation system, which shows definitely a high amount of impurities (see Chapter 4, Figure 8), I could conclude the same argument. However, both compositions exhibit impurities. The difference in the activation energies of $Ti_{0.16}Cr_{0.36}Al_{0.48}N$ and $Ti_{0.03}Cr_{0.38}Al_{0.59}N$ is the variation of composition and the different growth of oxide which is illustrated in Figure 41. For higher Ti-content in TiCrAlN, the affinity of forming oxides is much higher as described in Section 8.4.1 and 8.3.2.

8.6 h-AlN transformation in vacuum and oxidation

This sub-chapter summarizes our results of the growth of the h-AlN phase in the vacuum atmosphere [125] in order to compare these results with the results of my real-time oxidation experiments [126].

Figure 47 illustrates the evolution of the fraction transformed of the h-AlN (100) of a) $Ti_{0.16}Cr_{0.36}Al_{0.48}N$ and b) $Ti_{0.03}Cr_{0.38}Al_{0.59}N$ at 1000 °C, 1100 °C and 1250 °C in an oxidation atmosphere.

The calculation of the fraction of the h-AlN was performed with the synchrotron radiation data of the vacuum experiments. The data (integrated intensity) of the h-AlN phase of the oxidation experiment was normalized with integrated intensity of the plateau value of the full transformed h-AlN in the vacuum experiment (at 1150 °C) in order to ensure comparability and to get a fraction. With these data a conclusive statement about the fraction of the evolution of h-AlN can be done (see Chapter 6.9). In Figure 47 a), it is obvious that the increase of the transformation is very fast in the beginning of the transformation.

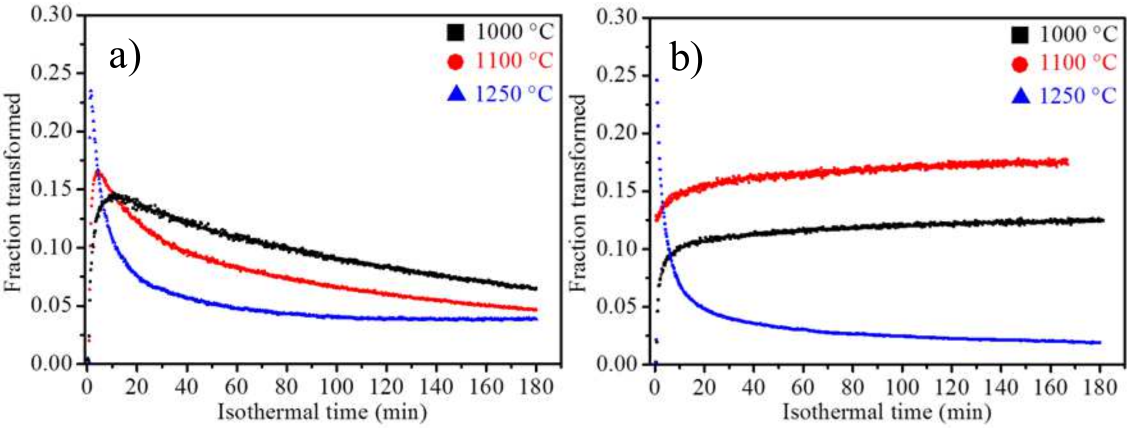

Figure 47: Fraction transformed of h-AlN (100) of a) $Ti_{0.16}Cr_{0.36}Al_{0.48}N$ and b) $Ti_{0.03}Cr_{0.38}Al_{0.59}N$ at 1000 °C, 1100 °C and 1250 °C in the oxidation atmosphere.

For 1000 °C, a maximum value 0.15 of the fraction transformed is reached after ~11 minutes. With higher temperature, the maximum is shifted to lower isothermal times and to higher fraction values. At 1100 °C the maximum value 0.17 is reached after ~6 min and at 1250 °C the maximum value 0.23 is reached after ~ 2 min. At 1250 °C, a very fast growth of the h-AlN phase can be measured. This fact can be rudimentarily seen at the onset of the growth in Figure 47 a).

After reaching the maximum values, the fraction value decreases with isothermal time. At 1000 °C the h-AlN decreases very slowly and after 70 min it reveals a linear behaviour. At 1100 °C, the decrease of the h-AlN phase is faster compared to the measurement at 1000 °C. At 1250 °C, the h-AlN decreases very fast and shows an exponential decrease. In Figure 47 b), $Ti_{0.03}Cr_{0.38}Al_{0.59}N$, the h-AlN fraction transformed for 1000 °C increases very fast at the beginning of the evolution and slows down with time. After ~150 min there is no significant change in the fraction transformed. A plateau is reached. The same situation is observed for 1100 °C, but with a higher fraction transformed value. Due to beam loss during the measurements, the last 12 minutes could not be recorded. At 1250 °C, the onset of the evolution is very fast and after ~2 min the maximum fraction transformed value is reached. After that, the curve shows an exponential decrease. This curve exhibits almost the same situation as for the sample $Ti_{0.16}Cr_{0.36}Al_{0.48}N$ at 1250 °C in Figure 47 a).

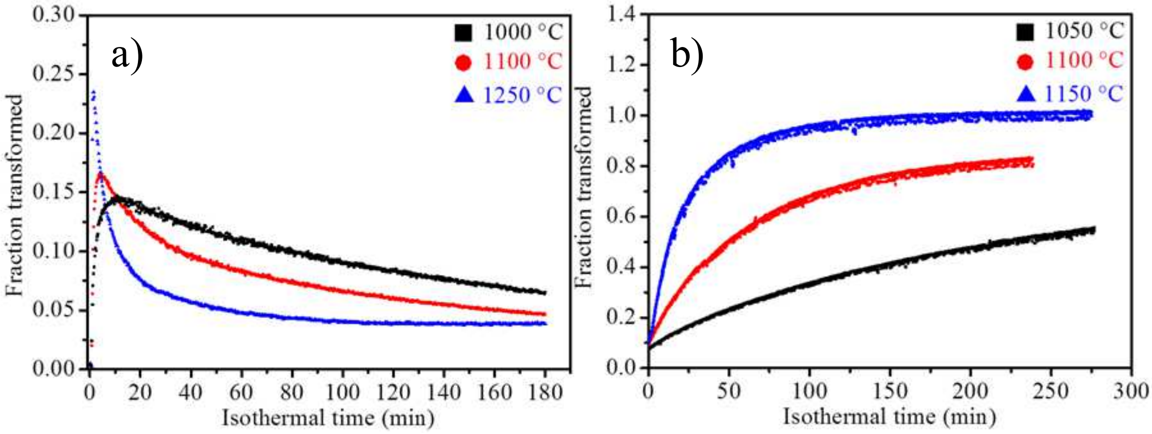

Figure 48: Fraction transformed h-AlN (100) of $Ti_{0.16}Cr_{0.36}Al_{0.48}N$ as a function of isothermal time in a) oxidation atmosphere and b) in vacuum at 1000 °C, 1100 °C and 1250 °C and respectively 1050 °C, 1100 °C and 1150 °C

In Figure 48 a), the h-AlN (100) evolution of $Ti_{0.16}Cr_{0.36}Al_{0.48}N$ in oxidation atmosphere is shown and in Figure 48 b), the evolution of the same h-AlN (100) phase of $Ti_{0.16}Cr_{0.36}Al_{0.48}N$ in a vacuum environment is presented. For 1050 °C, the fraction transformed of the h-AlN grows slowly without reaching a plateau value within

275 min. For 1100 °C, the onset of the growth is fast and slows down with time without reaching a plateau value. Due again to the beam loss the last 40 minutes could not be measured. For 1150 °C, the increase is fast in the beginning of the transformation and slows down with time. A plateau is reached after ~180 min which indicates a full transformation of h-AlN, a fraction transformed value of ~1.

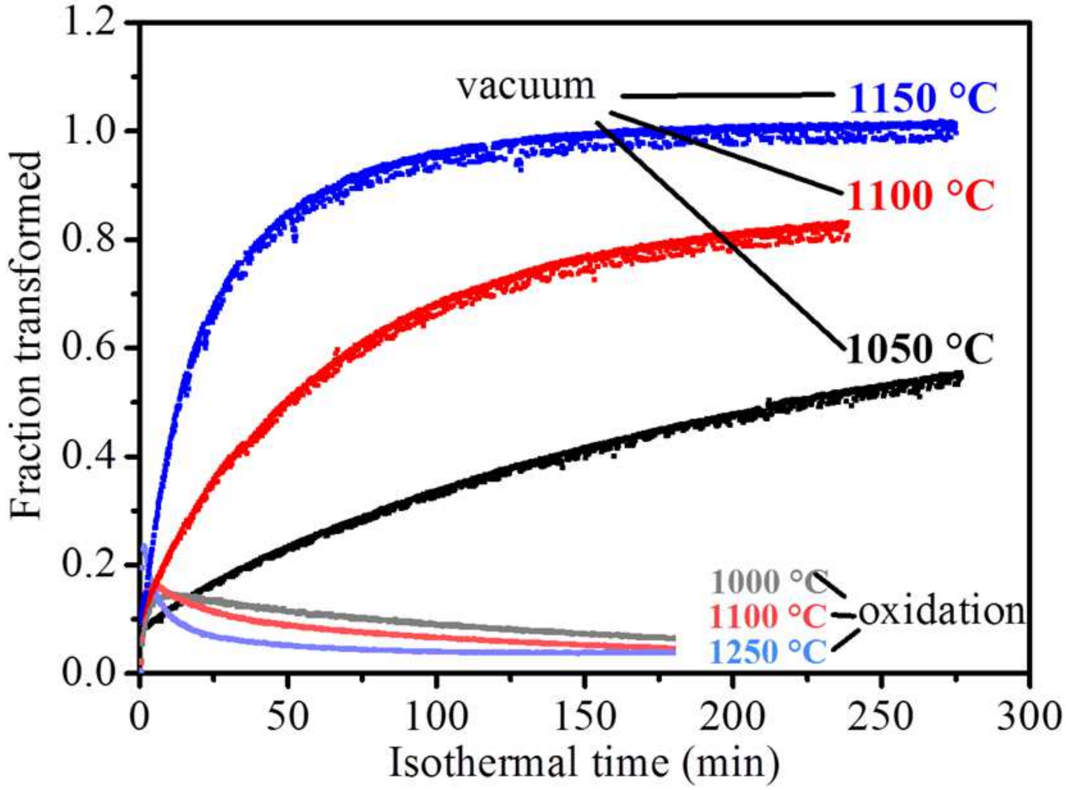

Figure 49: Summarized fraction transformed of h-AlN as a function of isothermal time at three different temperatures for $Ti_{0.16}Cr_{0.36}Al_{0.48}N$ in oxidation atmosphere and in vacuum environment [127] [126].

Figure 49 presents the h-AlN (100) evolution of $Ti_{0.16}Cr_{0.36}Al_{0.48}N$ in an oxidation atmosphere and in a vacuum environment for different indicated temperatures in one plot. This plot illustrates the differences of the fraction of the h-AlN evolution in Figure 48 a) and Figure 48 b) more pronounced. With this result it can be clearly seen that in the oxidation atmosphere only a max fraction of ~0.23 of the h-AlN is transformed, for short period of isothermal time, whereas a full transformation is reached in a vacuum environment.

8.6.1 Discussion

It is evident from my peak fitting data analysis that the evolutions of the h-AlN phase in my real-time oxidation experiment for the compositions $Ti_{0.16}Cr_{0.36}Al_{0.48}N$ and $Ti_{0.03}Cr_{0.38}Al_{0.59}N$ show different behaviour.

By comparing the h-AlN phase evolution of the vacuum annealing experiment ($Ti_{0.16}Cr_{0.36}Al_{0.48}N$) with the h-AlN phase evolution of the oxidation experiment ($Ti_{0.16}Cr_{0.36}Al_{0.48}N$), it is seen that, additionally, these behaviours are also different. Furthermore, the data analysis of the h-AlN phase evolution (in my oxidation setup) at 1000 °C confirms my rough observation from the lineouts in Figure 29 at this temperature. For $Ti_{0.03}Cr_{0.38}Al_{0.59}N$, the presented curves at 1000 °C and 1100 °C of the h-AlN in the real-time oxidation experiment exhibit similar trends as the h-AlN evolution for $Ti_{0.16}Cr_{0.36}Al_{0.48}N$ in the vacuum annealing experiment at 1050 °C and 1100 °C.

A full transformation of the h-AlN phase in my oxidation experiment, as indicated here as a plateau in $Ti_{0.03}Cr_{0.38}Al_{0.59}N$, does not correspond to a complete transformation of c-CrAlN into h-AlN as indicated in our vacuum annealing experiment. My calculation of the fraction transformed value has shown this fact directly (compare Figure 47 b) with Figure 48 b)). The data analysis shows that only the maximum fraction value of 0.23 has been reached at 1250 °C and furthermore, this value is reached for a short time before the h-AlN phase decreases. In other words, only 23% of the possible h-AlN transformation takes place, for a short time. Due to the very fast growth of the h-AlN phase at 1250 °C in both compositions, it was possible with the fast detector and with the optimized detector configuration to record 5 data points before the maximum of the fraction value is reached.

At first, the different behaviour of the h-AlN evolution can be explained by the different observed oxidation processes. Obviously, the protective oxide scale $(Cr,Al)_2O_3$ is more effective in $Ti_{0.03}Cr_{0.38}Al_{0.59}N$ compared to the oxide scale composed of α-$(Cr,Al)_2O_3$ and TiO_2 in $Ti_{0.16}Cr_{0.36}Al_{0.48}N$. In my real-time oxidation experiment a finished transformation of the h-AlN evolution is measured for $Ti_{0.03}Cr_{0.38}Al_{0.59}N$, but not a complete. At this point I can repeat my conclusion. The formed oxide scales α-$(Cr,Al)_2O_3$, in $Ti_{0.03}Cr_{0.38}Al_{0.59}N$, provide a nearly protective effect against a complete decomposition into the decomposition products (see section 8.2) of the metastable c-TiCrAlN phase. The phase evolution of the h-AlN confirms my conclusion. The transformation of h-AlN evolution is protected by the described oxide scale at 1000 °C and 1100 °C for $Ti_{0.03}Cr_{0.38}Al_{0.59}N$ and only maximum 17 % (0.17) of the h-AlN is transformed (see Figure 47). Therefore, there is no complete transformation and this analysis of the evolution of the h-AlN phase also confirms this conclusion.

For $Ti_{0.16}Cr_{0.36}Al_{0.48}N$, the transformation of h-AlN evolution is also protected by the described oxide scale. But here, the transformation of the h-AlN evolution stops after ~11 min, ~6 min and ~2 min, and the h-AlN phase starts to decrease. The decrease of the h-AlN is associated with a transformation of the h-AlN into θ-Al_2O_3, and therefore an oxidation of the h-AlN phase. At 1250 °C, $Ti_{0.03}Cr_{0.38}Al_{0.59}N$ shows the same oxidation behaviour of the h-AlN evolution as shown for $Ti_{0.16}Cr_{0.36}Al_{0.48}N$, a transformation of the h-AlN into θ-Al_2O_3.

Secondly, the data analysis shows directly, that the protective oxide scale $(Cr,Al)_2O_3$ for $Ti_{0.03}Cr_{0.38}Al_{0.59}N$ provide a better protective effect against the complete decomposition (see section 8.2) into the decomposition products compared to $Ti_{0.16}Cr_{0.36}Al_{0.48}N$. This fact can be directly seen in Figure 47. For 1000 °C, the fraction shows a value of 0.1 for $Ti_{0.03}Cr_{0.38}Al_{0.59}N$ after ~20 min compared to 0.15 for $Ti_{0.16}Cr_{0.36}Al_{0.48}N$, 50 % more based on this observation. The h-AlN transformation is less distinct in $Ti_{0.03}Cr_{0.38}Al_{0.59}N$. For 1100 °C, the fraction shows a value of 0.15 for $Ti_{0.03}Cr_{0.38}Al_{0.59}N$ after ~10 min compared to 0.17 for $Ti_{0.16}Cr_{0.36}Al_{0.48}N$, respectively. Here it can be noted, that in $Ti_{0.16}Cr_{0.36}Al_{0.48}N$, the increase of the h-AlN evolution becomes faster for higher temperatures, and with higher temperature the effect of the oxidation process becomes stronger.

Thirdly, the fact that the first appearance of h-AlN phase in vacuum is at first at 1150 °C for $Ti_{0.16}Cr_{0.36}Al_{0.48}N$, and in my oxidation experiment the same h-AlN phase appears at 1000 °C, which additionally starts to oxidize after the declared minutes, support one fact distinctly.

Here obviously, I can confirm my assumption that the spinodal decomposition (which suppressed the h-AlN transformation and increase the onset-temperature of the h-AlN transformation, which results in a higher thermal stability) has positive stability effect in vacuum for $Ti_{0.16}Cr_{0.36}Al_{0.48}N$, but has a negative effect in air. The evidence for this fact will be clearer in the last section 8.7. So, the h-AlN domains are surrounded by the c-TiCr and c-CrAlN domains (caused by the spinodal decomposition) or, as Forsén's *et al.* decomposition model described, the Al-rich c-TiCrAlN domains are not stable and, therefore, there is a transformation into h-(Ti)AlN with traces of Ti inside these domains [20]. It seems that these traces promote the oxidation of the h-AlN for higher Ti-content in $Ti_{0.16}Cr_{0.36}Al_{0.48}N$ which was shown in Figure 47.

8.7 Relation between coating grain *vs.* h-AlN *vs.* oxide

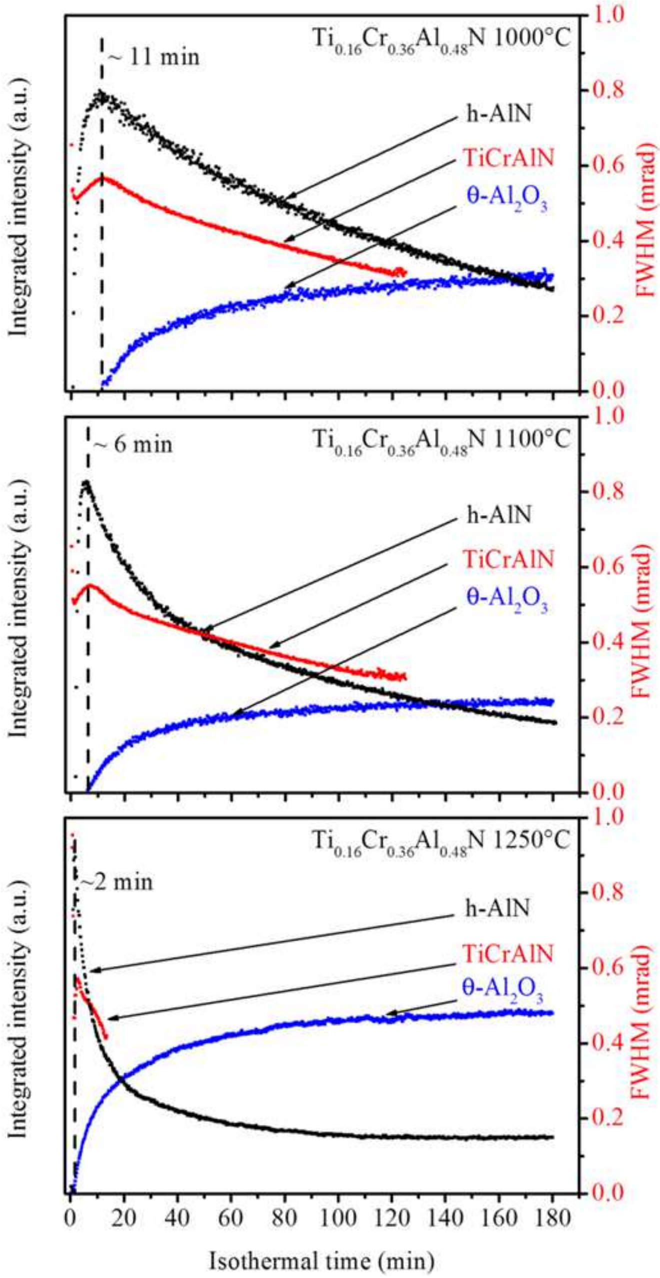

Figure 50: The integrated intensity of h-AlN(**black**) and θ−Al_2O_3(**blue**), and the FWHM of the c-TiCrAlN(**red**) of $Ti_{0.16}Cr_{0.36}Al_{0.48}N$ at 1000 °C, 1100 °C and 1250 °C. The arrows mark the curves for a better view. On the left side is the scale for the integrated intensity related to h-AlN(**black**) and θ−Al_2O_3(**blue**), and on the right side is the scale for FWHM related to c-TiCrAlN(**red**). This plot [88] illustrates the relation between FWHM evolution of TiCrAlN (FWHM) coating, the h-AlN and the emerging Oxide θ−Al_2O_3.

Figure 50 illustrates the correlation between the transformation of the h-AlN, the new emerging θ-Al_2O_3, and the evolution of the FWHM of the c-TiCrAlN coating as a function of isothermal time. On the left side is the integrated intensity and represent the scale for the evolution of the h-AlN(black) and the new emerging θ-Al_2O_3(blue). On the right side is the FWHM and represent the scale for evolution of FWHM of c-TiCrALN(red). As described in Chapter 8.5, the h-AlN reaches a maximum value after around ~11 min, ~6 min and ~2 min. This time step is correlated with the new emerging θ–Al_2O_3. The h-AlN phases starts to oxidize and transform into θ-Al_2O_3 as described in Chapter 8.1. At the same time step, a local maximum of the FWHM of the TiCrAlN is reached. The mechanism behind this observation can be described as follows.

8.7.1 Discussion

During the spinodal decomposition CrAlN domains and TiCrN domains build up and at the same time h-AlN starts to transform. In the meanwhile oxygen diffuses into the coating and oxides will form. Additionally, Cr, Ti and/or Al can also diffuse to the oxide scale interface and form $(Cr,Al)_2O_3$ and porous TiO_2. This confirms my conclusion that $Ti_{0.16}Cr_{0.36}Al_{0.48}N$ in my oxidation experiment does not provide a good protective effect against the described decomposition. After 11 min, 6 min and 2 min, the h-AlN domains are surrounded by these c-TiCr and c-CrAlN domains and the onset of the transformation of h-AlN into θ-Al_2O_3 starts. The Al-rich c-TiCrAlN domains are not stable and therefore there is a transformation into h-(Ti)AlN with traces of Ti inside these domains [20], as Forsén *et al.* have described the decomposition model of TiCrAlN in their *ex-situ* annealing experiment.

Therefore, further oxygen diffusion, supported by the high Ti-content, promotes the transformation of h-AlN into θ-Al_2O_3. This behaviour is observed for all temperatures in the $Ti_{0.16}Cr_{0.36}Al_{0.48}N$. The higher the temperature is the faster the transformation of h-AlN takes place. For $Ti_xCr_{1-x}Al_{0.61}N$ with small amount of Ti ($x \approx 0$), the nucleation and growth of the h-AlN precipitates at grain boundaries, as mentioned above. Under the assumption, that the oxidation process attack the grain boundaries, a protective oxide layer $(Cr,Al)_2O_3$ will build up at the grain boundaries and no significant porous TiO_2 will form. Therefore the growth of the h-AlN is undisturbed and the limited activity of Al in h-AlN hinders a further transformation of the h-AlN, and into a θ-Al_2O_3. The observed plateau of the h-AlN transformation can be interpreted as impingement of the h-AlN domains and the oxide layer. In addition to that, the mentioned limited Al activity is mirrored in the low growth kinetic of the h-AlN for the sample with low Ti-content [94] and this low Al activity leads finally to a low affinity for the h-AlN in $Ti_{0.03}Cr_{0.38}Al_{0.59}N$ to oxidize.

Chapter 9

9. Summary

The a.d. compositions of the $Ti_{0.03}Cr_{0.38}Al_{0.59}N$ and $Ti_{0.16}Cr_{0.36}Al_{0.48}N$ coatings deposited by industrial scale cathodic arc evaporation are mainly B1 structure type. For the *in-situ* synchrotron radiation x-ray powder diffraction (SR-XRPD) real-time oxidation studies in air the coatings have to be ground into powder. A self-designed thermal annealing setup was constructed to perform the real-time oxidation studies on c-TiCrAlN coatings and to simulate the conditions in a high performance cutting tool with a heating rate of 3000 K min^{-1} up to 1000 °C, 1100 °C and 1250 °C. By using a fast Perkin Elmer 1621 detector in read-out mode with 15 seconds exposure time per diffraction pattern, a time resolved evolution of the oxidation process could be measured. The composition $Ti_{0.03}Cr_{0.38}Al_{0.59}N$, shows a superior oxidation resistance compared to the composition $Ti_{0.16}Cr_{0.36}Al_{0.48}N$ due to a time delayed dense growth of a convolute thin oxide scale composed of α-Al_2O_3 and α-Cr_2O_3. The decrease of the peak intensity of the cubic structure indicates mainly an oxidation process, due to the time correlated growth of oxides, and, additionally, a decomposition of the c-TiCrAlN into the decomposition product h-AlN.

Assumptions made in the literature about the oxidation resistance of TiCrAlN and the prevented complete decomposition due to the oxidation process, are confirmed by the *in-situ* SR-XRPD real-time oxidation studies. The higher oxidation resistance is related to convoluted oxide α-$(Cr,Al)_2O_3$, and the α-$(Cr,Al)_2O_3$ oxide scale likely provide a protective effect against a complete decomposition. Reaction kinetic studies of α-Al_2O_3 show a low Al activity in $Ti_{0.03}Cr_{0.38}Al_{0.59}N$. This result is supported by the observed low growth of α-Al_2O_3 and the observed strong stability of the cubic structure. This results in a high activation energy for a complete oxidation. Both compositions show different oxidation behaviour accompanied with different evolution of the h-AlN. Up to 1250 °C, a complete transformation of the h-AlN is not observed in an air atmosphere in both compositions. For $Ti_{0.16}Cr_{0.36}Al_{0.48}N$, the h-AlN transformation stops after several minutes and starts to oxidize and transforms into θ-Al_2O_3 whereas for $Ti_{0.03}Cr_{0.38}Al_{0.59}N$, the h-AlN transformation reaches a plateau after 180 min which, here, does not indicate a complete transformation of h-AlN. In this connection, the studied decomposition mechanisms of the c-TiCrAlN in vacuum also appear in the oxidation experiment of the coating in air. The evidence for the decomposition mechanisms were found in the time resolved evolution of the FWHM and of the d-spacing, in both experimental setups. The spinodal decomposition process, promoted by the higher Ti-content in $Ti_{0.16}Cr_{0.36}Al_{0.48}N$, leads to a decreased oxidation resistance due to the growth of porous TiO_2 in the formed enriched c-TiN (c-TiCr(Al)N) domains which benefits the growth of α-Al_2O_3, which in turn lead to a higher Al activity and this results in a lower activation energy for a complete oxidation. The spinodal decomposition in these compositions shows a negative effect on the oxidation process in air, whereas it leads to a higher thermal stability in vacuum.

Chapter 10

10. Conclusion and outlook

10.1 Conclusion

According to my knowledge, this is the first time to present results from a high temperature *in-situ* SR-XRPD real-time oxidation experiment on this compositional $Ti_xCr_{\sim 0.37}Al_{1-0.37-x}N$ material system in the literature. The applied time resolved SR-XRPD technique is a powerful tool to perform oxidation experiments on TiCrAlN material systems on short timescales. With this technique, time resolved phase transformations and oxidation processes could be measured.

The higher oxidation resistance in $Ti_{0.03}Cr_{0.38}Al_{0.59}N$ is related to thin dense convoluted α-$(Cr,Al)_2O_3$ oxide scale. The assumption in the literature that the higher oxidation resistance in TiCrAlN material system is likely related to α-$(Cr,Al)_2O_3$ oxide scale can be confirmed by my *in-situ* SR-XRPD real-time oxidation experiment. The methodological peak fitting approach for the *in-situ* SR-XRPD real-time oxidation data analysis reveal that the B1 structure $Ti_{0.03}Cr_{0.38}Al_{0.59}N$ is still remaining up 1250 °C for 30 min annealing in air. The kinetic studies show that the activation energy of α-Al_2O_3 is 431.7 kJ mol^{-1} for $Ti_{0.03}Cr_{0.38}Al_{0.59}N$, whereas the activation energy for $Ti_{0.16}Cr_{0.36}Al_{0.48}N$ is 276.3 kJ mol^{-1}, which supports the observation of the higher oxidation resistance of the $Ti_{0.03}Cr_{0.38}Al_{0.59}N$ coating. The oxidation of the cubic structure is composed of the oxides scale α-$(Cr,Al)_2O_3$, TiO_2 and the decomposition product h-AlN.

So far, it was known from the literature that the addition of Cr delay the formation and growth of h-AlN, in vacuum. With my real-time oxidation setup it was shown that the formation of h-AlN is additionally strongly suppressed in air, and the formation of h-AlN starts to oxidize, depending on the decomposition process and Ti content.

Additionally, in this thesis it is reveal that the oxidation process severely hinders the complete decomposition of my $Ti_xCr_{\sim 0.37}Al_{1-0.37-x}N$ system, also with respect to the different decomposition mechanisms. So far, similar observation was known for the ternary system CrAlN.

These results provide new knowledge of the temporal sequence of the growth of oxides, the temporal sequence of the oxidation of the coating (-peak) itself and the temporal sequence of the phase transformation of $Ti_xCr_{\sim 0.37}Al_{1-0.37-x}N$, in an air environment.

10.2 Outlook

The next step must be to deposit coatings with these compositional content, or similar compositions with low Ti-content, on substrates. But additionally, a local pressure should be applied directly on the coating to prevent a strong bending caused by the coating-substrate reaction. Therefore, this leads to a better direct correspondence to a real-time cutting process. Due to the analysed data, in the first 15 min of my oxidation experiments there is a thermal expansion in the d-spacing of the c-TiCrAlN. So, one can assume a high stress in the coating. From the data, it can be assumed that if there is a contact and a pressure between a cutting edge and the c-TiCrAlN coating, the thermal expansion can lead to a counter pressure and for a short time there is an equilibrium between the pressure of the cutting edge and the coating. This short equilibrium state can have a positive effect on the oxidation resistance and mechanical properties. Similar experiments were also performed in TiAlN. The formation of h-AlN still limits the high temperature properties and the details regarding in its transformation is lacking. Therefore it is very important to study the h-AlN phase evolution in c-TiCrAlN under oxidation atmosphere in more detail and try to do kinetic studies on the h-AlN. Here, the temperature range depends on the composition. Based on the coating-substrate reaction I observed textured coatings. Here, an impact of the texture on the oxidation resistance may have been possible. Based on the data analysis, I observed a short time delay of the growth of the α-$(Cr,Al)_2O_3$ components. A further investigation in this process can maybe lead to a better understanding of the suggestion that by adding of Al to CrN, which is related to an altered bond structure with a stronger Al-N bonds, nitrogen release can be suppressed which stabilizes the cubic structure. For further studies on this material system in air, I would vary the Ti-content close from 3 at. % to 16 at. %, and with a constant Al-content of ~ 60 at. %.

11. Publications

Publication in connection to the thesis:

- Y. H. Chen, L. Rogström, D. Ostach, N. Ghafoor, M. P. Johansson-Joesaar, N. Schell, J. Birch and M. Oden, “Effects of decomposition route and microstructure on h-AlN formation rate in TiCrAlN alloys,” *Journal of Alloys and Compounds*, Vol. 691, p 1024-1032, 2017.

- D. Ostach, J. Schroeder, Y.H. Chen, L. Rogström, N. Ghafoor, M.P. Johansson-Jõesaar, N. Schell, J. Birch and A.Schreyer “Oxidation Behavior of TiCrAlN Coatings Studied by *in situ* Synchrotron Radiation X-ray Powder Diffraction”, *Surface and Coatings Technology,* submitted (in progress).

- D. Ostach, Y.H. Chen, L. Rogström, J. Schroeder, N. Ghafoor, M.P. Johansson-Jõesaar, N. Schell, J. Birch and A.Schreyer “Oxidation Behavior of h-AlN Formation in TiCrAlN Alloys Studied by *in situ* Synchrotron Radiation X-ray Powder Diffraction” (in progress).

Publications:

- P. Biplab, J. L. Schroeder, S. Kerdsongpanya, N. V. Nong, N. Schell, D. Ostach, J. Lu, J. Birch and P. Eklund, “Mechanism of Formation of the Thermoelectric Layered Cobaltate Ca3Co4O9 by Annealing of CaO–CoO Thin Films,” *Adv. Electron. Mater.,* vol. 1, p. 1400022, 2015.

- Y. Zhong, D. Ostach, M. Scholz, S. W. Epp, S Techert, I Schlichting, J Ullrich and F S Krasniqi, “Hot carrier relaxation in CdTe via phonon-plasmon modes”, Journal of Physics: Condensed Matter Vol. 29, 9, 2017.

12. References

[1] “www.chalmers.se,” 2015. [Online]. Available: www.chalmers.se/fy.

[2] “www.staton.sk,” 2015. [Online]. Available: www.staton.sk.

[3] J. Birch, “In-situ X-ray scattering during the Birth and Death of Cutting Tool Coatings,” in *DESY USER GEMS Satellite Meeting*, Hamburg, 2015.

[4] N. Norrby, Microstructural evolution of TiAlN hard coatings at elevated pressures and temperatures, Linköping: LiU-Tryck, 2014.

[5] T. Childs, Metal Machining: Theory and Applications, London: Arnold, 2000.

[6] N. Norrby, *Surf. & Coat. Technol.,* vol. 209, p. 203, 2012.

[7] O. Knotek, M. Bohmer and T. Leyendecker, *J. Vac. Sci. Technol.* , vol. A 4, p. 6, 1986.

[8] H. A. Jehn, S. Hofmann, V. Ruckborn and W. Munz, *J. Vac. Sci. Technol.*, vol. A 4, p. 6, 1986.

[9] A. Knutsson, M. P. Johansson, P. O. A Persson, L. Hultman and M. Odén, *Appl. Phys. Lett.,* vol. 93, p. 143110, 2008.

[10] A. Knutsson, M. P. Johansson, L. Karlsson and M. Odén, *J. Appl. Phys.*, vol. 108, p. 044312, 2010.

[11] B. Alling, A. V. Ruban, A. Karimi, O. E. Peil, S. I. Simak, L. Hultman and I. A. Abrikosov, *Phys. Rev.* , vol. B 75, p. 4, 2007.

[12] M. Hörling, L. Hultmann, M. Odén, J. Sjölen and L. Karlsson, *J. Vac. Sci.Technol.,* vol. A 20, p. 1815, 2002.

[13] M. Hörling, L. Hultmann, M. Odén, J. Sjölen and L. Karlsson, *Surf. Coat. Technol.*, vol. 191, p. 384, 2005.

[14] P. H. Mayrhofer, A. Hörling, L. Karlsson, J. Sjölen, T. Larsson, C. Mitterer and L. Hultman, *Appl. Phys. Lett.* , vol. 83, p. 10, 2003.

[15] M. Kawate, A. K. Hashimoto and T. Suzuki, *Surf. Coat. Technol.*, vol. 165, p. 163, 2003.

[16] B. Navinsek, P. Panjan and A. Cvelbar, *Surf. Coat. Technol.*, vol. 74, p. 1, 1995.

[17] J. C. Knight, *Wear,* vol. 138, p. 1, 1990.

[18] Y. C. Chim, X. Z. Ding, X. T. Zeng and S. Zhang, *Thin Solid Films*, vol. 517, p. 4845, 2009.

[19] J. Vetter, *Surf. Coat. Technol.* , Vols. 76-77, p. 719, 1995.

[20] R. Forsén, M. P. Johansson, M. Odén and N. Ghafoor, *Thin Solid Films*, vol. 534, p. 394, 2013.

[21] T. Sato, Y. Tada, M. Ozaki, T. Hoke and T. Besshi, *Wear,* vol. 178, p. 95, 1994.

[22] G. Berg, C. Friedrich, E. Broszeit and C. Berger, *Surf. Coat. Technol.* , vol. 86/87, p. 184, 1996.

[23] B. Navinsek, P. Panjan and I. Milosev, *Surf. Coat. Technol.*, vol. 97, p. 182, 1997.

[24] G. Bertrand, H. Mahdjoub and C. Meunier, *Surf. Coat. Technol.*, vol. 126, p. 199, 2000.

[25] X. Z. Ding, X. T. Zeng, Y. C. Liu, F. Z. Fang and G. C. Lim, *Thin Solid Films*, vol. 516, p. 1710, 2008.

[26] J. Lin, B. Mishra, J. J. Moore and W. D. Sproul, *Surf. Coat. Technol.*, vol. 202, pp.

3272-3283, 2008.

[27] M. A. Djouadi, C. Nouveau, O. Banakh, R. Sanjines, F. Levy and G. Nouet, *Surf. Coat. Technol.,* Vols. 151-152, p. 510, 2002.

[28] H. Hasegawa and T. Suzuki, *Surf. Coat. Technol.,* Vols. 188-189, p. 234, 2004.

[29] A. E. Reiter, V. H. Derflinger, B. Hanselmann, T. Bachmann and B. Sartory, *Surf. Coat. Technol.,* vol. 200, p. 2114, 2005.

[30] H. O. Gekendo and S. V. Subramanian, *Surf. Coat. Technol.*, vol. 149, p. 151, 2002.

[31] N. Schell and Seco Tools, Interviewees, *Questions about service life time of cutting tools.* [Interview]. October 2015.

[32] B. Alling, T. Marten, I. A. Abrikosov and A. Karimi, *J. Appl. Phys.*, vol. 102, p. 4, 2007.

[33] H. Lind, R. Forsén, B. Alling, N. Ghafoor, F. Tasnadi, M. P. Johansson, I. A. Abrikosov and M. Odén, *Appl. Phys. Lett.*, vol. 99, p. 091903, 2011.

[34] H. Willmann, P. H. Maryhofer, L. Hultmann and C. Mitterer, *J. Mater. Res.*, vol. 23, p. 11, 2008.

[35] H. Willmann, P. H. Maryhofer, P. O. Persson, A. E. Reiter, L. Hultmann and C. Mitterer, *Scr. Mater.,* vol. 54, p. 1847, 2006.

[36] J. Lin, B. Mishra, J. J. Moore and W. D. Sproul, *Surf. Coat. Technol.,* vol. 201, p. 4329, 2006.

[37] A. E. Reiter, C. Mitterer and B. Sartory, *J. Vac. Sci. Technol.,* vol. A 25, p. 711, 2007.

[38] S. G. Harris, E. D. Doyle, A. C. Vlasveld, J. Audy, J. M. Long and D. Quick,

Wear, vol. 254, p. 1, 2003.

[39] Z. F. Zhou, P. L. Tam, P. W. Shum and K. Y. Li, *Thin Solid Films*, vol. 517, p. 5243, 2009.

[40] A. I. Kovalev, D. L. Wainstein, A. Y. Rashkovskiy, G. S. Fox-Rabinovich, K. Yamamoto, S. Veldhuis, M. Aguirre and B. D. Beake, *Vacuum*, vol. 84, p. 184, 2009.

[41] Q. Luo, W. M. Rainforth, L. A. Donohue, I. Wadsworth and W. Münz, *Vacuum 53*, Vols. 1-2, p. 123, 1999.

[42] S. Yang, E. Wiemann and D. G. Teer, *Surf. Coat. Technol.*, Vols. 188-189, p. 662, 2004.

[43] S. Yang, X. Li and D. G. Teer, *Surf. Eng.*, vol. 18, p. 391, 2002.

[44] K. E. Cooke, S. Yang, C. Selcuk, A. Kennedy, D. G. Teer and D. Beale, *Surf. Coat. Technol.*, vol. 188, p. 697, 2004.

[45] C.-H. Hsu, K.-L. Chen, Z.-H. Lin, C.-Y. Su and C.-K. Lin, *Thin Solid Films*, vol. 518, p. 3825, 2010.

[46] Y. Shi, S. Long, S. Yang and F. Pan, *Appl. Surf. Sci.* , vol. 254, p. 7342, 2008.

[47] I. Wadsworth, I. J. Smith, L. A. Donohue and W. -D. Mqnz, *Surf. Coat. Technol.* , Vols. 94-95, p. 315, 1997.

[48] R. Forsén, M. Johansson, M. Odén and N. Ghafoor, *J. Vac. Sci. Technol.*, vol. A 30 (6), p. 0615061, 2012.

[49] R. Forsén, N. Ghafoor and M. Odén, *J. Appl. Phys.*, vol. 114 (24), p. 244303, 2013.

[50] D. B. Lewis, I. Wadsworth, W. -D. Münz, R. Kuzel Jr. and V. Valvoda, *Surf. Coat.*

Technol., vol. 116, p. 284, 1999.

[51] K. Yamamoto, T. Sato, K. Takahara and K. Hanagur, *Surf. & Coat. Techno.*, vol. 174, p. 620, 2003.

[52] R. Forsén, Mutricomponent Alloying for Improved Hard Coatings, Linköping: LiU-Tryck, 2014.

[53] V. Chawla, A. Chawla, B. S. Sidhu, S. Prakash and D. Puri, *Journal of Minerals & Materials Characterization & Engineering*, vol. 9, no. 11, p. 1037, 2010.

[54] K. Fujita, *Surf. & Coat. Technol.*, vol. 196, p. 139, 2005.

[55] S. Hassan, “Master Thesis,” in *Thermal Stability of cubic and nanocrystalline arcevaporated TiCrAlN coatings*, Linköping, Linköping, 2015, pp. 14-15.

[56] S. Hashmi, Comprehensive Materials Proseccing, Newnes: Elsevier, 2014.

[57] L. S. Darken and R. W. Gurry, Physical Chemsitry of Metals, New York: McGraw-Hill, 1953.

[58] H. Hindam and D. P. Whittle, *Oxid. Met.*, vol. 18, p. 245, 1982.

[59] N. Birks and G. H. Meier, Introduction to High Temperature Oxidation of Metals, London: Edwars Arnold Ltd, 1983.

[60] M. F. Ashby and D. R. H. Jones, Engineering Materials 1, Oxford: Butterworth-Heinemann, 1996.

[61] J. Als-Nielsen and D. McMorrow, in *Elemets of Modern X-Ray Physics* , Copenhagen, Wiley, 2000.

[62] L. S. Zevin and G. Kimmel, Quantitative X-Ray Diffractometry, 1st Edition, Springer, 1995.

[63] DESY, “photon-science.desy.de,” Deutsches Elektronen-Synchrotron DESY, 2015. [Online]. [Accessed 1 August 2015].

[64] N. Schell, A. King, F. Beckmann, T. Fischer, M. Müller and A. Schreyer, *Materials Science Forum,* vol. 722, p. 57, 2014.

[65] a. R. W. S. Rointan F. Bunshah, Handbook of Deposition Technologies for Films and Coatings: Science, Technology and Applications, 2. ed. ed., Park Ridge, N.J.: Noyes, 1994.

[66] D. M. Mattox, “HANDBOOK OF PHYSICAL VAPOR DEPOSITION (PVD) PROCESSING,” in *HANDBOOK OF PHYSICAL VAPOR DEPOSITION (PVD) PROCESSING,* Albuquerque, New Mexico, NOYES PUBLICATIONS Westwood, New Jersey, U.S.A., 1998, pp. 31-60.

[67] D. Mattox, “"Metal Finishing",” vol. 100, p. 394, 2002.

[68] A. Anders, *Phys. Rev.* , vol. E55, p. 969, 1997.

[69] A. A, Cathodic arcs - From Fractal Spots to Energetic Condensation, New York: Springer, 2008.

[70] J. Vyskocil and J. Musil, “J. Vac. Sci. & Technol.,” vol. A 10, p. 1740, 1992.

[71] A. Anders, *Vacuum,* vol. 67, p. 673, 2002.

[72] R. L. Boxman and S. Goldsmith, *Surface and Coatings Technology,* vol. 33, p. 153, 1987.

[73] L. Rogström, High temperature behavior of arc evaporated ZrAlN and TiAlN thin films, Linköping: LiU-Tryck, 2012.

[74] I. Petrov, P. B. Barna, L. Hultman and J. E. Greene, *J. Vac. Sci. Technol.,* vol. A 21, p. 117, 2003.

[75] I. Petrov, L. Hultman, U. Helmersson, J. E. Sundgren and J. E. Greene, *Thin Solid Films,* vol. 169, p. 299, 1989.

[76] H. Hasegawa, T. Yamamoto, T. Suzuki and K. Yamamoto, *Sur. and Coat. Technol.* , vol. 200, p. 2864, 2006.

[77] R. W. Cheary and A. A. Coelho, *J. Appl. Cryst. 1998*, vol. 31, p. 851, 1998.

[78] V. K. Pecharsky and P. Y. Zavalij, Fundamental of Powder Diffraction and Structural Characterization of Materials, 2nd Edition, Springer, 2009.

[79] D. L. Bish and E. P. Jeffrey, Modern Powder Diffraction, Reviews in Mineralogy vol.20, vol. 20, Mineralogical Society of America, 1989.

[80] B. D. Cullity, Elements of X-ray diffraction, Addison-Wesley Publishing Company, Inc., 1978.

[81] “Excelsus,” Development & Design by Novitis, 06 11 2015. [Online]. Available: http://www.excels.us/index/pages/id_page-33/lang-en/.

[82] M. Sakata, S. Aoyagi, T. Ogura and E. Nishibori, *AIP Conference Proceedings*, vol. 879, p. 1829, 2007.

[83] F. Gozzo, “The power of synchrotron X-ray powder diffraction,” www.scienceomega.com, Science Omega Review: issue 3.

[84] D. Ostach, L. Rogström and U. Lienert, *Matlab program written by Lina Rogström (IFM, Linköping) based on Ulrich Lienert (DESY, Hamburg), Matlab scripts modified by Daniel M. Ostach (HZG, Hamburg).*

[85] J. Lin, X. Zhang, Y. Ou and R. Wei, *Surf. & Coat. Technol.*, vol. 277, p. 58, 2015.

[86] OSRAM, “OSRAM Licht AG,” 24 August 2015. [Online]. Available: http://www.osram.de/osram_de/produkte/lampen/speziallampen/halogen-niedervoltlampen/halogenlampen-mit-reflektor-

mr16/index.jsp?productId=ZMP_56082.

[87] P. Biplab, J. L. Schroeder, S. Kerdsongpanya, N. V. Nong, N. Schell, D. Ostach, J. Lu, J. Birch and P. Eklund, *Adv. Electron. Mater.,* vol. 1, p. 1400022, 2015.

[88] D. M. Ostach, N. Schell, A. Schreyer, J. Birch, J. Schroeder, L. Rogström, Y. H. Chen and M. P. Johansson-Jõesaar, "Phase Transformation During Annealing in Air and Vacuum Atmosphere in Arc Evaporated (Ti,Cr,Al)N Coatings Studied by In-situ High Energy X-ray Diffraction," in *ICMCTF 2015*, Sand Diego, USA, 2015.

[89] N. Norrby, L. Rogström, M. P. Johansson-Jõesaar, N. Schell and M. Odén, *Acta Materialia,* vol. 73, p. 205, 2014.

[90] T. P. Li, X. H. Yin, M. S. Li and Y. C. Zhou, *Oxid Met*, vol. 68, p. 193, 2007.

[91] F. Vaz, L. Rebouta, M. Andritschky, M. F. Da Silva and J. C. Soares, *J. Eur. Ceram. Soc.,* vol. 17, p. 1971, 1997.

[92] D. McIntyre, J. E. Greene, G. Hakansson, J. Sundgren and W. Münz, *J. Appl. Phys.* , vol. 67, p. 1542, 1990.

[93] L. Chen, J. Paulitsch, Y. Du and P. H. Mayrhofer, *Surf. Coat. Technol.,* vol. 206, p. 2954, 2012.

[94] Y. H. Chen, L. Rogström, D. Ostach, N. Ghafoor, M. P. Johansson-Jõesaar, N. Schell, J. Birch and M. Odén, *Surf. Coat. & Technol.,* submitted.

[95] R. Rachbauer, S. Massl, E. Stergar, D. Holec, D. Kiener, J. Keckes, J. Patscheider, M. Stiefel, H. Leitner and P. H. Mayrhofer, *J. Appl. Phys.,* vol. 110, p. 023515, 2011.

[96] P. H. Mayrhofer, A. Hörling, I. Karlsson, J. Sjölen, T. Larsson, C. Mitterer and I. Hultman, *Appl. Phys. Lett.,* vol. 83, p. 2049, 2003.

[97] P. H. Mayrhofer, F. D. Fischer, H. J. Bohm, C. Mitterer and J. M. Schneider, *Acta Matrialia,* vol. 55, p. 1441, 2007.

[98] M. Odén, L. Rogström, A. Knutsson, M. R. Terner, P. Hedström, J. Almer and J. Ilavsky, *Appl. Phys. Let.,* vol. 94, p. 053114, 2009.

[99] L. Rogström, J. Ullbrand, J. Almer, L. Hultmann, B. Jansson and M. Odén, *Thin Solid Films,* vol. 520, p. 5542, 2012.

[100] H. Willmann, P. H. Mayrhofer, I. Hultman and C. Mitterer, *J. Mater. Res.,* vol. 23, p. 2880, 2008.

[101] M. Odén, J. Almer, G. Hakansson and M. Olsson, *Thins Solid Films,* vol. 377, p. 407, 2000.

[102] K. Grönhagen, J. Agren and M. Odén, *Scripta Materialia,* vol. 95, p. 42, 2015.

[103] A. Flink, J. M. Andersson, B. Alling, R. Daniel, J. Sjölen, L. Karlsson and L. Hultman, *Thin Solid Films,* vol. 517, p. 714, 2008.

[104] S. Khamseh, M. Nose, T. Kawabata, K. Matsuda and S. Ikeno, *Materials Transactions,* vol. 51, no. 2, p. 271, 2010.

[105] P. Karvankova, M. G. J. Veprek-Heijmana, M. F. Zawrahb and S. Vepreka, *Thin Solid Films,* vol. 467, p. 133, 2004.

[106] O. Knotek and A. Barimani, *Thin Solid Films,* vol. 174, p. 51, 1989.

[107] A. Hörling, J. Sjölen, L. Karlsson, M. Odén and L. Hultmann, *J. Vac. Sci. Technol.,* vol. A 20, p. 1815, 2002.

[108] H. A. Jehn, S. Hofmann, V. Ruckborn and W. Munz, *J. Vac. Sci. Technol.* , vol. A 4, p. 2701, 1986.

[109] M. Zhu, M. Li and Y. Zhou, *Surf. & Coat. Technol.,* vol. 201, p. 2878, 2006.

[110] M. W. Brumm and H. J. Grabke, *Corrosion Science* , vol. 33, p. 1677, 1992.

[111] S. Hasani, M. Panjepour and M. Shamanian, *Open Access Scientific Reports,* vol. 1, no. 8, 2012.

[112] A. Khatibi, J. Lu, J. Jensen, P. Eklund and L. Hultman, *Surface and Coatings Technology* , vol. 206, p. 3216, 2012.

[113] M. Avrami, *The Journal of Chemical Physics* , vol. 7, p. 1103, 1939.

[114] M. Avrami, *The Journal of Chemical Physics 8,* vol. 8, p. 212, 1940.

[115] M. Avrami, *The Journal of Chemical Physics,* vol. 9, p. 177, 1941.

[116] W. A. Johnson and R. F. Mehl, *Trans Amer Inst Min Met Eng,* vol. 135, p. 416, 1939.

[117] E. A. Jägle and E. J. Mittemeijer, *Acta Materialia,* vol. 59, p. 5775, 2011.

[118] W. D. Kingery, H. K. Bowen and D. R. Uhlmann, Introduction to ceramics, 2nd Edition, New York: John Wiley, 1976.

[119] A. L. Brown and M. G. Norton, *J. Mater. Sci. Let,* vol. 17, p. 1519, 1998.

[120] E. W. Osborne and M. G. Norton, *J. Mater. Sci.,* vol. 33, p. 3859, 1998.

[121] A. Atkinson, *Solid State Ionics,* vol. 12, p. 309, 1984.

[122] R. Freer, *J. Mater. Sci.,* vol. 15, p. 803, 1980.

[123] Y. K. Yao, Stoichiometry and Thermodynamics of Metallurgical Processes, Cambridge: Cambridge University Press, 1985.

[124] D. Suryanarayana, *J. Amer. Ceram. Soc.,* vol. 73, p. 1108, 1990.

[125] L. Rogström, N. Norrby, J. Schroeder, D. Ostach, Y. H. Chen, M. P. Johansson, N. Schell, M. Odén and J. Birch, "Growth of h-AlN in TiAlN and TiCrAlN coatings studied in-situ during annealing by high energy x-ray diffraction," photon-science.desy.de, Hamburg, 2013.

[126] D. M. Ostach, N. Schell, A. Schreyer, J. Birch, J. Schroeder, L. Rogström, Y.-H. Chen, M. P. Johansson-Jõeasaar and M. Rachid, "In-situ high energy x-ray diffraction studies on the phase evolution during decomposition of arc evaporated (Ti,-Cr,-Al)N coatings," in *DPG 2014*, Dresden, 2014.

[127] D. M. Ostach, N. Schell, A. Schreyer, J. Schroeder, J. Birch, L. Rogström, Y.-H. Chen and M. p. Johansson-Jõeasaar, "High temperature phase transformations & oxidation behavior of arc evaporated (Ti, Cr, Al)N coatings," in *MSE 2014*, Darmstadt, 2014.